1-1-1990

A multi-transition study of the cyclic molecule cyclopropenylidene (C2H2) in the galaxy.

Suzanne C. Madden
University of Massachusetts Amherst

A MULTI-TRANSITION STUDY OF THE CYCLIC MOLECULE CYCLOPROPENYLIDENE (C_3H_2) IN THE GALAXY

A Dissertation Presented

by

SUZANNE C. MADDEN

Submitted to the Graduate School of the
University of Massachusetts in partial fulfillment
of the requirements for the degree of

DOCTOR OF PHILOSOPHY

February 1990

Department of Physics and Astronomy

A MULTI-TRANSITION STUDY OF THE CYCLIC MOLECULE

CYCLOPROPENYLIDENE (C_3H_2) IN THE GALAXY

A Dissertation Presented

by

SUZANNE C. MADDEN

Approved as to style and content by:

William M. Irvine, Committee Chairperson

Lorne W. Avery, Member

John Kwan, Member

F. Peter Schloerb, Member

Ronald L. Snell, Member

Robert A. Guyer, Outside Member

Henry E. Matthews, Consultant

Robert B. Hallock, Department Head

Department of Physics and Astronomy

ACKNOWLEDGEMENTS

I would like to thank some of the many people who were sources of support and encouragement throughout my graduate school tenure. My advisor, Bill Irvine, allowed me the independence I needed, while also providing the direction and discipline necessary for my productivity all these years. I am grateful to him for continuous financial support, especially for an inordinate ammount of observing trips and conferences. I have much to thank you for, Bill. I thank Lorne Avery whose continuing interest and insight in this project helped me to see the end of my dissertation.

I feel there exists a particularly helpful and encouraging attitude toward graduate students among the UMass astronomy faculty. I thank all of you, and especially Ron Snell for valuable discussions about my research.

This dissertation is deeply rooted in massive observing efforts over the past years with most of the credit belonging to the helpful and competent telescope operators at Green Bank, West Virginia, especially Tom Carpenter, Harold Grist, Ralph High, Larry Brothers and Preston Meadows. These observations would not have been possible without the reliable Henry Taylor and Meri Kerr who performed well beyond the call of duty getting me back and forth to the airport.

I am endebted to John MacLeod and Lorne Avery for my "sabattical" opportunity at Herzberg Institute of Astrophysics in Ottawa during my final year. I thank the entire HIA Radio Astronomy

Section for providing me with a most productive and hospitable environment during those crucial months.

I am ever in awe of the miracles performed by Jackie Goionka, Barbara Keyworth, Denise Kuzmescus and Sally Ruie. I dont even want to imagine what my years in graduate schooi would have been like without the competence and forever calm and cheerful demeanor of these very special people.

Life as a graduate student was endurable only through the efforts of special good friends including Young Minh, Beth Norton, Carsten Kömpe, Gina Daddario and Steve Lord. Particular thanks go to Jim Morgan who was always willing to tackie my Mongo problems. He deserves the credit for many of the figures in this dissertation. I thank Shuding Xie for her sagely advice and intimate friendship over the many years. Special thanks go to Bev Smith for her continuous inspiration as my running and lifting "coach". Thank you Bev and Lori Allen for the countless sources of joy and the many necessary and stimulating astrosociology discussions. I thank Sylvie Cabrit for valuable astronomy discussions and a critical review of this work.

I thank my very special friend, Beth Berry, who has been an unfailing source of encouragement and sound advice. For all her help, including typing, proof-reading, and a home, I am eternally grateful.

Many thanks go to my family, especially my parents, who have endured these years anxiously and who have given me astronomical amounts of love and encouragement.

ABSTRACT

A MULTI-TRANSITION STUDY OF THE CYCLIC MOLECULE CYCLOPROPENYLIDENE (C_3H_2) IN THE GALAXY

FEBRUARY 1990

SUZANNE C. MADDEN, B.S., MICHIGAN STATE UNIVERSITY

M.S., UNIVERSITY OF MASSACHUSETTS

Ph.D., UNIVERSITY OF MASSACHUSETTS

Directed by: Professor William M. Irvine

We report results of multi-transition observations and modeling of the hydrocarbon ring molecule cyclopropenylidene (C_3H_2). From a survey of the $1_{10}-1_{01}$ (18 GHz) and $2_{12}-1_{01}$ (85 GHz) transitions in the Galaxy, we have found C_3H_2 present in a variety of sources including cold, dark clouds, giant molecular clouds, the envelope of a carbon star, and diffuse clouds. Up to 10 transitions of C_3H_2 ranging in wavelength from 1.3 cm to 1.3 mm were observed in the dark clouds L1498, L134N, B335 and toward several positions in TMC-1. The Large Velocity Gradient (LVG) approximation was used to model the observations. Optical depth values of C_3H_2, estimated from $C^{13}C_2H_2$ observations, are necessary to constrain the results since the range in excitation energies of the observed C_3H_2 transitions does not contrast sufficiently. The molecular hydrogen density in TMC-1 is estimated to be 3.7×10^4 cm^{-3}, while the fractional abundance of C_3H_2 relative to H_2 is 5.7×10^{-9}. Previous estimates assuming LTE conditions overestimate the abundance of C_3H_2. The abundance in the

ridge component in Orion is estimated to be approximately 8×10^{-10} cm^{-2}.

Gas phase chemical models can reproduce the high C_3H_2 abundance found in dark clouds under assumptions such as steady state conditions with [C]/[O]/ > 1.0, conditions of earlier evolutionary time, or 'optimistic' rate coefficients. However, large deuteration ratios (0.05 to 0.15) create difficulties for gas phase models.

TABLE OF CONTENTS

LIST OF TABLES

LIST OF FIGURES

CHAPTER 1

INTRODUCTION

In spite of the fact that molecular clouds are a dominant mass constituent of the interstellar medium, we are far from completely specifying the physical and chemical conditions in any real cloud. Major uncertainties exist in deciphering the signatures of cloud properties present in spectral lines, since the observed intensities and line widths can be extremely complex functions of many variables. Nevertheless, efforts to determine properties such as molecular hydrogen density and molecular abundance often proceed from only an observed pair of lines in various molecules, sometimes resulting in contradictions. Reliable determinations of physical parameters in a molecular cloud often require observations of several transitions of a species. Multi-transitional modeling has been pursued, for example, by Snell *et al.* (1984) using 4 transitions of CS, Mundy *et al.* (1986) using 3 transitions of $C^{34}S$, Mundy *et al.* (1987) using 6 transitions of H_2CO and Swade (1989) who analyzed the dark cloud L134N from multi-species, multi-level observations (cf. Irvine, Goldsmith and Hjalmarson 1987; Goldsmith 1987).

The versatility of molecules as probes of the physics and chemistry of the environment in which they are formed is critical for studying the chemical evolution of molecular clouds, which in turn is important in understanding protostellar evolution. The observed distribution of a molecular species is a product of chemical reaction

networks which are dependent on the physical conditions, both present and initially, in molecular clouds. Elaborate models composed of thousands of chemical reactions have been constructed in an effort to match observed chemical abundances, and molecular line observations can provide a potential discriminant between alternate reaction schemes. Difficulties in simulating the temperatures and densities of interstellar environments in a terrestrial laboratory often hamper the measurement of accurate reaction rates neccessary for the chemical models.

Laboratory spectroscopy plays a crucial role in the discovery of new interstellar molecules. For example, a combination of fortuitous observations at 1.3 cm (Matthews and Irvine 1985) and clever laboratory sleuthing (Thaddeus, Vrtilek and Gottlieb 1985) succeeded in assigning a new molecule, C_3H_2, as the carrier of several unidentified interstellar lines, including unidentified 3mm lines reported in 1981 (Thaddeus, Guelin and Linke 1981). C_3H_2 became the first cyclic hydrocarbon molecule detected in space, adding to the growing list of more than 70 known interstellar molecules.

Years of futile deliberate searches for simple ring molecules preceded this accidental discovery, since it had seemed that at least simple cyclic hydrocarbons should be present in the interstellar medium along with such heavy organic molecules as the cyanopolyynes ($HC_{2n}CN$, n = 0 to 5) which had already been detected.

C_3H_2 possesses a significant polarity, giving it a large dipole moment (μ = 3.3 Debye). Generally, a more polar molecule requires higher local molecular hydrogen densities to excite it to an

observable intensity in the interstellar medium. Hence HCN and CS (μ = 3.0 and 2.0 Debye, respectively) are regarded as good probes of high density material, whereas CO, which has a low dipole moment (μ = 0.1 Debye), can be observed toward regions of lower densities.

Soon after its interstellar identification it was thought that C_3H_2 might have potential as a useful probe for physical conditions in molecular clouds since 1) many observable transitions of C_3H_2 exist in the cm to mm wavelength range; 2) a potentially diagnostic property of the 2_{20}-2_{11} transition is that it is one of the rare molecular transitions detected in absorption against dark clouds - refrigerated below the 2.7 K microwave background radiation as are certain lines of H_2CO and CH_3OH; 3) having a large dipole moment, it has the potential to be a density sensitive molecule; and 4) C_3H_2 is a ubiquitous molecule in the Galaxy. This study explores diagnostic possibilities for C_3H_2, as well as its abundance distribution in the Galactic interstellar medium. A goal was to obtain data for a range of transitions in several dark cloud sources and construct a model to derive parameters such as $n(H_2)$ and $X/(dv/dr)$.

This dissertation is arranged in a somewhat historic way. Chapter 2 is an overview of the chemical and physical properties of C_3H_2. Chapter 3 is a publication by Madden *et al.* (1989) which demonstrates the ubiquity of C_3H_2 in the Galaxy. An extensive survey carried out at 21 and 18 GHz along with limited surveys at 7 and 3 mm characterize C_3H_2 as a relatively abundant and widespread molecule. It is detected in a variety of environments, including giant molecular clouds, diffuse clouds, cold dark clouds, the spiral arms

in the direction of distant continuum sources, and the envelope of a carbon star. Chapter 4 describes observations of isotopic C_3H_2 species. Section 4.1 is a published paper by Madden, Irvine and Matthews (1986) presenting estimates of column densities in several sources based on ^{13}C-substituted C_3H_2 observations. The fractional abundance relative to H_2 in TMC-1 is estimated to be $\sim 10^{-8}$, making it one of the more abundant organic molecules in the interstellar medium. The deuterated version of C_3H_2 was detected in dark clouds and deuteration ratios (0.05 to 0.15) are among the highest observed in the Galaxy (reported in section 4.2). In Chapters 3 and section 4.1 the basic format of the published papers is maintained so that these sections are self-contained and can be read independently. Chapter 5 gives a review of basic radiative transfer formalism and describes procedures used in this study for multi-transition modeling utilizing a uniform density Sobolev approximation and a 2-component model. The results of such modeling applied to the dark clouds TMC-1, L1498, L134N, and B335, for which 4 to 10 C_3H_2 transitions have been detected, are presented in Chapter 6. Chapter 7 draws conclusions and illuminates prospects to be addressed in light of this C_3H_2 study.

CHAPTER 2

PHYSICS AND CHEMISTRY OF THE C_3H_2 MOLECULE

2.1 Structure of the C_3H_2 Molecule

Ab initio calculations and spectroscopic studies have addressed the structure and stability of hydrocarbons with the formula C_3H_2 for the past 20 years, beginning with the nearly linear form, propargylene (H-C=C-C-H) (Jones *et al.* 1968; Bernheim *et al.* 1965). The cyclic version, cyclopropenylidene, was first detected in an argon matrix via the vibrational spectrum at IR wavelengths (Reisenauer *et al.* 1984) and finally at mm wavelengths (Thaddeus, Vrtilek and Gottlieb 1985; Vrtilek, Gottlieb and Thaddeus 1987). Of 5 stable isomers which exist on the C_3H_2 potential energy surface, cyclopropenylidene has been determined to have the lowest energy ground state (DeFrees and McLean 1986).

Cyclopropenylidene is a 3-member carbon ring structure with hydrogen atoms attached to two of the carbon atoms (Figure 2.1). Two electrons associated with the bivalent carbon atom cause C_3H_2 to be an exceptionally polar hydrocarbon with a permanent dipole moment determined both experimentally and theoretically to be 3.4 Debye (Lee, Bunge and Schaefer 1985; Kanata, Yammamoto and Saito 1987; Brown, Godfrey and Bettens 1987). The two identical hydrogen atoms can be interchanged and the molecule converted into an identical configuration through a rotation of $2\pi/n$ degrees (where n=2 in the

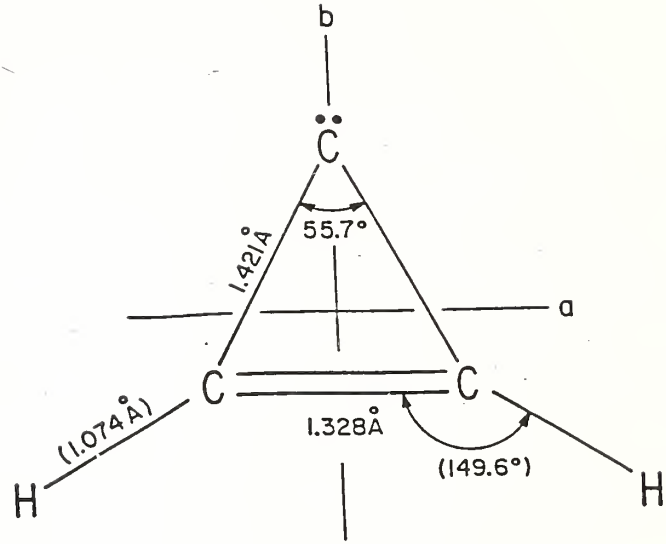
b
C
55.7°
1.421Å
a
C
C
(1.074Å)
1.328Å
(149.6°)
H
H

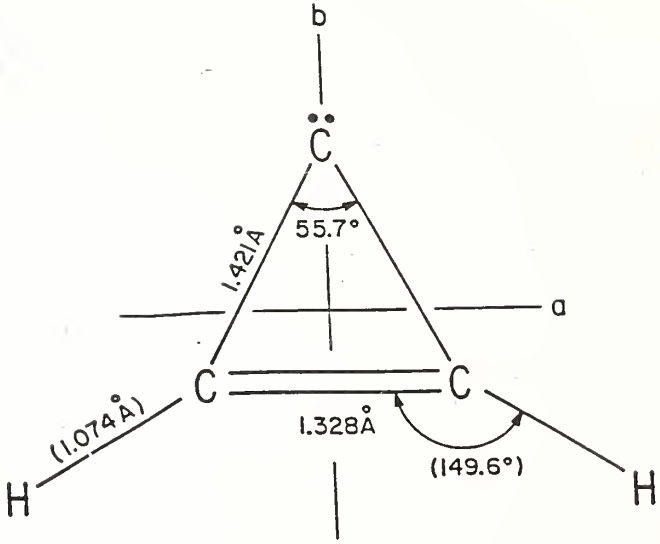
b
C
55.7°
1.421Å
a
C
C
(1.074Å)
1.328Å
(149.6°)
H
H

case of C_3H_2) about the axis of symmetry (labeled the b axis in Figure 2.1). In the notation of group theory, this symmetry operation identifies C_3H_2 with C_{2v} symmetry, denoting the presence of 2 symmetry planes and a 2-fold rotation axis through the bivalent carbon atom.

Ab initio calculations determined the electronic configuration of C_3H_2 (Lee, Bunge and Schaefer 1985) and the result was confirmed in an argon matrix at 10 K (Reisenauer *et al.* 1984). The ground electronic state of C_3H_2 has no electronic angular momentum making it a $^1\Sigma$ state. Thus, the sum of the orbital angular momenta of the electrons is zero as is the sum of the electron spins. (The superscript 1 indicates that the electronic spin = 0 corresponding to a singlet state). This implies that application of an electric or magnetic field to the C_3H_2 molecule produces no splitting.

On account of the 2 symmetrically placed off-axis hydrogen nucleii, each a single proton of spin = $\pm$ 1/2, the rotational levels of C_3H_2 are segregated into 2 distinct symmetry states: ortho and para. The para species has the nuclear spins of the hydrogen atoms arranged antiparallel with a total nuclear spin (I) of 0, while the ortho form has parallel nuclear spins producing I = 1. Interconversion from one form to the other is strictly forbidden (quantum mechanically) through radiative or collisional processes. Under conditions governed by local thermodynamic equilibrium (LTE), the ortho-para ratio (O:P) in the high temperature limit is expected to be equal to 3:1, the ratio of the respective statistical weights.

Other molecules existing in ortho and para forms are, for example, H_2, H_2CO, H_2CS, and H_2O.

Table 2.1

C_3H_2 Rotational Constants

A: 35092.596 MHz
B: 32212.931 MHz
C: 16749.315 MHz

Although C_3H_2 is an asymmetric rotor since all of its principal moments of inertia are different (Table 2.1, recalling that the moment of inertia $I_a \alpha 1/A$ where A is the molecular constant), it can be described in the notation similar to that of a symmetric top since two of its principal moments of inertia are similar. In the custom of assigning the moments of inertia, I_A, I_B, I_C, in order of increasing value (or decreasing value of molecular constants A, B and C), we see that $I_A \approx I_B < I_C$. These properties describe C_3H_2 as a nearly oblate symmetric top: its ellipsoid of inertia has a pancake shape where the 2 smaller moments of inertia are nearly equal.

The energy level diagram for C_3H_2 can most easily be discussed by first considering the more simple symmetric rotor case and then examining the behavior of the energy levels as the molecule deviates

from the simple oblate case. A parameter used to describe a molecule's "oblateness" or "prolateness" is Ray's asymmetry parameter: $\kappa = (2B-A-C)/(A-C)$, where A, B and C are the molecular rotation constants (Table 2.1). For C_3H_2 $\kappa = +0.69$. If C_3H_2 were truly symmetric, κ would be 1 (and -1 for prolate symmetric molecules where B = C). The quantum numbers used to designate a particular energy configuration for the symmetric rotor are J, the total angular momentum of the molecule and K, the projection of J on the axis of symmetry. For the asymmetric rotor case, however, K is not a constant along any single direction and therefore is not a good quantum number to describe the state. A traditional system which is used for labeling the energy states in asymmetric cases attempts to give simple physical meaning: J continues to be the total angular momentum and K_{-1} and K_{+1} correspond to the limiting prolate and oblate cases, respectively. Therefore the convenient notation to describe a particular state is $J_{K_{-1}K_{+1}}$. Ortho and para states are such that $K_{-1} + K_{+1}$ is, respectively, an odd or an even value.

The energy level diagram shown in Figure 2.2. is segregated into ortho and para states and arranged into individual K_{+1} ladders. The vertical axes indicate the energy (E) in temperature units of each level above the ortho or para ground state (E/k, where k is the Boltzmann constant). Notice that the ground ortho level ($J_{K_{-1}K_{+1}} = 1_{01}$) is 2.4 K above the ground para level ($J_{K_{-1}K_{+1}} = 0_{00}$).

Figure 2.2 The energy level diagram of C_3H_2 with rotational energy levels separated into ortho and para species. The vertical axes indicate energy above the ground para level in temperature units (K). The ortho ground level is 2.4 K above the ground para level.

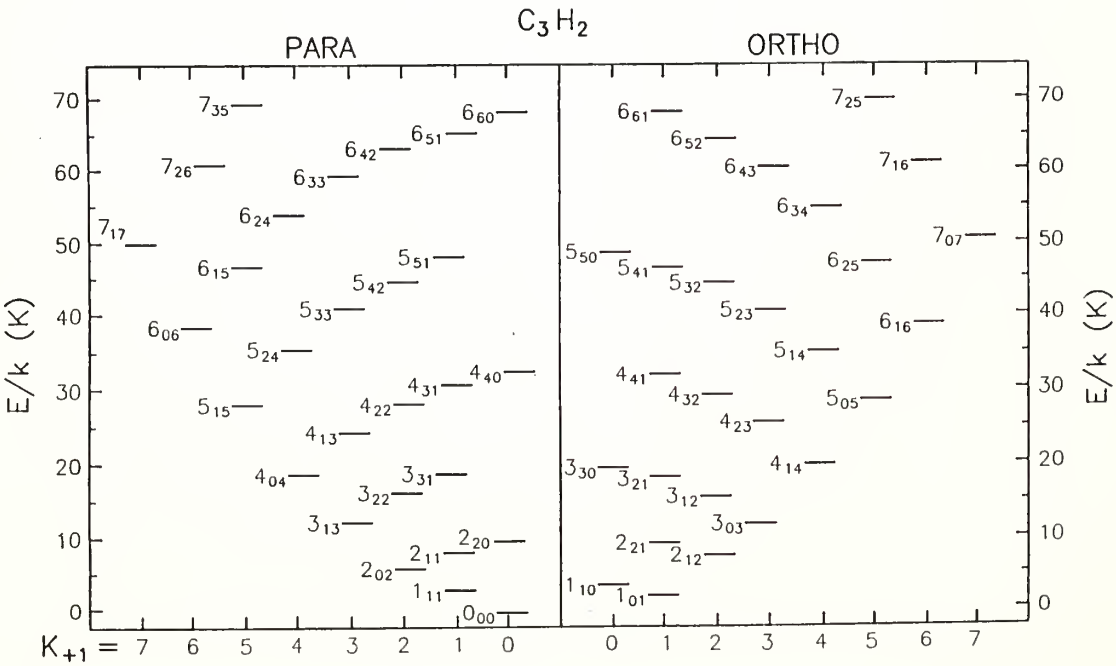
C3 H2
PARA
ORTHO
E/k (K)
K+1 =
7 6 5 4 3 2 1 0
0 1 2 3 4 5 6 7
0 10 20 30 40 50 60 70
7 35
7 26
7 17
6 60
6 51
6 42
6 33
6 24
6 15
6 06
5 51
5 42
5 33
5 24
5 15
4 40
4 31
4 22
4 13
4 04
3 31
3 22
3 13
2 20
2 11
2 02
1 11
0 00
6 61
6 52
6 43
6 34
6 25
6 16
5 50
5 41
5 32
5 23
5 14
5 05
4 41
4 32
4 23
4 14
3 30
3 21
3 12
3 03
2 21
2 12
1 10
1 01
7 25
7 16
7 07

2.2 The Chemistry of C_3H_2

The synthesis of C_3H_2 is proposed to follow from a sequence of gas-phase chemical reactions involving carbon-bearing molecules, beginning with the radiative association reaction (Herbst 1983):

$$C^+ + H_2 \rightarrow CH_2^+ + h\nu. \qquad (2.1)$$

This is followed by a series of reactions with molecular hydrogen and ion-electron reactions leading to the formation of one-carbon molecules. Two-carbon species are then synthesized via reactions of C^+ or C with the one-carbon molecules. Eventually, the relatively fast reaction of acetylene (C_2H_2) with C^+ occurs (van Dishoeck 1988; Adams and Smith 1987; Herbst, Adams and Smith 1984):

$$C_2H_2 + C^+ \rightarrow C_3H^+ + H. \qquad (2.2)$$

Adams and Smith (1987) propose that the subsequent radiative association reaction,

$$C_3H^+ + H_2 \rightarrow C_3H_3^+ + h\nu, \qquad (2.3)$$

is the primary pathway for the reservoir of both the cyclic (c) isomer of $C_3H_3^+$ (cyclopropenium ion) and the linear (l) $C_3H_3^+$ species (propargyl ion) with equal probability. $C_3H_3^+$ finally undergoes dissociative recombination to form C_3H_2 or C_3H:

$$c\text{-}C_3H_3^+,\ l\text{-}C_3H_3^+ \xrightarrow{e^-} C_3H,\ l\text{-}C_3H_2,\ c\text{-}C_3H_2. \qquad (2.4)$$

It is not clear whether the precursor for $c\text{-}C_3H_2$ should be the linear or cyclic ion or what the branching ratios are for all of the possible reactions. Other gas-phase routes for the production of $c\text{-}C_3H_2$ have been studied and are thought to be less significant (Adams and Smith 1987; Bohme 1986). Although the linear and cyclic form of $C_3H_3^+$ are produced with equal probability from C_3H^+, the linear form is more reactive in ion-molecule reactions and will be destroyed more rapidly, making the cyclic species more abundant.

Destruction mechanisms for C_3H_2 include the following reactions (Herbst 1983; Herbst, Adams and Smith 1984):

$$H_3^+ + C_3H_2 \rightarrow C_3H_3^+ + H_2, \qquad (2.5)$$

$$HCO^+ + C_3H_2 \rightarrow C_3H_3^+ + CO, \qquad (2.6)$$

$$H_3O^+ + C_3H_2 \rightarrow C_3H_3^+ + H_2O, \qquad (2.7)$$

$$C^+ + C_3H_2 \rightarrow C_4H^+ + H. \qquad (2.8)$$

Oxygen can also participate in the destruction of C_3H_2 via:

$$C_3H_2 + O \rightarrow C_2H_2 + CO \qquad (2.9)$$

if the activation energy is low (Sternberg, Dalgarno and Lepp 1987). It should also be possible to remove C_3H_2 via the neutral-neutral

reaction (Herbst 1983),

$$C_3H_2 + N \rightarrow HC_3N + H \ , \qquad (2.10)$$

but at cloud temperatures of 10 K, this pathway is thought to be insignificant since a large activation energy barrier must be overcome.

Detailed chemical models have been developed which are time dependent in the sense that *physical* conditions of the cloud are fixed and homogeneous, and the *chemical* conditions are allowed to evolve from initial values toward steady state conditions which are reached after about 10^7 years (Prasad and Huntress 1980; Graedel, Langer and Frerking 1982; Millar and Freeman 1984; Millar and Nejad 1985 and Herbst and Leung 1986). In general, the steady state gas phase model values reproduce the observed abundances of the simple molecules but fail in the case of the more complex molecules such as C_3H_2 and the cyanopolyynes, except in the model of Millar and Nejad (1985) who have employed more 'optimistic' values for the reaction rate coefficients, and ignored other processes which can depress complex molecule growth (Millar, Leung and Herbst 1987). In this case, model predictions for the steady state abundance of C_3H_2 give an abundance relative to H_2 of ~ 8×10^{-8} for a molecular cloud with $n(H_2) = 3\times10^4$ cm^{-3}, which is about an order of magnitude *greater* than that observed for TMC-1 (see Cahpter 6) while all other model steady state abundance values underpredict C_3H_2 (and other hydrocarbon molecules) by 3 to 5 orders of magnitude.

One of the chronic deficiencies in these models is that by the time steady state is reached too little atomic carbon remains to match the large abundances of CI that are observed inside dark clouds (Keene *et al.* 1985). Subsequent steady state models have therefore increased the [C]/[O] ratio to be greater than 1.0, which is larger than the solar value of 0.5 (Langer, Frerking, and Wilson 1986; Herbst and Leung 1986; Langer and Graedel 1989). The abundance of C_3H_2 is coupled to that of atomic carbon since ionized carbon initiates the track of chemical reactions leading to the formation of complex hydrocarbons (equation 2.1). Steady state abundance predictions for C_3H_2 are improved when [C]/[O] > 1.0, but this situation results in low abundance values for oxygen-bearing molecules since the oxygen is used up in CO formation. High [C]/[O] values are proposed to occur by a preferential depletion of H_2O ice versus carbon-containing molecules onto grains (Blake *et al.* 1987; Swade 1989a). In addition, after the sticking of C and O onto grains, reactions with H and H_2 result in CH_4 and H_2O. Evaporation is more easily accomplished by CH_4 rather than H_2O, thus resulting in a larger reservoir of carbon-bearing species in the gas phase. Hence it may be possible for large [C]/[O] values to exist in the gas phase (Blake *et al.* 1987).

Time-dependent results for the dense cloud chemistry show that the abundances of the complex hydrocarbon species reach peak values at an earlier time ($\sim 3\times10^5$ yr), well before steady state is reached, when the [C]/[O] ratio is less than 1. These larger abundances of C_3H_2 are more satisfactory in matching observations in

dense clouds, yet they imply earlier cloud ages than are believed to exist.

Finally, time dependent calculations coupling evolution of cloud physical parameters to chemical evolution have been developed (Gerola and Glassgold 1978; Tarafdar *et al.* 1985). In the model of Tarafdar *et al.* 1985, a molecular cloud evolves from a diffuse stage cloud to one with a dense core and diffuse envelope structure. Varying the collapse rate can control the amount of atomic carbon production and can produce larger values of complex hydrocarbons than steady-state calculations.

The suggestion that large molecules, such as polycyclic aromatic hydrocarbons (PAHs), are a substantial component of the interstellar medium (Omont 1986; Léger and Puget 1984) results in possible modification of the interstellar chemistry. Lepp and Dalgarno (1988) evoke PAHs (or large molecules) to facilitate the synthesis of C_3H_2. In molecular clouds, the free electrons can attach to the PAHs thus creating a reservoir of $PAHs^-$ (Omont 1986). When the abundance of PAHs relative to H_2 is about 10^{-8}, the negatively charged PAHs can alter the chemistry, especially in the case of carbon-bearing species, directly affecting C_3H_2 abundances through mutual - neutralization reactions:

$$C_3H_2^+ + PAH^- \rightarrow C_3H_2 + PAH \qquad (2.11)$$

$$C_3H_3^+ + PAH^- \rightarrow C_3H_2 + H + PAH. \qquad (2.12)$$

Model calculations show that steady state abundances of C_3H_2 in the presence of large molecules can be enhanced over the previous steady state calculations to agree with observations in dark clouds (Lepp and Dalgarno 1988).

Numerous difficulties exist in comparing model predictions of molecular abundances with observational evidence. Lack of experimental data on many critical chemical reaction rates hampers accurate model predictions. Physical variables of molecular clouds such as density, age and initial conditions are coupled with chemical evolution. Ion-molecule synthesis is capable of reproducing the relatively large abundances of C_3H_2 observed in the interstellar medium under steady state conditions but only by assuming a large abundance of PAHs which can alter the chemistry or by assuming the available [C]/[O] ratio is greater than unity (and omitting PAH chemistry). An alternative to assuming steady state conditions is to assume an early cloud age ($\sim 3 \times 10^5$ yr), when C_3H_2 abundances are predicted to peak. However, the predicted peak abundance values exceed observed abundances, and the calculated abundances pass through observed values very rapidly before the low abundances at steady state are reached.

CHAPTER 3

A SURVEY OF CYCLOPROPENYLIDENE IN GALACTIC SOURCES

3.1 Introduction

Searches for cyclic species have been carried out in molecular clouds almost since the first detection of interstellar polyatomic molecules, and have been pursued more vigorously following the discovery of increasingly complex carbon chain molecules. Interest in ring molecules follows from the suggestion that their presence might be an indication of surface formation on interstellar grains (Fertel and Turner 1975), from their presence in carbonaceous chondrites (*e.g.*, Hayatsu and Anders 1981), and from their critical importance for terrestrial biochemistry. The inferred presence of polycyclic aromatic hydrocarbons (PAHs) in the interstellar medium (Allamandola, Tielens, and Barker 1987) also suggests the possibility of less complex ring molecules. Despite the number of searches that have been undertaken for cyclic species (cf. Irvine *et al.* 1981; Kutner *et al.* 1980; Giguere *et al.* 1973; de Zafra *et al.* 1971), success has been very limited: at present the only cyclic species identified in astronomical sources have been SiCC, which has been found only in the envelope of evolved carbon stars (*e.g.* Thaddeus, Cummins and Linke 1984), C_3H_2, and C_3H.

Thaddeus, Vrtilek, and Gottlieb (1985) and Vrtilek, Gottlieb, and Thaddeus (1987) have drawn upon their own laboratory work and astronomical detections by Matthews and Irvine (1985) and Thaddeus, Guélin, and Linke (1981) to identify the first interstellar hydrocarbon ring molecule, cyclopropenylidene (C_3H_2). Ab initio calculations have shown that cyclopropenylidene has a closed shell singlet ground state (Lee, Bunge, and Schaefer 1985), a result confirmed by experiments in an argon matrix at 10 K (Reisenauer *et al.* 1984). The molecule is planar with C_{2v} symmetry and is an asymmetric oblate top with an asymmetry parameter of +0.69. (Thaddeus, Vrtilek and Gottlieb 1985). It has the lowest energy of five stable isomers on the C_3H_2 potential energy surface (DeFrees and McLean 1986). Spin statistics for the two equivalent protons divide the rotational levels into ortho and para symmetry species, as occurs for water. Since both radiative and collisional transitions between these species are forbidden, ortho and para C_3H_2 should be effectively distinct molecules with statistical weights in the ratio of 3:1. Recent calculations by Cox, Walmsley and Güsten (1989) suggest the possibility of a ratio other than 3:1. Because of the presence of two unpaired electrons on the bivalent carbon nucleus, cyclopropenylidene has a large dipole moment (μ = 3.43 Debye; Lee, Bunge, and Schaefer 1985; Kanata, Yamamoto, and Saito 1987).

Recently, the related cyclic molecule, C_3H, has been detected in the laboratory and in space; it is less abundant than and less widely distributed than C_3H_2 (Yamamoto *et al.* 1987).

Earlier observations of C_3H_2 revealed anomalous excitation of the 2_{20}-2_{11} transition at 21 GHz which, as in the case of formaldehyde, is seen in absorption against the cosmic 2.7 K background (Matthews *et al.* 1986). Observations of carbon-13 and deuterated isotopes of C_3H_2 have also been reported (Madden, Irvine, and Matthews 1986; Gerin *et al.* 1987 and Bell *et al.* 1988). Cox, Güsten, and Henkel (1987) have reported the detection of the 1_{10}-1_{01} transition in the planetary nebula NGC7027, and C_3H_2 has been detected in the regions of IRAS cirrus emission (Turner, Rickard and Xu 1989). In the present paper we complement the initial astronomical reports with the results of a survey of mostly galactic sources for the 1_{10}-1_{01} and 2_{20}- 2_{11} transitions (18 and 21 GHz, respectively). In addition, more limited data has been obtained on the 85 GHz 2_{12}-1_{01} transition of ortho C_3H_2 and the 46.8 GHz 2_{20}-2_{11} transition of para C_3H_2. The results indicate that C_3H_2 may provide a very useful probe of physical conditions in molecular clouds, since strong lines are present at a number of widely spaced frequencies (Avery 1987; Avery and Green 1989). We have detected C_3H_2 in almost all the sources observed, with negative results only in the cases of oxygen-rich stellar envelopes and external galaxies (*cf.*, however, Seaquist and Bell 1986; Bell and Seaquist 1988).

This paper is the first in a series of C_3H_2 presentations and serves as an overall preview of many sources observed in our Galactic survey. More complete and in-depth multi-transition analyses are in preparation for specific sources for which much more data has been

obtained, such as the dark clouds TMC-1, L1498, B335, and L134N (see Chapter 6).

3.2 Observations

The observations were carried out during numerous observing sessions between November 1984 and May 1987. Dates and telescope parameters for the observations are given in Table 3.1. Observations of the $1_{10}-1_{01}$ transition at 18 GHz were made using the 42.7 m telescope of the NRAO in Green Bank, West Virginia. All data have been corrected for antenna gain as a function of hour angle and for atmospheric attenuation. All the NRAO observations were carried out using linear polarization and a K-band maser preamplifier, which under good conditions gave system temperatures as low as 40 K. Calibration was accomplished by means of a noise tube. The spectra were obtained with the NRAO Model IV autocorrelation spectrometer, usually split into two or four separate groups of delay channels. This allowed us to observe many of the C_3H_2 spectra with more than one spectral resolution. In many cases, we also observed the HC_3N (J=2-1) transition at 18.2 GHz simultaneously.

Three different observing techniques were used to obtain the K-band (18 and 21 GHz) spectra presented in this paper: (i) frequency switching, in which both signal and reference frequencies remained within the observed bandwidth, for bandwidths up to 20 MHz; (ii) double-beam switching, using the nutating sub-reflector switched

Table 3.1

Observing Log

Transition	Frequency[a] (MHz)	Telescope	η_B	HPBW (arcmin)	Dates
$1_{10}-1_{01}$ ortho	18343.145	NRAO	0.26[b]	1.65	11/84, 3/85, 7/85, 11/85, 12/85, 1/87, 4/87
$2_{20}-2_{11}$ para	21587.400	NRAO	0.26[b]	1.28	11/85, 12/85, 1/87
		NEROC	0.27	1.50	5/86
$2_{11}-2_{02}$ para	46755.62	FCRAO	0.58	1.83	7/85
$2_{12}-1_{01}$ ortho	85338.90	FCRAO	0.56	1.00	12/82, 12/83, 6/85, 5/87

Notes to Table 3.1:

[a] Frequencies are from Vrtilek, Gottlieb and Thaddeus (1987).

[b] The gain is a function of both hour angle and declination at NRAO. Values given are at transit and are derived from observations of the standard calibration sources 3C123 and NGC7027. Beam efficiency is scaled from η_A.

at 1 Hz over a distance of either 8' or 10' at a position angle 112 ° (N through E). Alternate integration periods placed the source in either the signal or reference beam, and the focus was modulated by ± 1/8 wavelength once per minute. The combined effect of this technique is to remove baseline irregularities due to differing power levels between the signal and reference cycles and also to largely eliminate ripple due to reflections within the telescope feed structure (cf. Bell, Feldman and Matthews 1981); (iii) total power, or position switching, in which the signal spectrum is compared to a reference taken some distance (up to 30') from the source. This technique enabled us to identify some cases in which there was clear contamination of data taken by double-beam switching due to line signals in the reference position.

The second K-band transition of C_3H_2 (2_{20}-2_{11} at 21.587 GHz) was observed where strong lines had been seen in the 1_{10}-1_{01} transition. These observations were carried out primarily with the 42.7 m telescope of the NRAO. Matthews *et al.* (1986) presented our preliminary findings for the NRAO observations, and for these and our present observations, the techniques and equipment are the same as described above for the 18.3 GHz observations. Other 21 GHz observations were performed using the 37 m NEROC Haystack antenna, which also made use of a K-band maser preamplifier receiver, an autocorrelation spectrometer, and a noise tube for calibration. For narrow band (less than 10 MHz) observations, frequency switching was

employed. For larger bandwidths, we used the standard position-switching technique.

The higher frequency observations were made with the 14 m telescope of the Five College Radio Astronomy Observatory (FCRAO): the $2_{11}-2_{02}$ transition at 46.8 GHz and the $2_{12}-1_{01}$ transition at 85.3 GHz. Both frequency switching and position switching were employed. FCRAO has a 7 mm double sideband mixer mounted together with a 3 mm mixer which has a single sideband filter where the image is terminated in a cold load. The antenna temperatures have been corrected for atmospheric opacity and losses at the ambient temperature by the standard chopper wheel method (Penzias and Burrus 1973). Spectra were taken with various filter bank configurations with resolutions ranging from 12.5 to 250 kHz resolution.

3.3 Results

We list our results in tabular form in Table 3.2 for the K-band observations and Table 3.3 for the millimeter-wave lines. The Tables contain the results of either numerical gaussian component fits to the data, or eye estimates of the intensity, velocity and width where the line is distinctly non-gaussian. There is a strong velocity component correspondence between these data and those published on other molecules. Especially for the cases where observations were made toward HII regions with intervening diffuse spiral arm material,

Table 3.2

C_3H_2 $1_{10}-1_{01}$ and $2_{20}-2_{11}$ Observations

Source	RA(1950)	DEC(1950)	Frequency (GHz)	T_A^a (K)	Vlsr $km\ s^{-1}$	dV $km\ s^{-1}$	resolution $km\ s^{-1}$	Coments
(a) Galactic Continuum and Star Formation Regions								
W3	$02^h21^m56^s.6$	61°52'59"	18.3	0.08(2)	-39 (1)	8.5(1)	0.77	T_C=4.0 K
				-0.09(1)	-21.7(3)	1.3(2)		
			21.6^b	<0.09	-	-	0.55	
W3(OH)	02 23 16.8	61 38 57	18.3	<0.11	-	-	0.38	
AFGL490	03 23 38.8	58 36 39	18.3	0.083(4)	-12.7(1)	2.3(1)	0.77	
NGC1333	03 26 00.8	31 02 38	18.3	0.096(5)	7.5(6)	1.3(5)	0.081	
Orion KL	05 32 47.0	-05 24 23	18.3	0.11(8)	8.9(1)	4.4(4)	0.77	
			21.6^b	<0.06	-	-	0.55	
Orion 3N1E	05 32 51.0	-05 21 23	18.3	0.18(3)	9.0(5)	2.5	0.77	radical position
			21.6	<0.04	-	-	0.55	
NGC1999	05 33 53.0	-06 47 56	18.3	0.096(9)	9.0(2)	3.0(4)	0.77	
NGC2071	05 44 30.6	00 21 42	18.3	0.150(3)	9.59(2)	1.28(4)	0.38	
Mon R2	06 05 20.0	-06 22 23	18.3	0.12(1)	9.8(1)	2.0(4)	0.38	
S255	06 09 58.3	18 00 11	18.3	0.07(7)	6.9(2)	3.2(4)	0.77	
AFGL961	06 31 57.9	04 15 30	18.3	0.066(8)	12.3(1)	2.0(3)	0.77	
NGC2264	06 38 21.0	09 36 24	18.3	0.22(1)	6.0(6)	2.1(1)	0.77	
	06 38 24.9	09 32 30	18.3	0.09(6)	7.3(1)	3.5(3)	0.77	
NGC6334A	17 16 57.8	-35 51 45	18.3	0.26(2)	-3.5(2)	4.4(5)	0.77	
NGC6334B	17 17 00.5	-35 49 49	18.3	0.19(1)	-2.7(2)	5.4(4)	0.77	
NCG6334C	17 17 11.3	-35 48 25	18.3	0.12(2)	-0.9(6)	7 (1)	0.77	
NGC6334D	17 17 23.0	-35 46 20	18.3	0.22(1)	-3.5(1)	5.9(3)	0.77	
				-0.11(5)	7.7(1)	3.2(1)		
Sgr A	17 42 31.5	-28 59 33	18.3	-0.05(2)	-133(6)	20 (2)	3.1	
				-0.05(1)	-73 (5)	5 (2)		
				-0.19(2)	-49 (4)	5 (1)		
				-0.10(2)	-28 (6)	9 (2)		
				-0.26(3)	0 (5)	11 (1)		
				-0.18(2)	37 (5)	16 (2)		
Sgr B2	17 44 11.3	-28 22 30	18.3	-0.10(1)	-100(5)	16 (5)	3.1	T_C = 2.0 K
				-0.07(2)	-74 (3)	5 (2)		
				-0.05(2)	-56 (2)	5 (1)		
				-0.10(3)	-41 (4)	11 (3)		

(continued on next page)

Table 3.2

(continued)

Source	RA(1950)	DEC(1950)	Frequency (GHz)	T_A^a (K)	Vlsr km s^{-1}	dV km s^{-1}	resolution km s^{-1}	Coments
				-0.07(2)	-22 (5)	16 (3)		
				-0.16(4)	15(10)	26 (5)		
				-0.95(4)	66 (3)	15 (2)		
			21.6	-0.35(3)	63 (1)	16 (1)	2.55	T_c = 1.4K
G10.315-0.150	$18^h96^m00^s.1$	-20°05'47"	18.3	0.10(3)	12.2(3)	2.5(7)	0.77	
				-0.13(6)	20.6(2)	2.0(8)		
				-0.06(4)	27.1(4)	3 (1)		Uncertain
G10.2-0.3	18 06 21.0	-20 20 06	18.3	0.27(2)	9.3(2)	6.4(4)	0.77	
				-0.15(4)	17.1(2)	1.6(5)		
				-0.08(3)	27 (1)	7.5(9)		
				-0.11(3)	37.1(2)	1.5(7)		
W31	18 07 30.6	-19 56 30	18.3	0.16(11)	-2.7(1)	6.5(3)	1.53	
				-0.079(7)	29 (1)	26 (2)		Probably multiple components; T_c = 0.67 K
			21.6^b	<0.06	-	-	0.55	
W33	18 11 18.0	-17 56 46	18.3	-0.04(1)	24 (5)	37(10)	0.77	Probably multiple components; T_c = 3.1 K
				0.49(2)	35.8(1)	3.7(2)		
G12.909-0.277	18 11 48.0	-17 53 25	18.3	-0.023(5)	-1 (2)	8 (3)	0.77	Uncertain
				-0.020(6)	31 (1)	6 (2)		Uncertain
				0.08(1)	36 (1)	6 (1)		
M17	18 17 31.9	-16 13 05	18.3	0.14(3)	19.4(5)	4.5(8)	0.77	T_c = 8.1 K
				-0.25(4)	23.9(3)	0.7(4)		Unresolved
Serpens	18 27 25.0	01 12 40	18.3	0.15(2)	8.04(7)	1.3 (2)	0.77	
3C385	18 35 32.6	-06 50 28	18.3	<0.063	-	-	1.63	
G30.539+0.024	18 44 22.9	-02 10 25	18.3	<0.087	-	-	0.64	
W43	18 45 00.4	-01 59 16	18.3	-0.04(2)	6.1 (7)	2 (1)	0.77	
				-0.14(4)	13.8(4)	2 (1)		
				-0.04(1)	67 (2)	14 (3)		Probably multiple components
				-0.16(3)	82.9(3)	2 (1)		
				0.04(2)	93 (1)	9 (2)		
G34.3+0.1	18 50 47.6	01 10 57	18.3	-0.05(1)	12 (1)	5 (1)	0.77	
				-0.04(1)	27 (1)	3 (1)		

(continued on next page)

Table 3.2

(continued)

Source	RA(1950)	DEC(1950)	Frequency (GHz)	T_A^a (K)	Vlsr km s^{-1}	dV km s^{-1}	resolution km s^{-1}	Coments
				0.012(2)	57.1(3)	3.8(3)		
				-0.04(1)	60.9(2)	1.3(3)		Uncertain
G35.2-1.8	$18^h59^m15^s.0$	01°08'58"	18.3	<0.042	-	-		
W49N	19 07 49.6	09 01 15	18.3	0.11(2)	3 (1)	5 (1)	0.77	T_C = 3.3 K
				0.20(2)	11.5(8)	5 (1)		
				-0.19(3)	15.0(7)	1.3(5)		
				-0.38(5)	18.2(5)	1.2(4)		
				-0.20(2)	33.5(7)	3.0(4)		
				-0.36(5)	39 (1)	2.4(3)		
				-0.13(2)	54 (1)	3.0(6)		
				-0.24(4)	60 (1)	3.9(6)		
				-0.28(4)	63 (1)	2.7(5)		
				-0.06(2)	68 (1)	4.0(3)		
			21.6	-0.038(6)	11 (1)	13 (2)	1.08	T_C = 4.4 K
				-0.014(6)	35 (2)	12 (3)		
				-0.029(8)	62 (2)	8 (1)		
W49S	19 07 58.0	09 00 05	18.3	0.11(1)	11 (1)	6 (1)	0.77	T_C = 3.5 K
				-0.07(3)	18.2(5)	0.07(3)		
				-0.11(2)	34.8(8)	4.0(8)		
				-0.20(2)	40.3(4)	2.8(3)		
				-0.032(9)	60 (2)	23 (3)		
G49.2-0.3	19 20 43.0	14 10 49	18.3	<0.082	-	-	0.77	
G49.4-0.3	19 20 54.3	14 21 07	18.3	0.09(1)	51.8(2)	3.0(5)	0.77	
				-0.13(1)	63.8(2)	3.2(4)		
W51N (IRS2)	19 21 22.3	14 25 16	18.3	-0.13(2)	6.0 (7)	3 (1)	0.77	T_C = 6.25 K
				-0.17(2)	45.5(3)	0.8(3)		the site of W51d
				0.32(3)	57 (1)	11 (1)		
				-0.15(3)	66 (2)	0.9(3)		
W15Main/South	19 21 26.3	14 24 35		-0.11(1)	6.0 (5)	3 (1)	0.77	the site of W51e1,e2
				-0.12(3)	45.5(4)	0.8(3)		
				0.29(4)	57 (2)	12 (2)		
				-0.17(3)	66 (2)	0.9(2)		
K3-50	19 59 50.0	33 24 18	18.3	0.064(8)	-24.8(4)	6.5(9)	0.77	
			21.6[b]	<0.063	-	-	0.90	
ON-1	20 08 10.0	31 22 40	18.3	0.042(8)	10.7(4)	3 (1)	0.77	
ON-2 (2)	20 19 51.5	37 17 00	18.3	0.06(1)	0.3 (1)	1.9(5)	0.77	

(continued on next page)

Table 3.2

(continued)

Source	RA(1950)	DEC(1950)	Frequency (GHz)	T_A[a] (K)	Vlsr km s^{-1}	dV km s^{-1}	resolution km s^{-1}	Comments
S106	$20^h25^m23^s.7$	37°13'00"	18.3	0.03(1)	-8.0(4)	2.5(9)	0.77	
				0.16(1)	-1.3(1)	1.7(2)		
				0.05(1)	3.5(3)	2.5(6)		
W75N	20 36 50.0	42 26 58	18.3	0.08(4)	-3.5(3)	4.0(5)	0.77	
				0.08(1)	9.5 (3)	3.8(5)		
DR21	20 37 14.0	42 08 54	18.3	0.25(2)	-2.2(2)	2.6(4)	0.77	
				-0.15(3)	7.6 (4)	2.6(9)		
			21.6[b]	-0.15(1)	-2.1(1)	3.4(3)	0.90	
DR21(OH)	20 37 15.0	42 12 08	18.3	0.26(1)	-2.5(3)	3.1(3)	0.77	
				-0.07(2)	5.3 (3)	1.3(3)		
				0.05(1)	9.3 (3)	2.5(3)		uncertain
			21.6[b]	-0.034(7)	-2.1(3)	2.9(7)	0.54	
S140	22 17 41.2	63 03 41	18.3	0.076(6)	-7.8(2)	3.8(4)		
S142	22 48 25.0	57 50 30	18.3	<0.031	-	-	0.77	
Ceph A	22 54 19.0	61 45 47	18.3	0.043(9)	-10.2(3)	3.2(7)	0.77	
NGC7538	23 11 36.6	61 11 48	18.3	0.062(6)	-55.9(4)	7.6(9)	0.77	
			21.6	<0.072	-	-		
Cas A	23 21 10.0	58 32 24	18.3	-0.36(4)	-46 (1)	2.5(3)	0.77	Perseus arm; T_C = 8.8 K
				-0.29(5)	-39 (1)	2.5(8)		"
				-0.36(5)	-36 (1)	2.0(5)		"
				-0.37(6)	-0.8(5)	0.9(3)		Orion spiral arm
				-0.43(7)	0.6 (4)	1.0(4)		"
			21.6	-0.036(4)	-47 (1)	3 (1)		Perseus arm; T_C = 6.2 K
				-0.019(5)	-37 (2)	7 (2)		"
				-0.025(3)	-1 (1)	3 (1)		Orion spiral arm
(b) Dark Clouds								
B1	03 30 16.3	30 57 26	18.3	0.55(2)	6.68(5)	1.28(6)	0.16	
			21.6	-0.05(5)	6.6(5)	1.1(5)	0.23	
B5	03 44 28.7	32 44 33	18.3	0.48(2)	10.15(1)	0.41(2)	0.096	
L1498	04 07 50.0	25 02 13	18.3	1.97(9)	7.78(1)	0.27(2)	0.040	
			21.6	-0.35(8)	7.77(1)	0.21(3)	0.068	
L1495	04 11 06.5	28 01 53	18.3	0.73	6.84(1)	0.24(1)	0.19	
			21.6	<0.28	-	-	0.091	
B217	04 24 42.5	26 11 13	18.3	0.85(3)	6.98(1)	0.28(2)	0.19	

(continued on next page)

Table 3.2

(continued)

Source	RA(1950)	DEC(1950)	Frequency (GHz)	T_A^a (K)	Vlsr km s^{-1}	dV km s^{-1}	resolution km s^{-1}	Coments
L1551	$04^h28^m40^s.2$	18°01'45"	18.3	0.32(1)	6.54(2)	0.84(4)	0.38	
TMC-2A	04 28 54.0	24 26 27	18.3	0.66(3)	5.88(1)	0.27(2)	0.19	
TMC-1(-4,6)	04 38 20.3	25 41 45	18.3	1.60(4)	5.80(3)	0.61(4)	0.081	NH_3 peak position
			21.6	-0.35(5)	5.82(6)	0.56(6)	0.068	
TMC-1C	04 38 11.9	25 44 02	18.3	1.58(7)	5.7(3)	1.6(3)	0.160	
TMC-1(0,0)	04 38 38.6	25 35 45	18.3	1.8 (4)	5.8(3)	0.59(4)	0.48	Multiple components;
			21.6	-0.54(7)	5.82(1)	0.53(4)	0.081	Cyanopolyyne peak
L1517B	04 52 07.2	30 33 18	18.3	0.87(4)	5.81(1)	0.26(1)	0.048	
L1512	05 00 54.4	32 39 00	18.3	1.13(3)	7.11(1)	0.16(3)	0.19	Not resolved
L1544	05 01 14.0	25 07 00	18.3	1.11(6)	7.18(1)	0.43(4)	0.19	
L134N	15 51 30.3	-02 43 31	18.3	0.81(8)	2.36(1)	0.25(3)	0.19	
			21.6	-0.19(2)	2.39(1)	0.26(3)	0.81	
	15 51 33.9	-02 40 30	18.3	1.18(4)	2.43(1)	0.22(1)	0.19	C_3H_2 peak position
			21.6	-0.35(3)	2.42(1)	0.23(2)	0.081	
Rho Oph B	16 24 10.0	-24 22 42	18.3	0.31(5)	3.57(8)	1.33(9)	0.096	
	16 24 13.2	-24 24 00	18.3	0.44(7)	3.47(6)	0.89(7)	0.096	
L1689	16 29 20.6	-24 22 09	18.3	0.60(8)	3.84(6)	0.64(8)	0.081	
			21.6	-0.5(2)	3.8(1)	0.6(1)	0.136	
L379(3)	18 26 36.4	-15 17 47	18.3	0.140(8)	18.70(7)	2.7 (2)	0.19	
			21.6	<0.05			0.19	
L778	19 24 26.4	23 52 37	18.3	0.42(4)	10.02(2)	0.46(5)	0.19	
			21.6	-0.19(8)	10.06(5)	-	0.081	Line width uncertain
B335	19 34 35.0	07 27 30	18.3	0.48(2)	8.29(1)	0.39(2)	0.096	
			21.6	-0.136(9)	8.33(2)	0.40(4)	0.081	
L1155H	20 42 36.0	67 35 33	18.3	<0.093	-	-	0.19	
L1082A	20 52 22.2	60 03 20	18.3	0.24(4)	-2.20(3)	0.32(7)	0.19	
L1174	20 59 46.3	68 01 04	18.3	0.35(3)	2.79(4)	1.07(9)	0.19	
L1172B	21 01 48.6	67 42 13	18.3	0.65(5)	2.83(2)	0.46(5)	0.19	
			21.6	-0.14(3)	2.81(3)	0.33(7)	0.091	
B361	21 10 28.0	47 11 00	18.3	<0.05	-	-	0.19	
			21.6	<0.05	-	-	0.19	
B163	21 40 32.6	56 29 17	18.3	<0.05	-	-	0.19	
			21.6	<0.06	-	-	0.19	
N7129S	21 41 50.5	65 49 39	18.3	<0.05	-	-	0.19	
			21.6	<0.05	-	-	0.19	

(continued on next page)

Table 3.2

(continued)

Source	RA(1950)	DEC(1950)	Frequency (GHz)	T_A^a (K)	Vlsr km s^{-1}	dV km s^{-1}	resolution km s^{-1}	Coments
LKH234	$21^h41^m57^s.2$	65°53'04"	18.3	<0.04	-	-	0.19	
			21.6	<0.05	-	-	0.19	
N7129N	21 41 57.5	65 54 20	18.3	<0.05	-	-	0.19	
			21.6	<0.06	-	-	0.19	
L1031C	21 44 24.0	47 05 00	18.3	<0.080	-	-	0.19	
L1031B	21 45 32.0	47 18 12	18.3	0.42(3)	4.07(3)	1.07(8)	0.19	
			21.6	-0.10(4)	3.98(3)	1.2 (1)	0.16	
L1262	23 23 32.2	74 01 45	18.3	0.58	3.95(1)	0.41(1)	0.19	
			21.6	-0.11(2)	3.92(4)	0.4 (1)	0.091	
L1253	23 53 40.7	58 16 59	18.3	<0.04			0.19	Possible .1 K feature at -1 km s^{-1}
			21.6	<0.04			0.19	
(c) Stellar Objects								
HD29647	04 38 03.8	25 53 51	18.3	0.035(5)	5.7 (1)	1.6 (2)	0.63	
			21.6	<0.023	-	-	0.14	
R Mon	06 36 26.0	08 47 04	18.3	<0.029	-	-	0.77	
IRC+10216	09 45 14.8	13 30 39	18.3	0.014(3)	-24 (4)	30 (3)	3.1	
			21.6	<0.002	-	-	10.2	
CIT6	10 13 11.0	30 49 17	18.3	<0.011	-	-	12.3	
S Oph	16 34 24.0	-10 28 00	18.3	<0.074	-	-	0.38	
NML Cyg	20 44 33.9	39 55 58	18.3	<0.058	-	-	0.38	
CRL2688	21 00 20.0	36 29 45	18.3	<0.047	-	-	0.38	
HD208501	21 53 12.0	56 22 26	18.3	<0.053	-	-	0.38	
R Cas	23 55 51.7	51 06 36	18.3	<0.071	-	-	0.38	

(continued on next page)

Table 3.2

(continued)

Source	RA(1950)	DEC(1950)	Frequency (GHz)	T_A[a] (K)	Vlsr km s^{-1}	dV km s^{-1}	resolution km s^{-1}	Coments
(d) Miscellaneous								
NGC253	$00^h45^m04^s9$	-25 33'53"	18.3	<0.012	-	-	12.3	
IC342	03 41 58.6	67 56 26	18.3	<0.006	-	-	12.3	
3C123	04 33 55.2	29 34 14	18.3	-0.029(8)	3.5 (8)	5.0 (9)	0.77	T_c = 0.55 K
P/Halley	04 37 41.1	22 18 20	18.3	<0.014	-	-	0.38	Coordinates for 11/9/85
IC443	06 14 15.0	22 26 50	18.3	<0.020	-	-	1.53	
M82	09 51 42.0	69 54 56	18.3	<0.003	-	-	12.3	
NGC5236	13 34 12.0	-29 36 40	18.3	<0.008	-	-	12.3	

Notes to Table

Numbers in parentheses are 1σ error estimates. Where no detections were made upper limit values are the 3σ T_{rms} vlaues.

[a] Antenna temperatures are corrected for the telescope gain which is function of hour angle. Atmospheric opacity corrections have also been applied.

[b] Observations made at NEROC. All others were done at NRAO.

Table 3.3

C_3H_2 $2_{12}-1_{01}$ and $2_{11}-2_{02}$ Observations

Source[a]	Frequency[b] (GHz)	T_A^{*c} (K)	Vlsr (km s-1)	dV (km s-1)	Resolution (km s-1)	Comments
(a) Galactic Continuum Regions						
Orion KL	85.3	0.25(2)	8.3 (2)	3.9 (2)	0.35	
	46.8	<0.08	-	-	6.42	
Orion 3N	85.3	0.48(6)	9.3 (3)	1.8 (4)	0.35	
Sgr B2	85.3				0.35	Self absorbed profile. Emission covers
	46.8	<0.05	-	-	6.40	40 - 90 km s^{-1}; minimum at 60 km s^{-1}
						See figure 17.
W49N	85.3	0.15(3)	7(1)	15.4(9)	2.00	Emission is a blend of 2 components.
		-0.03(2)	15(1)	3 (2)		Absorption shows complex velocity
		-0.03(1)	32(1)	3 (2)		structure. Other features may exist.
		-0.05(1)	40(1)	3 (2)		
		-0.04(1)	60(1)	12(2)		
	46.8	<0.06	-	-	6.40	
W51N(IRS2)	85.3	0.30(5)	60 (2)	10 (2)	0.88	
	46.8	<0.05	-	-	6.42	
DR21	85.3	0.32(5)	-2.5 (6)	3.6 (3)	0.35	
DR21 (OH)	85.3	0.30(5)	-3.1 (8)	3.6 (3)	0.35	
(b) Dust Clouds						
L1498	85.3	1.46(7)	7.8 (5)	0.3(1)	0.04	
TMC-1	85.3	2.2 (2)	5.88(8)	0.61(2)	0.18	
	46.8	1.2 (2)	5.76(5)	0.58(8)	0.08	
L134N(2)	85.3	0.9 (1)	2.2 (1)	0.4 (2)	0.18	
	46.8	0.24(4)	2.2 (2)	0.45(3)	0.16	
Rho Oph B	85.3	0.75(5)	3.47(10)	0.41(13)	0.88	
L1689	85.3	0.5 (1)	4.0 (2)	1.0 (5)	0.35	
B335	85.3	0.90(2)	8.25(8)	0.49(10)	0.09	
	46.8	0.3 (1)	8.3 (2)	0.2 (1)	0.08	
Cas A	85.3	0.04(2)	-42 (6)	15 (8)	0.35	Coordinates: RA: $23^h21^m00^s$; DEC: 58°32'40"
(c) Stellar Objects						
IRC+10216	85.3	0.66(7)	-17 (3)	24 (5)	3.52	
	46.8	<0.05	-	-	6.42	

(continued on next page)

Table 3.3

(continued)

Notes to Table

Numbers in parentheses are 1σ error estimates. Where no detections were made upper limit values are 3σ T_{rms} value.

[a] Source coordinates are given in Table

[b] Transition quantum numbers are in Table

[c] T_A^* is the antenna temperature calibrated by the chopper wheel method and is corrected for atmospheric attenuation.

the C_3H_2 velocity components closely resemble those of H_2CO (Bieging, Wilson, and Downes 1982).

Table 3.2 lists the source positions (1950 coordinates), the transition identified by the approximate frequency from Vrtilek, Gottlieb, and Thaddeus (1987), the antenna temperature calibrated by a noise tube and corrected for antenna gain variations and atmospheric attenuation (T_A), the central velocity (V_{LSR}), the linewidth at half intensity (dV), and the velocity resolution of the observation. The atmospheric corrections rarely amounted to more than 5% at the zenith at NRAO and Haystack. The emission or absorption character of the feature is indicated by the sign of the antenna temperature. In those cases where the continuum antenna temperature was determined, this is also given in the Comments column as T_C. If the $2_{11}-2_{02}$ line was not detected in a particular source, the 3 σ rms value is indicated under the T_A column.

For the millimeter wavelength observations from FCRAO listed in Table 3.3, the positions of the sources and the nomenclature are identical to those of Table 3.2 unless otherwise indicated. The tables have been subdivided by source type and ordered by increasing right ascension within each section. The categories are somewhat loosely defined. The majority of the sources appear under the heading "galactic continuum and star formation regions" and are chosen from various lists of well known HII regions and giant molecular clouds, outflow regions, galactic continuum objects with strong H_2CO absorption features, and at least one supernova remnant (Cas A). The

dust cloud source positions are mostly those of the densest cloud positions as determined by mapping in other molecular lines. Under the subheading "stellar objects" are included a few stars with known circumstellar molecular emission, as well as some which exhibit optical absorption features due to intervening material. Finally, we have grouped remaining miscellaneous objects together; this subgroup includes four external galaxies, one quasar (3C123), one galactic shock front where a supernova remnant (IC443) appears to interact with ambient molecular material, and one comet (P/Halley).

We shall not comment on the results for all the sources listed in the tables, but it is instructive to describe the spectra for a sample of representative and well-studied objects. Other spectra which are not discussed here are illustrated in Figure 3.1.

3.3.1 Cold, Dark Clouds

The properties of dense cores in nearby dark clouds have been summarized by Myers (1985). Among the most studied of such regions are TMC-1 and L183 (commonly referred to as L134N).

3.3.1.1 TMC-1

The complex of nearby (~140pc; Cernichero and Guélin 1987), rather low mass clouds in Taurus includes the prototypical dark cloud, Heiles cloud 2 (Heiles 1968). Schloerb and Snell (1984) have

shown that the gross structure of this object may be characterized as a rotating ring, of the type predicted by numerical calculations for molecular cloud collapse prior to fragmentation and star formation. One of the sub-condensations within Heiles Cloud 2 is the dense filament TMC-1, which itself appears to be fragmenting into still smaller units (e.*g.*, Schloerb, Snell, and Young 1983; Guélin 1985; Hjalmarson and Friberg 1988). Numerous studies have shown TMC-1 to be a chemically complex region particularly rich in molecular species, with the ISM's highest known abundances for carbon-rich molecules such as the cyanopolyynes (Irvine *et al.* 1985; Avery, MacLeod, and Broten 1982; Winnewisser 1981; Bujarrabal *et al.* 1981). Previous observations have shown that the strongest emission from many complex molecules in TMC-1 originates from an elongated cloudlet approximately 1'5 wide and about 5'-10' long with a southeast - northwest orientation.

The many C_3H_2 transitions for which we have data in TMC-1 (Madden *et al.* 1986) together illustrate the utility of this molecule as a probe of physical characteristics in interstellar gas, as well as the relatively high abundance of this species.

Figure 3.2 shows the 1_{10}-1_{01} (18.3 GHz) and 2_{20}-2_{11} (21.6 GHz) transitions taken toward the cyanopolyyne peak position in TMC-1 (RA(1950): $4^h38^m38^s6$; DEC(1950): $25^\circ35'45''$; referred to as the (0,0) or center position). Strip maps of these transitions were made along the TMC-1 ridge at 1'8 spacings. The HC_3N J=1-0 transition was observed simultaneous with the 18 GHz C_3H_2 transition. The intensity

Figure 3.1 The $1_{10}-1_{01}$ C_3H_2 transition (18 GHz) observed at NRAO toward various Galactic sources which are not individually discussed in the text. Source coordinates and spectral resolution are given in Table 3.2 Antenna temperatures are corrected for telescope gain and atmospheric opacity.

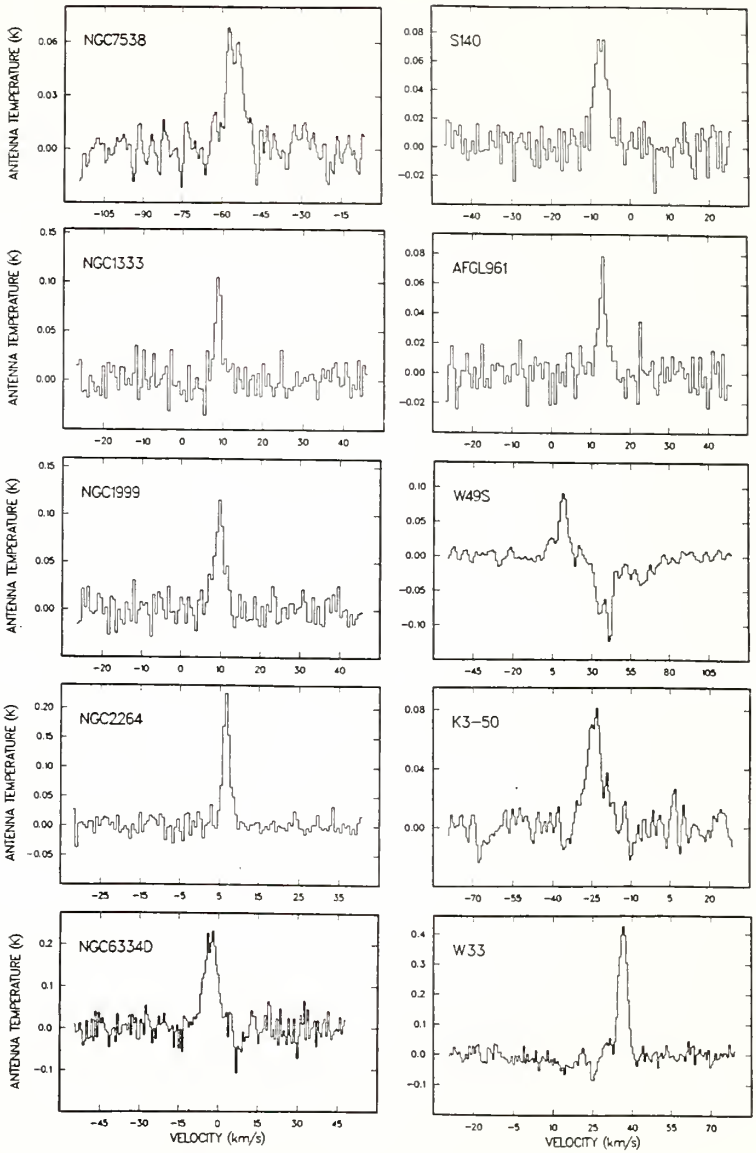
NGC7538
S140
NGC1333
AFGL961
NGC1999
W49S
NGC2264
K3-50
NGC6334D
W33
ANTENNA TEMPERATURE (K)
VELOCITY (km/s)

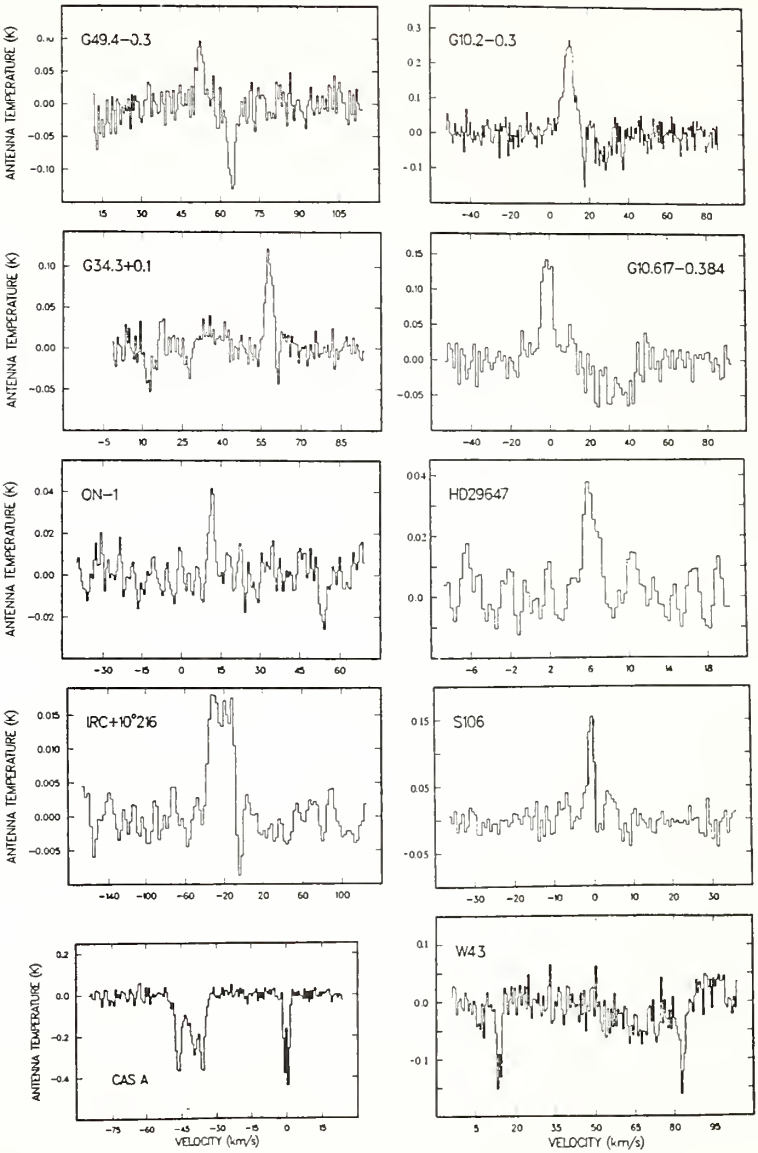
G49.4−0.3
G10.2−0.3
G34.3+0.1
G10.617−0.384
ON−1
HD29647
IRC+10°216
S106
CAS A
W43
ANTENNA TEMPERATURE (K)
VELOCITY (km/s)

Figure 3.2 $1_{10}-1_{01}$ and $2_{20}-2_{11}$ C_3H_2 transitions observed at NRAO toward TMC-1. The coordinates and spectral resolution are listed in Table 3.2 The upward lines in the $2_{20}-2_{11}$ profile, identified by the arrows, are artifacts from the frequency switching observing mode.

TMC−1 C_3H_2

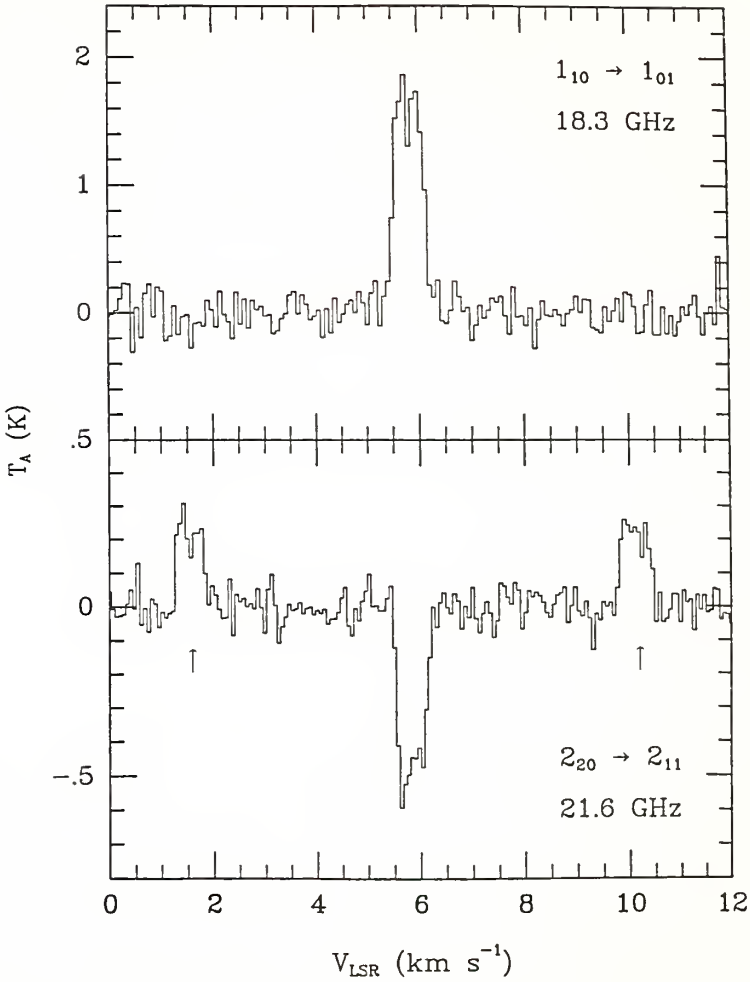
$1_{10} \rightarrow 1_{01}$
18.3 GHz
$2_{20} \rightarrow 2_{11}$
21.6 GHz
T_A (K)
2
1
0
.5
0
−.5
0
2
4
6
8
10
12
V_{LSR} (km s^{-1})

distributions of HC_3N and C_3H_2 along the ridge are similar, with both peaking at the center position. From this map and observations made in a cut across the ridge at the (0,0) position, the C_3H_2 half power source dimensions were determined to be approximately 15' X 1'8, while the HC_3N is slightly less extended (12' X 1'8). Both the narrowness of the ridge (on the scale of our 1.6 arcmin 18 GHz beam) and the SE-NW extention of the ridge are apparent from our limited mapping.

Spatial-velocity contours of the 18 GHz transition (Figure 3.3) demonstrate the velocity structure of the cloudlets along the ridge. Three velocity components are evident: peaking in the southeast is the 5.5 km s^{-1} component; toward the center position [TMC-1(0,0)] two components at 5.7 and 5.9 km s^{-1} contribute somewhat more equally (*cf.* Figure 3.2; HC_3N and C_4H, Tölle *et al.* 1981; Guélin, Friberg and Mezaoui 1982); and toward the north the emission is derived primarily from the higher velocity gas. This velocity gradient is also apparent in the HC_3N and the 21 GHz C_3H_2 spectra, but for the latter case the signal-to-noise is insufficient to distinguish separate velocity components much beyond the center position. The integrated emission in the $1_{10}-1_{01}$ line is slightly less at the "ammonia peak", 4'west and 6'north off-set from TMC-1(0,0), but this may largely be due to differences in the velocity components observed. The ratio of the $[1_{10}-1_{01}/2_{20}-2_{11}]$ integrated intensity along the ridge varies from ~ 2.7 in the south to ~ 3.7 toward the north over the 15' of the ridge mapped.

Figure 3.3 Integrated intensity contours of the $1_{10}-1_{01}$ C_3H_2 transition along the ridge in TMC-1. Offsets in declination are relative to the position given in Table 3.2. The RA offsets range from +5' to -10' relative to the TMC-1(0,0) position.

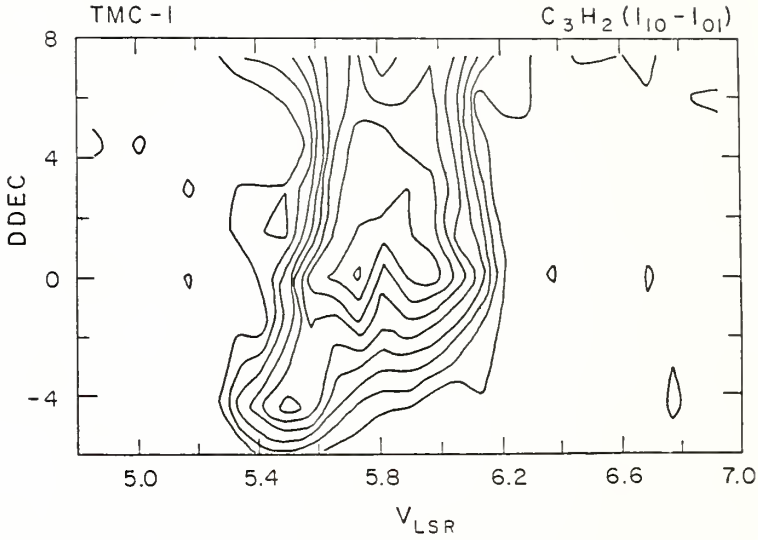
TMC-1
C_3H_2 ($1_{10}-1_{01}$)
8
4
0
-4
DDEC
5.0
5.4
5.8
6.2
6.6
7.0
V_{LSR}

At the peak position we estimate a radiation temperature, T_R, of 7.3 K for the $1_{10}-1_{01}$ line by correcting the observed antenna temperature for a beam efficiency, η_B=0.33, and a filling factor, F, estimated from the map to be 0.75. From observations of the ^{13}C substituted isotope of this transition and the assumption that the ^{13}C isotope is optically thin, Bell *et al.* (1988) derive an optical depth for the main isotope in this transition of 2. This requires the excitation temperature to be about 10 K. Since the kinetic temperature, T_k, in dark clouds like TMC-1 is approximately 10 K (*e.g.* Tölle *et al.* 1981), we see that this 18 GHz transition is both thermalized and optically thick .

For the $2_{12}-1_{01}$ line at 85 GHz, the Einstein A-coefficient is almost two orders of magnitude larger than that of the 18 GHz line: $A(2_{12}-1_{01}) = 2.36\ (10)^{-5}\ s^{-1}$ vs. $A(1_{10}-1_{01}) = 3.90\ (10)^{-7}\ s^{-1}$. Since density estimates for the core of TMC-1 at the center position are n ~ 5 $(10)^4\ cm^{-3}$ (*e.g.* Schloerb, Snell, and Young 1983) we would not expect the higher frequency line to be thermalized. This is in fact confirmed by observation (Figure 3.4). Correcting T_A^* (Table 3.3) for a beam efficiency η_B= 0.56 we find T_R = 3.4 K. From observations of the ^{13}C substituted isotope of this transition, T_{ex} is estimated to be 5.5 K (Gerin *et al.* 1987; Madden *et al.* 1986). This sub-thermal value of T_{ex} is similar to that deduced for other large dipole moment molecules in TMC-1 at mm wavelengths (*e.g.* HC_3N; Avery, MacLeod, and Broten 1982).

Figure 3.4 FCRAO C_3H_2 observations of the 2_{12}-1_{01} and 2_{11}-2_{02} transitions toward TMC-1. Source coordinates and spectral resolution are given in Table 3.3. Antenna temperatures are corrected for atmospheric opacity by the chopper wheel method.

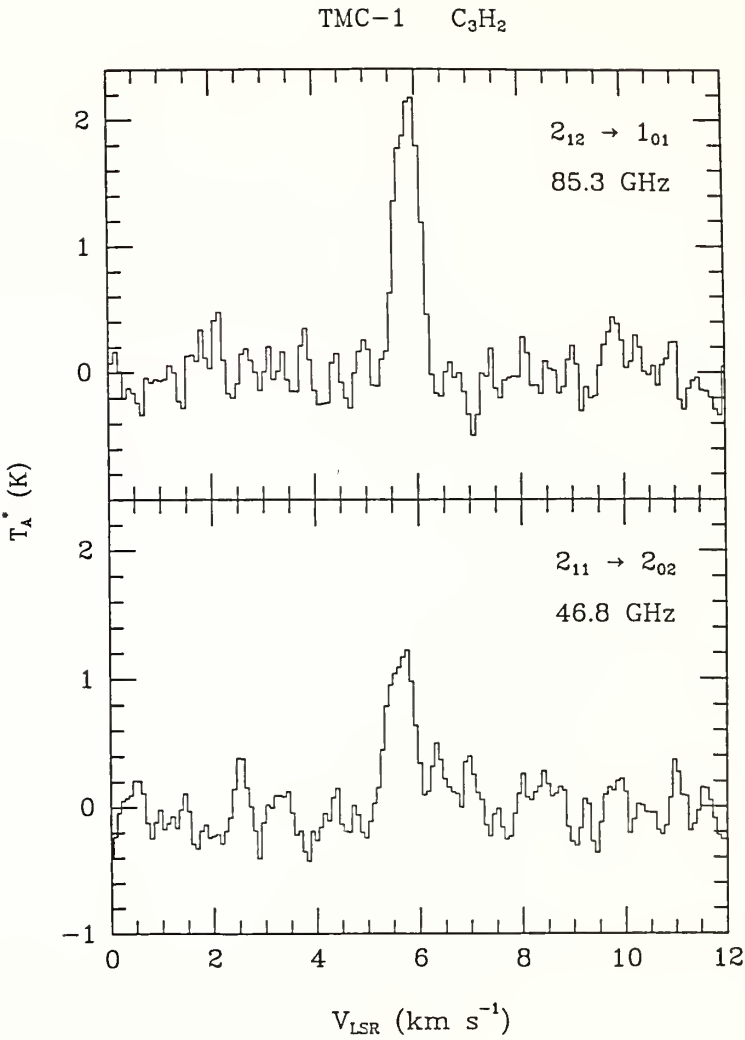
TMC−1 C_3H_2
$2_{12} \rightarrow 1_{01}$
85.3 GHz
$2_{11} \rightarrow 2_{02}$
46.8 GHz
T_A^* (K)
V_{LSR} (km s^{-1})
2
1
0
−1
0
2
4
6
8
10
12

Also the line of the para-species, $2_{11}-2_{02}$ at 46.8 GHz (Figure 3.4), is at least partially saturated in spite of the theoretical 1:3 ratio in statistical weight relative to the ortho species. With η_B=0.58 we find a minimum $T_{ex} \sim 5$ K. Since $A(2_{11}-2_{02}) = 2.72\ (10)^{-6}$, we would expect this transition to be slightly sub-thermal, and we deduce $\tau \sim 1$.

The combined column density in the observed ortho levels (1_{01}, 1_{10}, 2_{12}) is $N = 4\ (10)^{13}\ \eta_B\ \tau_{max}(1_{10}-1_{01})\ cm^{-2}$. Since we have determined that $\tau(1_{10}-1_{01}) \sim 2$ and η_B=0.75, we have a lower limit on the total column density for ortho-C_3H_2 of $6\ (10)^{13}\ cm^{-2}$. By including other low lying levels, we estimate that N (ortho) $\sim 10^{14}$ cm^{-2} at the TMC-1 (0,0) position.

The observed column density for the para-levels is considerably less: $N(2_{20}-2_{11}) \sim 1.3\ (10)^{13}\ cm^{-2}$ for $\tau(2_{11}-2_{02})$=1 and η_B=0.75. Determining the total ortho:para ratio would be interesting. If it is not in thermal equilibrium, information on the formation mechanism of C_3H_2 may be extracted (*cf.* Askne *et al.* 1984). The total column density, both ortho and para, of $\sim 10^{14}$ cm^{-2}, toward TMC-1 (0,0) is consistent with Bell *et al.* (1988) and Cox, Walmsley, and Güsten (1989).

3.3.1.2 L134N

This cloud has also been the object of numerous molecular line studies (*e.g.* Turner 1973; Rydbeck *et al.* 1976), including

mapping in several species (Snell, Langer, and Frerking 1982; Ungerechts, Walmsley, and Winnewisser 1980; Guélin, Langer, and Wilson 1982). A detailed multi-species, multi-transition mapping program has been carried out at FCRAO by Swade *et al.* (1985) and Swade (1989a, 1989b), who estimate an overall mass ~ 190 $M_\odot$, some 15 $M_\odot$ of which is located in a core region. The differences in map appearance for different species suggest that there are real chemical, as well as physical, gradients in the cloud. There also seem to be interesting differences in chemical composition between TMC-1 (where there are enhanced abundances of cyanopolyynes and related species such as C_3O and C_3H; e.*g.*, Irvine *et al.* 1985; Thaddeus *et al.* 1985; Brown *et al.* 1985) and L134N (relatively higher abundances of SO, SO_2, and perhaps NH_3; Irvine, Good, and Schloerb 1983).

The most extensively measured C_3H_2 transition in L134N was the 18 GHz 1_{10}-1_{01} line (Figure 3.5), from which a 37 point map was generated at NRAO (Swade 1989a, 1989b). Seven positions corresponding to peaks in the intensity distributions for one or more of $C^{18}O$ (J=1-0), CS (J=2-1), $H^{13}CO^+$ (J=1-0), and NH_3 (1,1) were observed in the 85 GHz 2_{12}-1_{01} transition (Swade 1989a, 1989b). The C_3H_2 map is quite similar to the NH_3 (1,1) distribution shown in Swade *et al.* (1985), but is not as spatially extended. In addition, the 21 GHz transition, 2_{20}-2_{11}, was detected at the peak C_3H_2 position and is observed in absorption against the 2.7 K background. The 2_{11}-2_{02} 46.8 GHz para transition was observed and detected at a

Figure 3.5 The 1_{10}-1_{01} C_3H_2 (18 GHz) transition observed at NRAO toward L134N. Source coordinates and spectral resolution are given in Table 3.2. Antenna temperatures are corrected for telescope gain and atmospheric opacity.

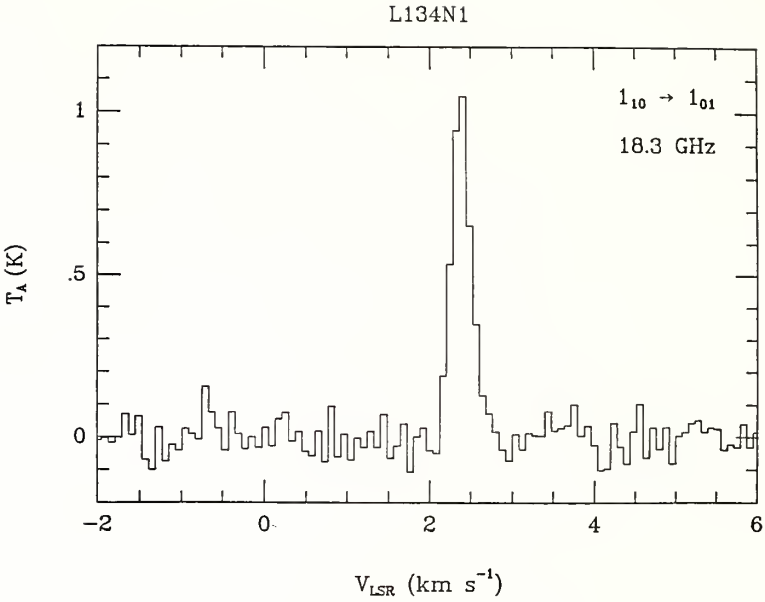
L134N1
$1_{10} \rightarrow 1_{01}$
18.3 GHz
1
.5
0
T_A (K)
−2
0
2
4
6
V_{LSR} (km s^{-1})

lower level than in TMC-1. See Tables 3.2 and 3.33 for the 21 and 46.8 GHz data, respectively.

Since the source is extended relative to our beam, we assume a filling factor for the 18 GHz transition of unity (perhaps a slight overestimate at the C_3H_2 maximum, since the emission is clearly peaked). The maximum position on the $1_{10}-1_{01}$ map then has a radiation temperature of 3.6 K. If this transition is thermalized, as seems likely in view of the excitation of NH_3 and HCO^+, then $\tau(1_{10}-1_{01}) = 0.7$ at this position for a kinetic temperature of 10 K (Snell 1981). At the seven positions where the $2_{12}-1_{01}$ line was observed, the ratio of the radiation temperature in that transition to the radiation temperature of the $1_{10}-1_{01}$ transition is roughly constant, so that both of these transitions may be optically thin in much of this cloud. This is also supported by the fact that the ratios of the different C_3H_2 lines to the 18 GHz line is smaller in L134N than in TMC-1 where the 18 GHz line is known to be saturated.

If we assume that the excitation temperatures of the observed transitions are the same at the peak position, we find a column density of ortho C_3H_2 in L134N that is at most 10-20% of that in TMC-1 and a total column density, assuming LTE, of 2-4 $(10)^{13}$ cm^{-2}. This range in column density takes into account uncertainties in beam filling factors and optical depths and is approximately a factor of 3 greater than that of HC_3N in L134N (Swade 1989a). (For comparision, note that the HC_3N fractional abundance ($N(HC_3N)/N(H_2)$) in L134N is only ~ 3% that of TMC-1). As in the case of TMC-1, C_3H_2 and HC_3N

appear to delineate similar regions. The abundance of C_3H_2 is comparable, for example, to HCN and SO, making it one of the more abundant molecules in L134N (Swade 1989b; Irvine, Goldsmith and Hjalmarson 1987).

3.3.1.3 Other Dark Clouds

We have also observed a number of other dark clouds (see Table 3.2), and detected the $1_{10}-1_{01}$ and $2_{12}-1_{01}$ transitions in all cases where we searched: in most cases we have also detected the $2_{20}-2_{11}$ line, always in absorption. These results are described in the tables. Figure 3.6 shows, for example, the $1_{10}-1_{01}$ transition taken toward 2 dark clouds: L1498 and B335. C_3H_2 is more abundant in the dark clouds where the carbon chain molecules are more abundant, suggesting a possible relation between these molecules and the formation of C_3H_2.

3.3.2 Giant Molecular Clouds - HII Regions

We have observed a number of clouds that may be classified as GMC's, typically with associated HII regions; all have been detected in the $1_{10}-1_{01}$ transition of C_3H_2. Partly because these objects are usually at considerably greater distances than the dark clouds discussed in the previous section, there is a much greater probability for intervening material, with a consequent increase in

Figure 3.6 $1_{10}-1_{01}$ C_3H_2 (18 GHz) transition toward the two dark clouds: L1498 and B335. Source coordinates and spectral resolution are given in Table 3.2. Antenna temperatures are corrected for telescope gain and atmospheric opacity. The downward lines at the locations of the arrows in L1498 are artifacts from the frequency switching observing mode.

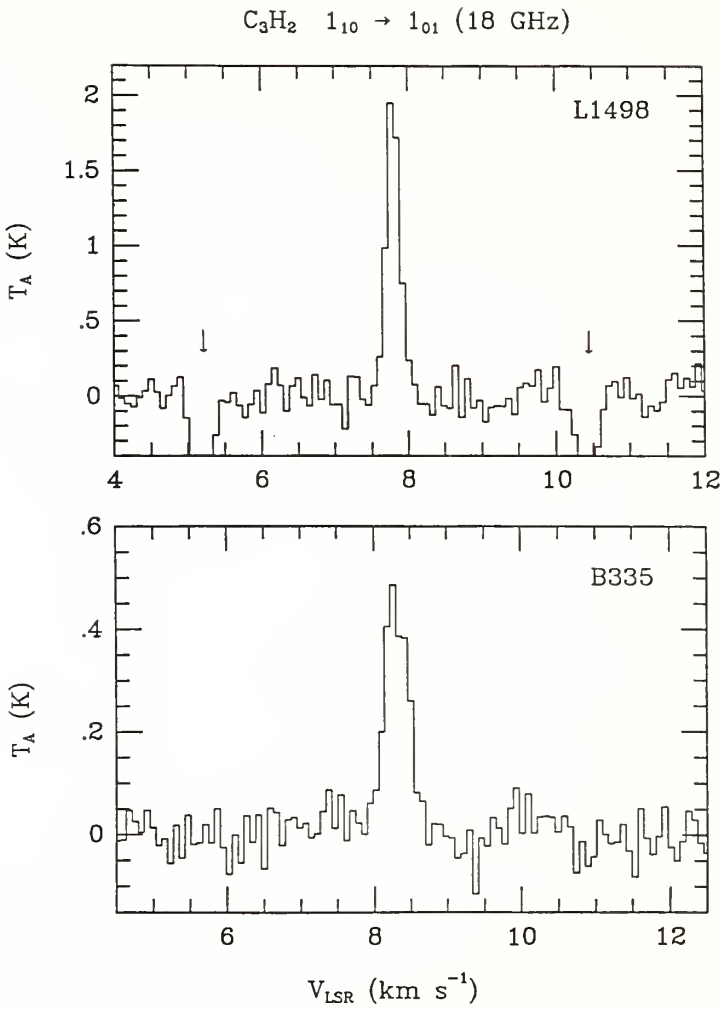
C_3H_2 $1_{10} \rightarrow 1_{01}$ (18 GHz)
L1498
B335
T_A (K)
V_{LSR} (km s^{-1})

complexity of the observed line profiles. In addition, the structures of GMC's are often quite heterogeneous, and it is difficult to resolve regions of differing physical conditions with single dish antennas. In Tables 3.2 and 3.3 we list the individual velocity components of the K-band and mm wavelength lines observed toward our source regions. Absorptions, which are indicated in the tables by negative antenna temperatures, are quite common for the 18 GHz C_3H_2 line, due to the continuum radiation from the HII regions. The 2_{11}-2_{02} transition at 46.8 GHz was searched for in many of these sources but was not detected, while the 2_{12}-1_{01} 85 GHz transition was detected in the HII regions that were searched. A few specific sources with complex profiles are considered in more detail below.

3.3.2.1 W51

The well-studied W51 complex includes a number of discrete radio sources in the Sagittarius spiral arm, which parallels the line of sight for many kpc, resulting in a complexity of projected HII regions and molecular clouds. It is one of the most luminous high-mass star forming regions in the Galaxy. There are two predominant HII regions, W51d and W51e, which are also bright infrared sources, W51(IRS2) and W51(IRS1), respectively (Genzel *et al.* 1982). Each of these regions are associated with a center of activity exhibiting signposts of active massive star formation. These signs include compact HII regions, clusters of H_2O masers,

molecular hydrogen emission and knots of hot $NH_3(3,3)$ gas (Martin 1972; Genzel *et al.* 1979; Beckwith and Zuckerman 1982; Ho, Genzel and Das 1983). The H_2O maser clusters W51 North (W51N) and W51 Main/South (W51M/S) are associated with W51(IRS2) and W51(IRS1), respectively. We will use W51N and W51M/S to designate each activity center.

Our C_3H_2 $1_{10}-1_{01}$ 18 GHz spectra toward W51M/S and W51N along with the 21 GHz $2_{20}-2_{11}$ transition toward W5N are shown in Figure 3.7. Figure 3.8 depicts the $2_{12}-1_{01}$ 85 GHz transition and the HCS^+(J = 1-0) transition toward W51N. Note that the distance between W51M/S and W51N is 70", less than the 90" NRAO beam at 1.4 cm. The two $1_{10}-1_{01}$ profiles show a wide emission feature with peaks at both 57 km s^{-1} and 61 km s^{-1}. In addition, narrow absorption features are observed at 6, 46 and 66 km s^{-1}. The $2_{12}-1_{01}$ 85 GHz profile toward W51N resembles the $1_{10}-1_{01}$ 18 GHz spectrum toward the same position, but the 57 km s^{-1} feature is less pronounced and the absorption features are very weak if detected at all. The $2_{20}-2_{11}$ 21 GHz line toward W51N has absorption maxima at 56, 61 and 66 km s^{-1}. However, the 66 km s^{-1} feature dominates and is wider than in the $1_{10}-1_{01}$ transition. Further, the intensity of the 61 km s^{-1} component is less than the 57 km s^{-1} component in contrast to the other W51N profiles. We did not detect any absorption at 6 or 46 km s^{-1} in this line.

Figure 3.7 $1_{10}-1_{01}$ C_3H_2 (18 GHz) transition toward W51M/S and W51N(IRS2). The $2_{20}-2_{11}$ transition at 21 GHz is observed toward W51N(IRS2). Source coordinates and resolution are given in Table 3.2. Antenna temperatures are corrected for telescope gain and atmospheric opacity.

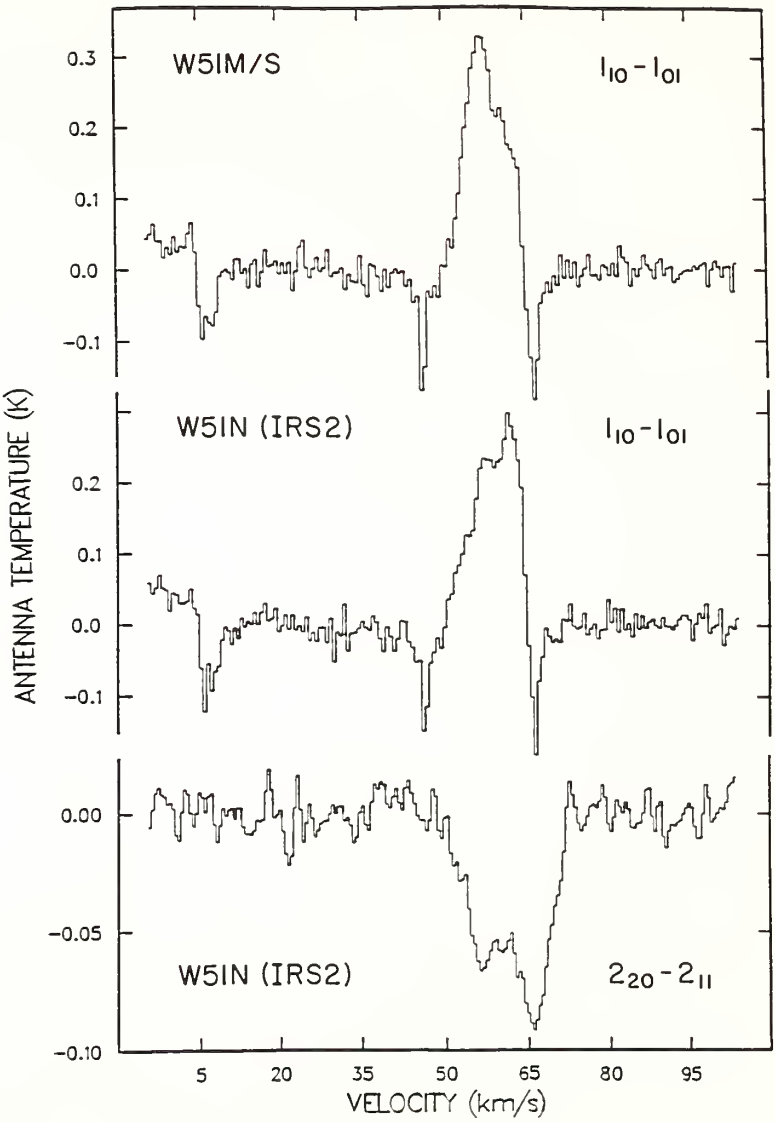
W5IM/S
$1_{10}-1_{01}$
W5IN (IRS2)
$1_{10}-1_{01}$
W5IN (IRS2)
$2_{20}-2_{11}$
ANTENNA TEMPERATURE (K)
VELOCITY (km/s)
0.3
0.2
0.1
0.0
−0.1
0.2
0.1
0.0
−0.1
0.00
−0.05
−0.10
5
20
35
50
65
80
95

Figure 3.8 The $2_{12}-1_{01}$ (85 GHz) transition of C_3H_2 observed toward W51N(IRS2). The HCS^+ J=2-1 line is also observed in the bandpass. Source coordinates and spectral resolution are given in Table 3.2. Antenna temperatures are corrected for atmospheric opacity by the chopper wheel method.

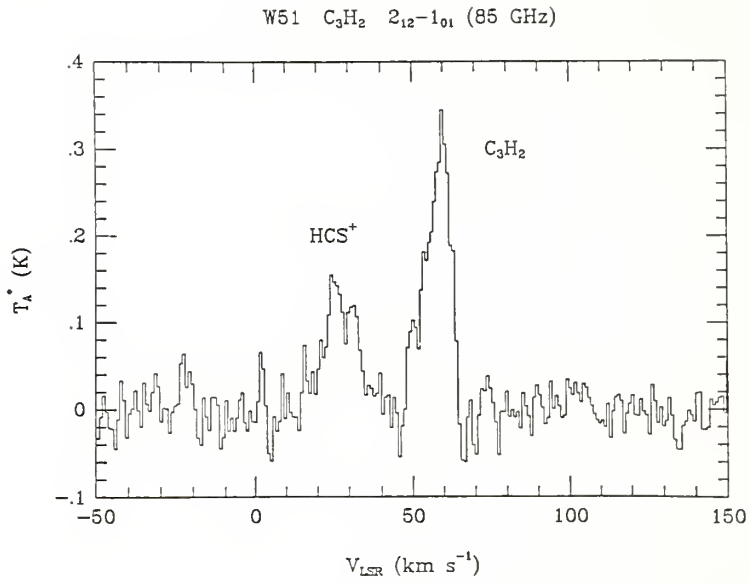
W51 C_3H_2 $2_{12}-1_{01}$ (85 GHz)
C_3H_2
HCS^+
T_A^* (K)
.4
.3
.2
.1
0
−.1
−50
0
50
100
150
V_{LSR} (km s^{-1})

We can explain the increased linewidth in the 66 km s^{-1} feature of the 21 GHz $2_{20}-2_{11}$ line by effects related to beam filling. The $2_{20}-2_{11}$ transition is absorbing the cosmic background and hence we receive contributions from all material within the 90" beam. For the 18 and 85 GHz absorption features, however, material in front of the compact HII regions (few arc seconds in size), is contributing. Hence, any velocity gradients or macro-turbulence will produce the observed increased linewidths. We conclude that the linewidth of the 66 km s^{-1} feature measured over a small region (*eg.* the size of compact HII regions), is only ~ 1 km s^{-1}.

Molecular emission in W51 is usually observed at three velocities: 52, 58 and 70 km s^{-1} (Mufson and Liszt 1979; Nyman 1983). With a wider bandpass, the H109α recombination line is seen at V_{LSR}~ 58 km s^{-1} in the $1_{10}-1_{01}$ spectra, thus associating this velocity component with the vicinity of the HII region (see Downes *et al.* 1980). Since lines from highly excited states of NH_3 are emitted at 57 and 60 km s^{-1} toward W51M/S and W51M (Mauersberger *et al.* 1986), we attribute both of these velocity components observed in C_3H_2 to the W51 region itself. Further, the two dominating velocity components of the easily excited $C^{18}O$ (J=1-0) line are seen at 57 and 60 km s^{-1} and peak at W51M/S and W51N, respectively (Bergman 1988). Hence, when observing W51N with a small beam the 60 km s^{-1} feature should dominate. This is just the case for our 85 GHz line (Figure 3.8).

The 52 km s^{-1} velocity component is prominent in CO (J=1-0, 2-1, 3-2 and 4- 3) and may be self-reversed in the J=2-1 line (Phillips *et al.* 1981; White *et al.* 1986). Emission from ^{13}CO (J=1-0) is also detected at this velocity (Mufson and Liszt 1979). This velocity component is a weak feature in C_3H_2 and could be due to a mixture of emission and absorption. However, since the 21 GHz line, which is expected to exhibit only absorption, is also weak, the most probable reason is simply a lack of C_3H_2 at 52 km s^{-1}. This particular component is probably associated with the nearby HII region G49.4-0.3 (*cf.* Figure 3.1; Bieging, Wilson and Downes 1982). We fail to detect any emission or absorption at 70 km s^{-1}. The absorptions at 6, 46 and 66 km s^{-1} all correspond to absorption features observed in 6 cm H_2CO (Bieging, Wilson and Downes 1982) and HCO^+ J=1-0 (Nyman 1983). Both of the 6 and 46 km s^{-1} lines are due to foreground clouds not in the proximity of W51 (Rydbeck *et al.* 1976, Bieging, Wilson and Downes 1982). The 66 km s^{-1} absorption, which is at a kinematically forbidden velocity, is attributed to gas streaming along the outside of the Sagittarius arm and hence is also foreground material unrelated to W51.

3.3.2.2 Orion A

The Orion A molecular cloud is the nearest region of massive star formation and is one of the most well studied objects in the Galaxy (e.*g.* Glassgold, Huggins and Schucking 1982). Models for the

region include at least 3 distinct kinematic features, with differing molecular emission characteristic of each component (Plambeck *et al.* 1982; Johansson *et al.* 1984a, 1984b; Blake *et al.* 1987). The hot core component is a small, warm, dense region near the embedded infrared source, IRc2. This molecular gas is observed at the characteristic V_{LSR} of 4 to 5 km s^{-1} and has linewidths of 10 to 15 km s^{-1}. The plateau emission at V_{LSR} = 7 or 8 km s^{-1} has linewidths of 20 km s^{-1} or larger probably originating in the material from the outflow of IRc2. The C_3H_2 observations are characteristic of a third distinct component, the ambient molecular ridge, also called the spike component. This narrow emission originates from a ridge of relatively undisturbed molecular gas extending along a N-S axis. At the source of the high velocity plateau outflows, bifurcation in the ridge gas occurs: the N-S ridge of quiescent gas becomes slightly displaced toward the northeast of IRc2 while the velocity here is about 10 km s^{-1}; south of IRc2 the velocity shifts to 8 km s^{-1}. Both clouds have linewidths of about 2 km s^{-1}. Profiles toward IRc2 are usually wider (3-4 km s^{-1}) since both clouds are observed (Bastien *et al.* 1981; Friberg 1983).

A map of the region covering 6' X 3' shows that the C_3H_2 1_{10}-1_{01} 18 GHz emission is extended and exhibits somewhat varying profiles. A peak in antenna temperature is found 3' north and 1' east of KL (Orion 3N1E; Figure 3.9). A map in the 85 GHz transition shows that the 2_{12}-1_{01} line and the HCS^+ (J=1-0) line also peak toward Orion 3N1E where narrow (1.5 km s^{-1}) profiles are observed at 9 km s^{-1},

while the KL region reveals wider, flatter profiles at 8 km s^{-1} (Figure 3.10). This distribution is similar to that seen for a number of other molecular species, including particularly many radicals and ions such as N_2H^+, CN, and HCO^+ (Turner and Thaddeus 1977).

Assuming that the 85 GHz lines are optically thin, in LTE, and the excitation temperature is about 15 to 20 K for high dipole moment species originating from the ambient ridge (Blake *et al.* 1987), we derive a column density for the combined ortho and para C_3H_2 of 8 $(10)^{13}$ cm^{-2} for each of the KL and 3N1E positions using a beam filling factor of 1 and T_{BG} = 2.7 K. This value is consistent with that of Blake *et al.* (1987) and is probably a lower limit for the IRc2 position if the emission arises from the spatially compact ridge source which is estimated to be 30" in diameter (Blake *et al.* 1987). If we assume a filling factor of 0.25 for the 1' FCRAO beam, we derive a column density for the compact ridge source, of 8 $(10)^{13}$ cm^{-2}. The abundance of C_3H_2 in the extended ridge component is similar to those of HC_3N and HCS^+ (Blake *et al.* 1987).

3.3.2.3 M17

M17 is a HII region with strong radio continuum and intense infrared emission, from which its total luminosity is estimated to be 6 $(10)^6$ $L_\odot$ (Harper *et al.* 1976). The HII region is in close proximity to a molecular cloud in the southwest. High angular

Figure 3.9 The $1_{10}-1_{01}$ (18 GHz) C_3H_2 transition observed at NRAO toward two positions in Orion: the KL region and the position 3' north and 1' east of KL (Orion 3N1E). Source coordinates and spectral resolution are given in Table 3.2. Antenna temperatures are corrected for telescope gain and atmospheric opacity.

ORION C_3H_2 $1_{10}-1_{01}$ (18 GHz)

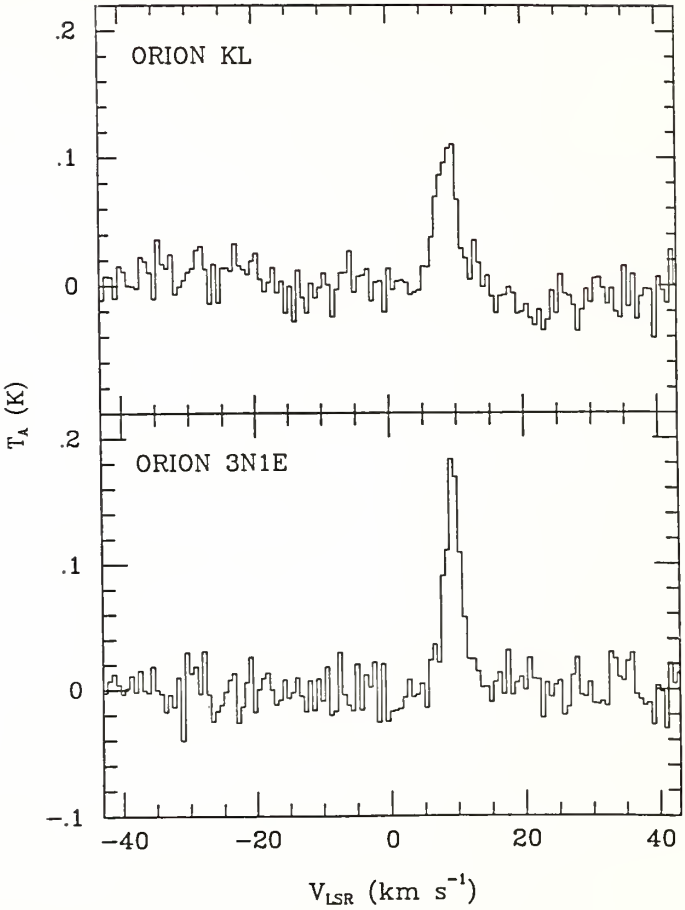

Figure 3.10 The 2_{12}-1_{01} (85 GHz) C_3H_2 transition observed toward Orion KL and the position 3' north and 1' east of Orion KL (Orion 3N1E). The HCS^+ line also in the bandpass is observed at both positions. Source coordinates and spectral resolution are given in Table 3.2. Antenna temperatures are corrected for atmospheric opacity by the chopper wheel method.

ORION C_3H_2 $2_{12}-1_{01}$ (85 GHz)

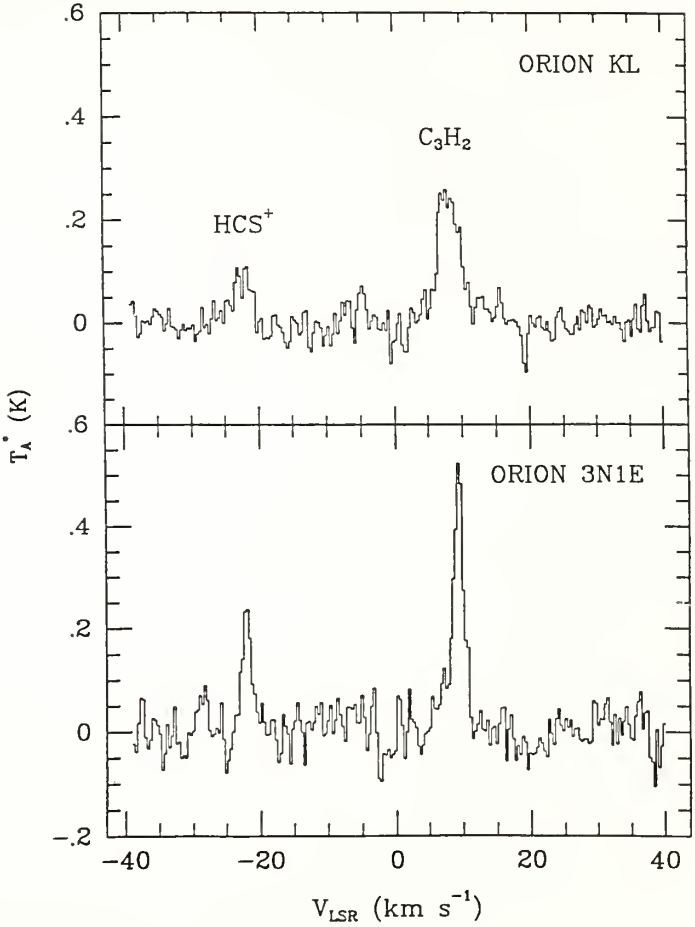

resolution continuum and NH_3 observations have revealed a complex ionization front adjacent to the molecular region (Felli, Churchwell, and Massi 1984; Massi, Churchwell, and Felli 1988; Güsten and Fiebig 1988). The geometry of the HII region-molecular cloud is thought to be viewed edge-on with recent star formation activity found at the interface as evidenced by H_2O masers and a bright 10 μm infrared source (Kleinman and Wright 1973; Jaffe, Güsten, and Downes 1981). From ^{12}CO and ^{13}CO observations there exist at least 2 molecular clouds along the direction towards M17. The more intense molecular emission arises from the larger, extended, $V_{LSR} \sim 20$ km s^{-1} cloud situated to the southwest of the HII region. A 23 km s^{-1} cloud seen in CO and in 6 cm H_2CO observations appears to lie in front of and along the line of sight to the HII region. However, this velocity component appears only at the HII region and is hence spatially correlated with M17 (Lada 1976; Lada and Chaisson 1975; Thronson and Lada 1983). Through multi-transition studies of CS and H_2CO, gas densities of the molecular region are determined to be $\sim 10^6$ cm^{-3} (Snell *et al.* 1984; Mundy *et al.* 1986; Mundy *et al.* 1987).

The C_3H_2 results are consistent with the presently existing molecular data, revealing an emission line at $V_{LSR} = 20$ km s^{-1} which is at least 4.5 km s^{-1} wide, while a narrow, stronger absorption line is detected in the 24 km s^{-1} cloud lying in front of the HII region (Figure 3.11). The narrow absorption feature is from the higher velocity molecular cloud in the foreground along the line of sight to the compact HII region. As a result, some fraction of the

Figure 3.11 The $1_{10}-1_{01}$ (18 GHz) C_3H_2 transition observed toward M17. Source coordinates and spectral resolution are given in Table 3.2. Antenna temperatures are corrected for telescope gain and atmospheric opacity.

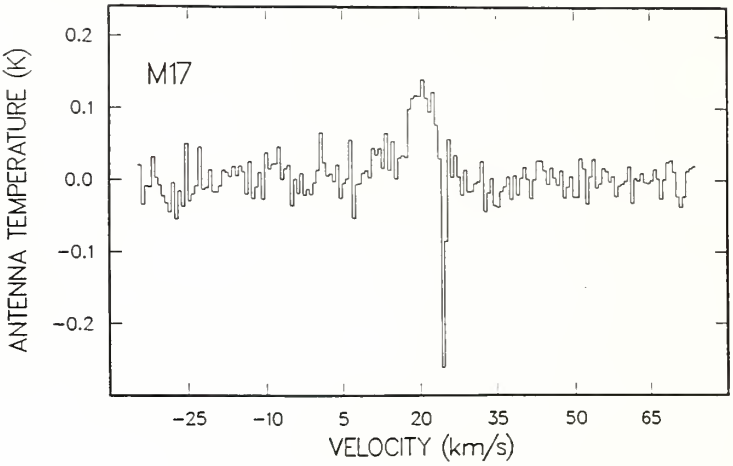
M17
ANTENNA TEMPERATURE (K)
0.2
0.1
0.0
−0.1
−0.2
−25
−10
5
20
35
50
65
VELOCITY (km/s)

M17 emission is absorbed and the emission line width may be somewhat broader. As for W51 the absorption feature in M17 is much narrower than the emission line toward the same position. Lada (1976) gives a linewidth of about 4 km s^{-1} for CO (J=1-0) emission at 23 km s^{-1} while the 18 GHz C_3H_2 and 6 cm H_2CO absorption lines are 0.7 and 0.9 km s^{-1} wide, respectively, at the V_{LSR} of 24 km s^{-1}.

3.3.2.4 DR21/W75N

DR21, DR21(OH) and W75N are a part of the W75 molecular complex in Cygnus. DR21 contains a strong continuum source, while W75N (13' north) is the site of a weak compact continuum source (Wynn-Williams 1971). DR21(OH) (3' north of DR21), in contrast, contains no significant free-free continuum, although it is similar to DR21 at 350 μm (Righini, Simon and Joyce 1976).

CO (J=1-0) maps of the DR21 region show an extended cloud at -3 km s^{-1} which does not extend north of W75N. A narrow 9 km s^{-1} feature peaks at W75N and is evident throughout the complex (Dickel, Dickel and Wilson 1978; Fischer *et al.* 1985). Six cm H_2CO observations also show two velocity features centered at -3 and 9 km s^{-1}. The -3 km s^{-1} H_2CO absorption peaks near the DR21/DR21(OH) region, while the feature at 9 km s^{-1} is concentrated toward W75N (Bieging, Wilson and Downes 1982). In DR21 where compact HII regions produce continuum emission at millimeter wavelengths, HCO^+, HCN and

C_2H are observed in weak absorption at 9 km s^{-1} and stronger emission at -3 km s^{-1} (Nyman 1983; Nyman 1984).

A C_3H_2 $1_{10}-1_{01}$ map of the DR21 complex, shows that the -3 km s^{-1} emission component is extended over the DR21-DR21(OH) region, while the 9 km s^{-1} cloud lies in front of the DR21 continuum source as is evidenced by the absorption peaking at this position in the $1_{10}-1_{01}$ spectrum. The 18 and 85 GHz transitions toward the DR21 and DR21(OH) positions are presented in Figures 3.12 and 3.13. North of DR21, the absorption line diminishes while shifting to ~ 6 km s^{-1} near DR21(OH). There may also be weak emission at 9 km s^{-1} toward this position. In the $2_{12}-1_{01}$ profiles (Figure 3.13), the HCS^+ J=2-1 line is also observed in the bandpass.

The 18 GHz absorption features in DR21 and DR21(OH) have linewidths of about 3 km s^{-1} which are comparable to the linewidths of the emission features. This behavior is in contrast to that of W51, M17 and W3 where the absorption features are much narrower than the emission features. We believe this is due to the fact that the absorption is mainly against the extended HII region of W75. In fact, toward DR21(OH) there are no compact HII regions detected at all. Hence, in this case all of the gas within the antenna beam contributes to the absorption and our explanation for the narrow absorption lines toward the other sources is consistent.

Figure 3.12 $1_{10}-1_{01}$ (18 GHz) C_3H_2 transitions observed at NRAO toward DR21(OH) and DR21. Source coordinates and spectral resolution are given in Table 3.2. Antenna temperatures are corrected for telescope gain and atmospheric opacity.

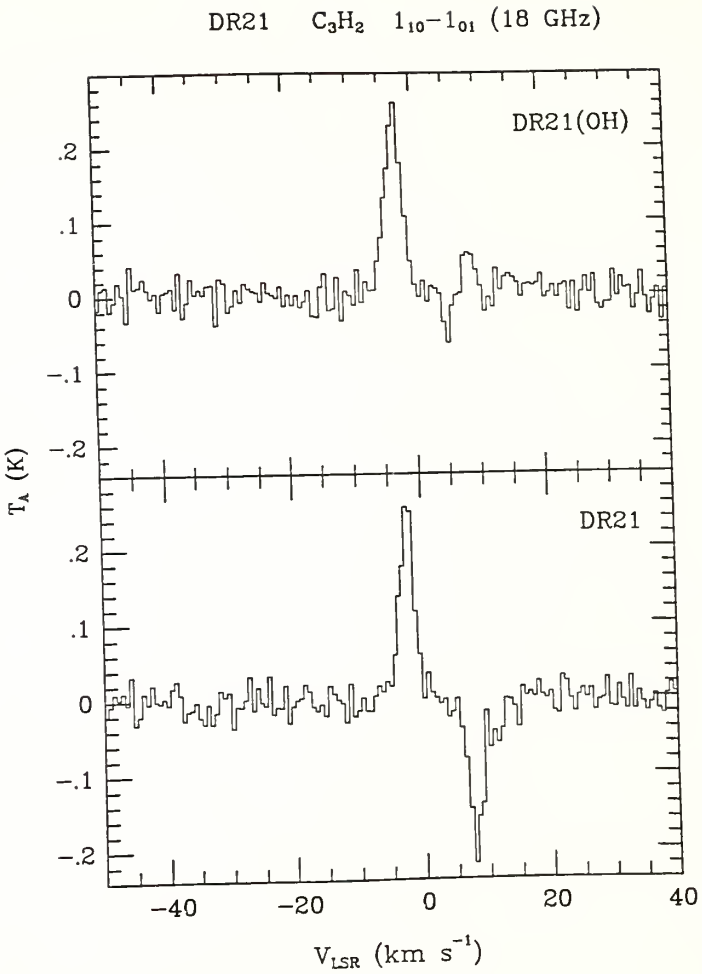
DR21 C_3H_2 $1_{10}-1_{01}$ (18 GHz)
DR21(OH)
DR21
.2
.1
0
−.1
−.2
T_A (K)
−40
−20
0
20
40
V_{LSR} (km s^{-1})

Figure 3.13 The $2_{12}-1_{01}$ (85 GHz) C_3H_2 line observed at FCRAO toward DR21(OH) and DR21. The HCS^+ J=2-1 line is also contained in the bandpass and is observed in both sources. Source coordinates and spectral resolution are given in Table 3.3. Antenna temperatures are corrected for atmospheric opacity by the chopper wheel method.

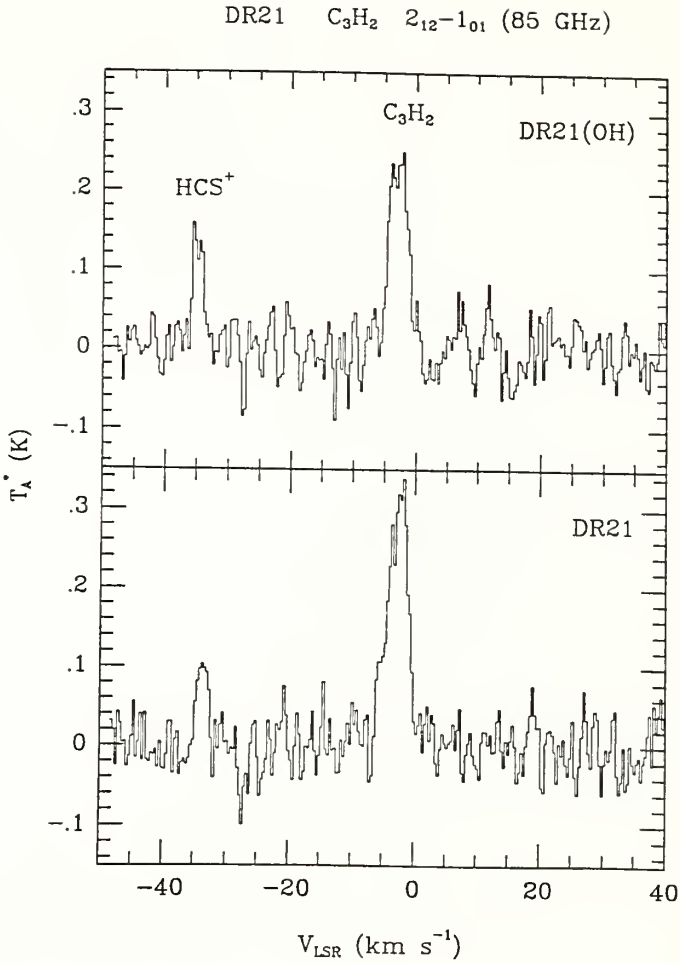
DR21 C_3H_2 $2_{12}-1_{01}$ (85 GHz)
C_3H_2
DR21(OH)
HCS^+
DR21
T_A^* (K)
.3
.2
.1
0
−.1
−40
−20
0
20
40
V_{LSR} (km s^{-1})

3.3.2.5 W3/W3(OH)

W3 is a giant HII region and molecular cloud complex located in the Perseus arm at a distance of about 3 kpc. It contains infrared objects (Wynn-Williams, Becklin, and Neugebauer 1972), radio continuum sources (Colley 1980), OH masers (Gaume 1985), CH_3OH masers (Menten *et al.* 1985) and H_2O masers (Dreher and Welch 1981). Most molecular emission in this massive cloud is observed to lie between -40 and -50 km s^{-1} (*e.g.*, C_2H [Tucker, Kutner and Thaddeus 1974] and NH_3 [Zeng *et al.* 1984; Mauersberger *et al.* 1988]). The distributions of the emission from ^{12}CO, ^{13}CO, CS and HCN were extensively mapped throughout the region, from which Dickel *et al.* (1980) conclude that there are three separate regions with distinct velocities; the brightest is the W3 molecular cloud core, with a $V_{LSR} \sim -40$ km s^{-1}. In addition, an absorption at 20 km s^{-1} is present in 6 cm H_2CO observations and 21 cm HI. This velocity feature is believed to be due to a foreground cloud (Bieging, Wilson and Downes 1982). The only reported emission at this velocity is in CO (J=1-0) having a linewidth of about 3 km s^{-1}.

The W3 18 GHz C_3H_2 profile has a broad 11 km s^{-1} emission feature at -42 km s^{-1} presumed to originate from the core of the W3 molecular cloud (Figure 3.14). In addition a very narrow, 1.2 km s^{-1} wide absorption feature at -21 km s^{-1} is present, apparently from the foreground cloud. Since W3 contains compact HII regions our explanation for the narrow absorption lines in W51 and M17 is also

applicable in this case. C_3H_2 was not detected toward the compact HII region W3(OH).

3.3.2.6 W31

The complex C_3H_2 profile of W31 (Figure 3.15) shows a prominent emission component at -2.7 km s^{-1} and a very broad, ~ 30 km s^{-1} wide, absorption feature centered at ~ 29 km s^{-1} but with considerable structure. This profile resembles that of 6 cm H_2CO, where numerous clouds are seen in absorption in the spiral arms along the line of sight toward W31 at velocities near 10, 17, 23, 28 and 38 km s^{-1} and also at -0.3 km s^{-1}, which is associated with the HII region itself (Downes *et al.* 1980). CO and OH are observed also in the spiral arm clouds near 17 and 30 km/s (Wilson 1974; Wilson *et al.* 1974).

3.3.3 Spiral Arm Clouds

Velocity components characteristic of the clouds traditionally assigned to "spiral arms" between the earth and distant continuum sources are obvious in many of our spectra, including W49 (Matthews and Irvine 1985), W51 (Figure 3.7), Cas A (Matthews and Irvine 1985 and Figure 3.1) and W31 (Figure 3.15). The nature of these absorbing clouds is a matter of some uncertainty. For material at the two

Figure 3.14 $1_{10}-1_{01}$ (18 GHz) C_3H_2 transition observed at NRAO toward W3. Source coordinates and spectral resolution are given in Table 3.2. Antenna temperatures are corrected for telescope gain and atmospheric opacity.

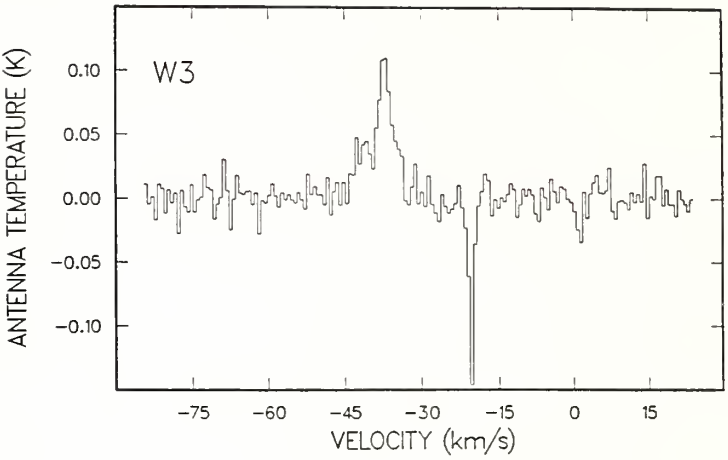
W3
ANTENNA TEMPERATURE (K)
0.10
0.05
0.00
−0.05
−0.10
−75
−60
−45
−30
−15
0
15
VELOCITY (km/s)

Figure 3.15 C_3H_2 $1_{10}-1_{01}$ (18 GHz) observations made at NRAO toward W31. Source coordinates and spectral resolution are given in Table 3.2. Antenna temperatures are corrected for telescope gain and atmospheric opacity.

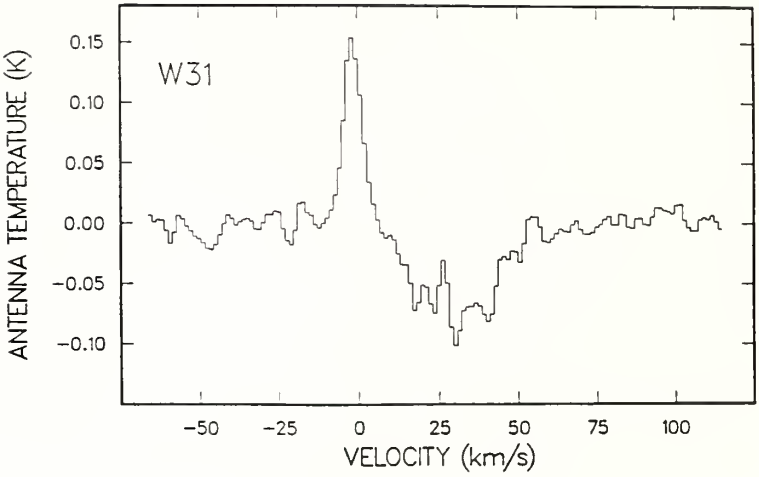
W31
ANTENNA TEMPERATURE (K)
0.15
0.10
0.05
0.00
−0.05
−0.10
−50
−25
0
25
50
75
100
VELOCITY (km/s)

positions in the Sagittarius arm crossed by the line of sight towards W49, Nyman (1983) deduces densities $n(H_2) \sim 10^3$ cm^{-3} from the excitation of ^{13}CO, HCO^+ HCN, and H_2CO. Batrla, Walmsley and Wilson (1984) find from NH_3 observations of the Orion and Perseus arm material seen in absorption against Cas A the slightly higher values $n(H_2) \sim 5\text{-}10$ $(10)^3 cm^{-3}$, with kinetic temperatures T_K=20 K, while Troland, Crutcher and Heiles (1985) estimate $n(H_2) = 1$ - few $(10)^3$ cm^{-3} from CO and ^{13}CO data towards these clouds. These values are intermediate between the hotter, more diffuse gas seen by optical spectroscopy and the cold, dark clouds discussed above. The NH_3 and H_2CO abundances deduced by Batrla, Walmsley and Wilson (1984) are about an order of magnitude less than found in typical dark clouds (see also Irvine *et al.* 1985); in contrast, Nyman (1983) estimates that the molecules which he observed towards W49 were roughly equal in abundance to those found in denser clouds.

Determination of the excitation of C_3H_2 in these clouds would provide important information on their physical state. For example, if the clouds containing C_3H_2 filled our telescope beam towards Cas A and W49N, then the observations of absorption features in the $1_{10}-1_{01}$ transition would require the excitation temperature T_{ex} to be less than 11.5 K and 6 K, respectively (given the measured continuum levels in Table 3.2). The latter value in particular would seem to be substantially sub-thermal, and hence would constrain the density to be less than a few times $(10)^3$ $cm^{-3}$for A = 3.9 $(10)^{-7}$ s^{-1}. Cox, Güsten and Henkel (1987; 1988) have studied C_3H_2 in the diffuse

interstellar medium in line-of-sight clouds toward several continuum regions and conclude that C_3H_2 is an unusual molecule, since in spite of the ultraviolet radiation permeating these regions, it can survive in more diffuse environments than other molecules such as H_2CO.

3.3.4 Circumstellar Envelopes

As reported in Matthews and Irvine (1985), C_3H_2 is found in the envelope of the evolved carbon star IRC+10216, but not in the envelopes of the supergiant NML Cyg, the oxygen-rich R Cas, or the more distant carbon-rich CRL2688. Results are given in the Tables 3.2 and 3.3.

3.3.5 Galactic Center Region

We observed two positions in the direction of the Galactic center: Sgr A and Sgr B2. Our results for the $1_{10}-1_{01}$ line (Figure 3.16) show complex absorption spectra in these directions, which (allowing for the considerable differences in beam sizes) mimic rather closely in their velocity structure the H_2CO absoption spectra obtained by other authors (e.*g*. Whiteoak and Gardner 1974; Downes *et al*. 1980).

Both Sgr A and Sgr B2 have been extensively studied for many years. Sgr A is a strong continuum source very close to the kinematic center of the Galaxy and is thought to be the origin of

Figure 3.16 $1_{10}-1_{01}$ (18 GHz) C_3H_2 observations from NRAO toward the Galactic center sources Sgr A and Sgr B2. Source coordinates and spectral resolution are given in Table 3.2. Antenna temperatures are corrected for telescope gain and atmospheric opacity.

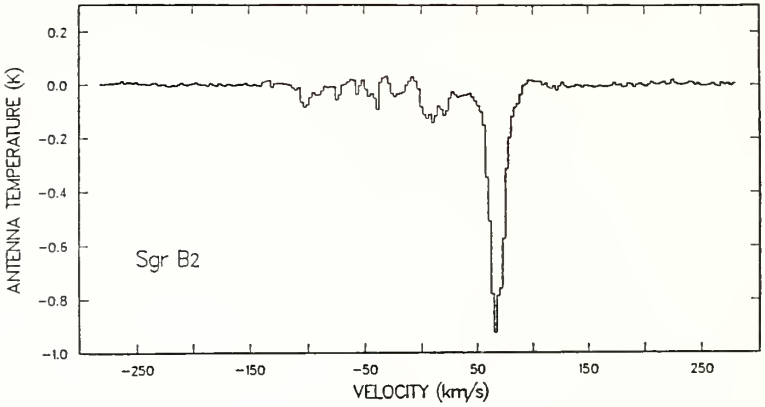
0.2
0.0
-0.2
-0.4
-0.6
-0.8
-1.0
ANTENNA TEMPERATURE (K)
Sgr B2
-250
-150
-50
50
150
250
VELOCITY (km/s)

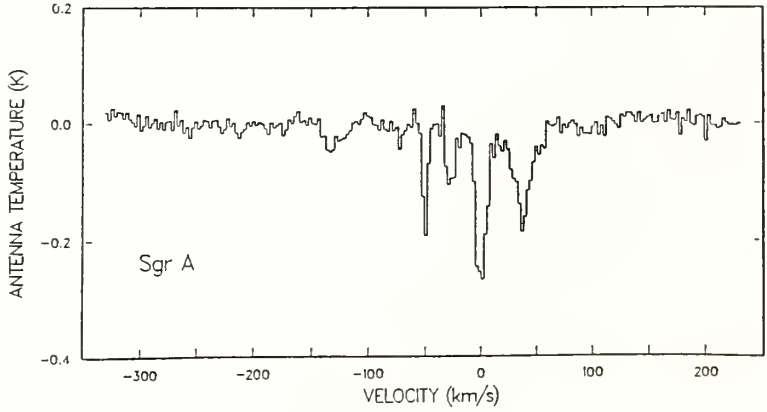
0.2
0.0
-0.2
-0.4
ANTENNA TEMPERATURE (K)
Sgr A
-300
-200
-100
0
100
200
VELOCITY (km/s)

explosive phenomena which have resulted in the non-circular gas motions in the inner parts of the Galaxy (*e.g.*, Oort 1977). Some of the velocity features seen in absorption in our spectrum arise from these expanding arm structures (*e.g.*, those at ~ -50 and -30 km s^{-1}) and are thought to be due to material far from the Galactic Center, as is that giving rise to the strong absorption at ~ 0 km s^{-1}, mostly due to material in the solar neighborhood (Figure 3.16). The precise relationship of any of the other velocity features to Sgr A itself fuels continuing debate (see, *e.g.*, Liszt, Burton and van der Hulst 1985, and for a recent review, Brown and Liszt 1984). However, it is thought that these features arise in gas quite close (within a few hundred parsecs) to the Galactic center. The component at ~ -135 km s^{-1} may be part of an expanding molecular ring (Scoville 1972), while that at ~ 50 km s^{-1} arises in dense molecular clouds which have been studied in many molecular transitions (see, *e.g.*, Güsten and Henkel 1983, Güsten *et al.* 1985, and Walmsley, *et al.* 1986). Our observations of Sgr A include part of the molecular cloud M-0.02-0.07 (Güsten and Henkel 1983) within the beam of the Green Bank antenna.

Sgr B2 is one of the most massive star formation regions in the Galaxy, and, probably because of the large column depths in its surrounding clouds, is exceptionally rich in molecular species. Apart from the longer carbon chains, almost all molecules known in the interstellar medium have been detected in this object; and some have been detected only here. According to Güsten and Downes (1980), Sgr B2 is within 300 pc of Sgr A, and it is possible that one of the

violent events in Sgr A may have triggered the outburst of star formation in Sgr B2 less than $3(10)^5$ years ago. Our spectrum of Sgr B2, taken toward the main continuum peak, shows at least seven identifiable velocity components in absorption in the $1_{10}-1_{01}$ line of C_3H_2 (Figure 3.16). The feature at ~ 60 km s^{-1} arises in the most massive of the molecular clouds closely associated with the HII region, and is the one in which the majority of molecules have been found. There have been numerous attempts to model the temperature and density structure of this cloud (*e.g.* Scoville, Solomon, and Penzias 1975; Avery *et al.* 1979; Goldsmith and Linke 1981; Cummins *et al.* 1983), with varying degrees of success. It is worth noting that the beam averaged peak optical depth of C_3H_2 ($1_{10}-1_{01}$) in the 60 km s^{-1} cloud is approximately 0.5, and this indicates that this transition will almost certainly be optically thick over parts of the source. The remaining absorption features in our spectrum can be assigned as before to various larger scale structures (*e.g.*, Oort 1977), some of which are quite far from the Galactic center and are common also to the Sgr A spectrum.

The $2_{12} - 1_{01}$ spectrum toward Sgr B2 (Figure 3.17) is a complex profile which includes the HCS^+ J=2-1 line. C_3H_2 shows a peak at 53 km s^{-1} and a dip near 60 km s^{-1} indicating self-absorption. A carbon-13 isotopic species of C_3H_2 peaks at 60 km s^{-1} confirming the self-absorption (Madden *et al.* 1986). Other self-absorbed profiles are observed toward Sgr B2 for many molecules (Matthews and Sears 1983; Linke, Stark and Frerking 1981). Observations of the 13-carbon

Figure 3.17. $2_{12}-1_{01}$ (85 GHz) C_3H_2 profile taken toward Sgr B2 at FCRAO. The HCS^+ J=2-1 line also in the bandpass is observed at the position of the arrow. Note the dip in the C_3H_2 profile near 60 km s-1 which is due to self-absorption. Source coordinates and spectral resolution are given in Table 3.3. Antenna temperatures are corrected for atmospheric opacity by the chopper wheel method.

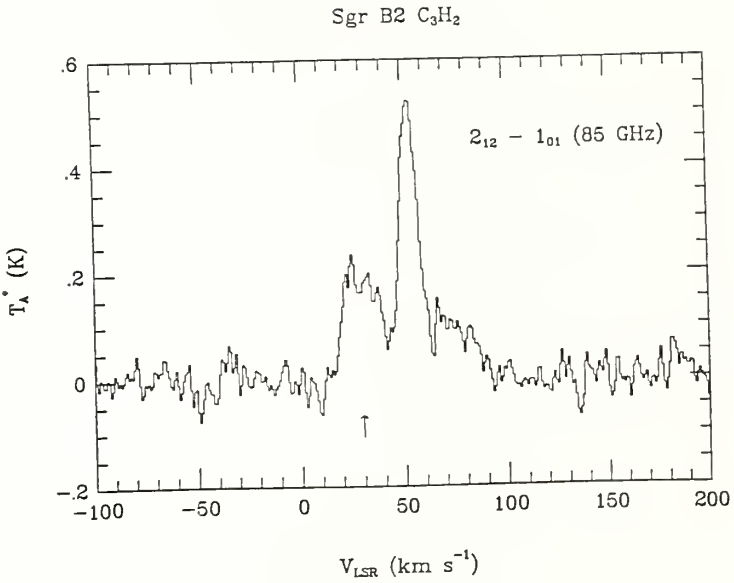
Sgr B2 C_3H_2
$2_{12} - 1_{01}$ (85 GHz)
T_A^* (K)
.6
.4
.2
0
−.2
−100
−50
0
50
100
150
200
V_{LSR} (km s^{-1})

isotopic species have been used to estimate a column density of ~ 5 $(10)^{14}$ cm^{-2} for the principal isotopic variant; for a H_2 column density of 2 $(10)^{23}$, the fractional abundance is extimated to be 3 $(10)^{-9}$ (Madden *et al.* 1986).

3.4 Discussion

This survey has demonstrated that C_3H_2 is a ubiquitous constituent of the interstellar medium. It is detected in sources possessing wide varieties of physical characteristics: in cold dense clouds, giant molecular clouds, the diffuse molecular gas component and in the envelope of a carbon star. Because of the strength of the observed transitions, at a variety of wavelengths from the cm to the mm bands, cyclopropenylidene should become a useful probe of physical conditions in the ISM; this is certainly true in the colder clouds, as we have shown for TMC-1 and L134N. We are continuing studies at 7 mm, 3 mm, and 1 mm to further assess the utility of C_3H_2 in this regard in warmer sources.

Although accurate abundance estimates for most sources will require multi- transition studies, the data obtained thus far on dark clouds indicate that C_3H_2 is one of the more abundant organic constituents of these regions. At the cyanopolyyne peak in TMC-1, $N(H_2) \sim 10^{22}$ cm^{-2}(Guélin, 1985; Irvine *et al.* 1985), giving a fractional abundance of C_3H_2 of ~ 10^{-8}, at least comparable to that of formaldehyde and HCN. For L134N the abundance is somewhat less,

consistent with the lower abundance of species like the cyanopolyynes and C_3O relative to that in TMC-1. Cox, Walmsley and Güsten (1989) have demonstrated that the abundance of C_3H_2 is related to the abundance of HC_5N in dark clouds. Those sources with greater HC_5N abundances exhibit larger C_3H_2 abundances. The dense cloud abundances are in reasonable agreement with recent calculations. On the basis of measured laboratory rates for the production of $C_3H_3^+$ via three-body association, Herbst, Adams and Smith (1984) and Adams and Smith (1987) estimate that the radiative association reaction

$$C_3H^+ + H_2 \rightarrow C_3H_3^+ + h\upsilon \qquad (3.1)$$

is relatively efficient. The precursor C_3H^+ can be produced from acetylene (C_2H_2) in a fast reaction with C^+. Dissociative recombination then yields

$$C_3H_3^+ + e \rightarrow C_3H_2 + H, \qquad (3.2)$$

$$\rightarrow C_3H + H_2. \qquad (3.3)$$

Although the isomeric form is not specified, Herbst, Adams and Smith (1984) and Millar and Nejad (1985) calculate abundances for linear C_3H_2 for a TMC-1 type cloud in the range 10^{-8} - 10^{-7}. If the branching ratio favors (3.2) over (3.3), it might explain the unexpectedly low abundance observed for C_3H, in both the linear and cyclic species (Thaddeus *et al.* 1985; Yamamoto et. al. 1987) relative

to theoretical predictions (*e.g.* Milllar and Freeman 1984). The abundances of cyclic and linear C_3H in TMC-1 have been observed to be comparable and at least an order of magnitude lower than that of C_3H_2. Cyclic C_3H in Galactic sources is indeed much less widespread than C_3H_2 but is more abundant in sources where C_3H_2 is more prevalent, especially in the dense dark clouds - rich sources of the cyanopolyynes.

CHAPTER 4

ISOTOPIC OBSERVATIONS OF C_3H_2

4.1 Detections of ^{13}C-Substituted C_3H_2 In Astronomical Sources

4.1.1 Introduction

Since the identification of the first interstellar organic ring molecule, C_3H_2, by Thaddeus, Vrtilek, and Gottlieb (1985) (see also Matthews and Irvine 1985), Galactic surveys have demonstrated the widespread nature of this molecule in giant molecular clouds, dark dust clouds, diffuse cloud regions, circumstellar envelopes, and the external galaxy Centaurus A (Madden *et al.* 1989; Seaquist and Bell 1986). Because the excitation of C_3H_2 is often far from thermal equilibrium and because strong transitions are available throughout the observable spectrum, this molecule promises to provide a valuable probe of physical conditions in the interstellar medium (Avery 1987; Matthews *et al.* 1986). Morever, the presence of C_3H_2 raises interesting chemical questions concerning the formation mechanisms of rings and the possible existence of other, more complex cyclic species.

From multitransition studies of various C_3H_2 transitions ranging from millimeter to centimeter wavelengths (Madden *et al.* 1987), it is clear that some lines are frequently saturated. Estimates of the opacity can be obtained from observations of rarer isotopic variants,

thus allowing more accurate estimates of chemical abundances. Recently, the singly substituted ^{13}C variants of C_3H_2 were identified in the laboratory by Bogey and Destombes (1986), and rotational spectra were measured. The different isotopic configurations correspond to two cases: (1) the ^{13}C lying on the axis of symmetry, and (2) the ^{13}C-substitution off the axis of symmetry, the latter case being twice as abundant as the former. We shall use the notation $^{13}CC_2H_2$ for the first case and $C_2{}^{13}CH_2$ for the second case. C_3H_2 refers to the main $^{12}C_3H_2$ isotopic species.

We have searched for both substituted species using the $2_{12} - 1_{01}$ transitions at 82 and 84 GHz and have detected $C_2{}^{13}CH_2$ in TMC-1 and Sgr B2 and tentatively in IRC +10216. We also have a consistent upper limit to $^{13}CC_2H_2$ in TMC-1. We note that Guélin (1987) reports the detection of ^{13}C-substituted C_3H_2 with the IRAM 30 m telescope, but no specific data are cited.

4.1.2 Observations

The observations of both the ^{12}C and ^{13}C isotopic species were carried out in June 1986 with the Five College Radio Astronomy Observatory (FCRAO) 14 m antenna. Values of the antenna temperatures in Figures 4.1 to 4.5 have been corrected for atmospheric opacity and losses at the ambient temperature by the standard chopper wheel method (Penzias and Burrus 1973). The spectral resolutions used are given in the figure legends. At a frequency of 85 GHz the half-power beam width of the antenna is 60" and the main beam efficiency factor,

Figure 4.1 Spectrum of the $2_{12} - 1_{01}$ transition of C_3H_2 toward the cyanopolyyne peak in TMC-1 (coordinates are given as notes to Table 4.1). The downward spikes are frequency switching artifacts. The spectral resolution is 0.18 km s^{-1}.

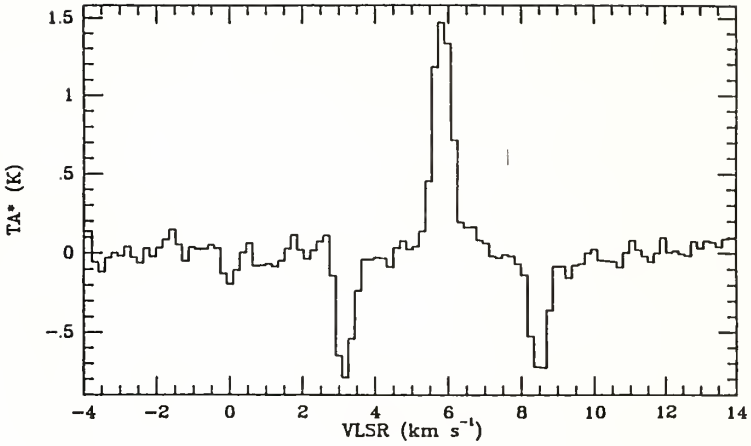
1.5
1
.5
0
-.5
TA* (K)
-4
-2
0
2
4
6
8
10
12
14
VLSR (km s^{-1})

Figure 4.2 Spectrum of the more abundant ^{13}C substituted form of C_3H_2 toward the cyanoployyne peak of TMC-1. Resolution and position are the same as in Figure 4.1.

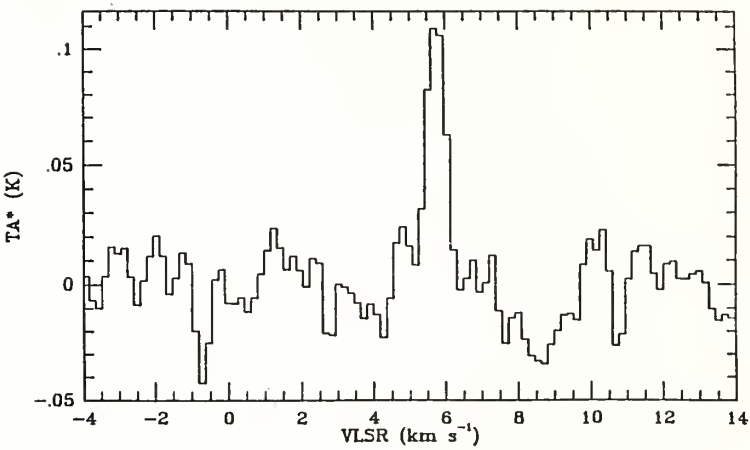
.1
.05
0
−.05
TA* (K)
−4
−2
0
2
4
6
8
10
12
14
VLSR (km s^{-1})

Figure 4.3 Spectrum of the $2_{12} - 1_{01}$ transition of C_3H_2 detected toward Sgr B2 (position given as notes to Table 4.1). The profile is self-absorbed with a dip at 60 km s^{-1}, corresponding to the velocity of the $C_2{}^{13}CH_2$ peak (Figure 4.4). The HCS^+ J = 2 - 1 rotational transition is blended into the blueshifted wing of the C_3H_2 line. The spectral resolution is 0.9 km s^{-1}.

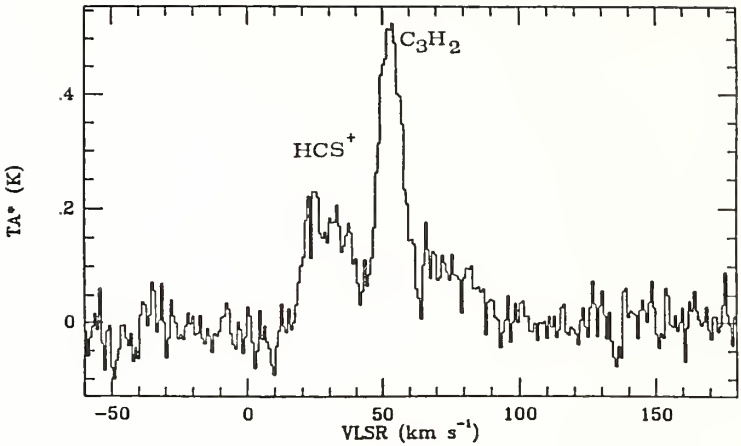
C_3H_2
HCS^+
TA* (K)
.4
.2
0
−50
0
50
100
150
VLSR (km s^{-1})

Figure 4.4 The spectrum of the $2_{12} - 1_{01}$ transition of $C^{13}C_2H_2$ toward Sgr B2. Compare with the self-absorbed profile of the main isotope in Figure 4.3. Other lines in the band are CH_3CHO (acetaldehyde) $2_{12} - 1_{01}$ A and C_2H_5CN (ethyl cyanide) $11_{0,11} - 10_{1,10}$. The spectrum has been smoothed to an effective resolution of 2 MHz.

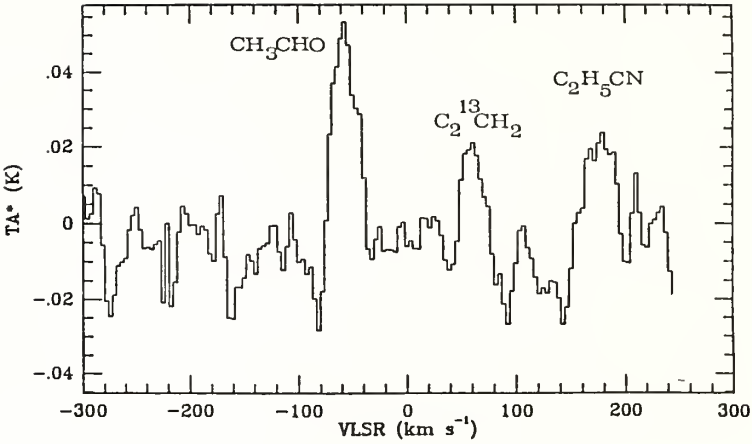
CH3CHO
C2H5CN
C2 13CH2
.04
.02
0
-.02
-.04
TA* (K)
-300
-200
-100
0
100
200
300
VLSR (km s-1)

Figure 4.5 The tentative detection of the $2_{12} - 1_{01}$ transition of the ^{13}C isotopic variant of C_3H_2 is shown at -25 km s^{-1} in IRC+10216 (coordinates are given as notes to Table 4.1). The spectrum has been smoothed to an effective resolution of 2 MHz. An unidentified doublet is observed at 84122.2 MHz (line A) and 84105.4 MHz (line B). A tentative narrow feature is seen at 84206.9 MHz (line C).

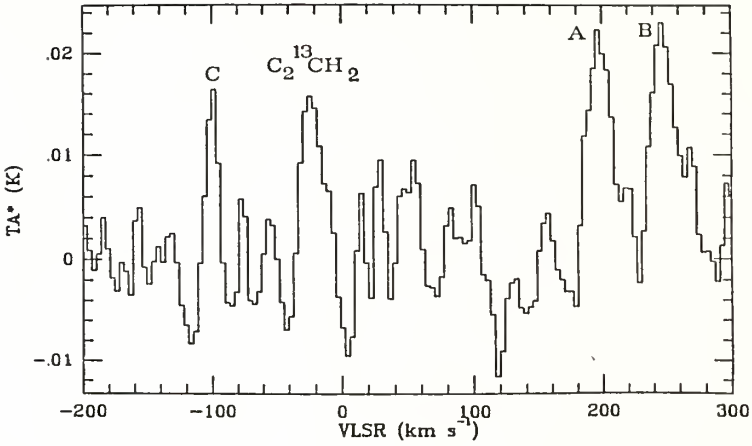
A
B
C
$C_2{}^{13}CH_2$
.02
.01
0
-.01
TA* (K)
-200
-100
0
100
200
300
VLSR (km s^{-1})

η_b, is 0.56. Frequencies are those obtained by Vrtilek, Gottlieb, and Thaddeus (1987) and Bogey and Destombes (1986).

4.1.3 Results and Discussion

The line parameters for the present observations are listed in Table 1. Due to the low intensity of the less abundant ^{13}C isotopic species, only an upper limit is reported for TMC-1.

4.1.3.1 TMC-1

From our Galactic survey of several C_3H_2 transitions, it is obvious that the dark dust cloud TMC-1 exhibits particularly strong emission and absorption of this molecule (Madden *et al.* 1987). Figure 4.1 shows the $2_{12} - 1_{01}$ transition for C_3H_2 taken toward the position of peak cyanopolyyne emission in TMC-1. Comparison with $C_2{}^{13}CH_2$ at the same position (Figure 4.2) shows similar line widths (0.69 km s^{-1}) and a ratio of integrated intensities for $C_2{}^{13}CH_2/C_3H_2$ of 0.075. For the $C_2{}^{13}CH_2$ profile, both frequency switching and position switching observing modes were used and the results have been averaged together. The relative intensities of the two species is an indication that the $C_2{}^{13}CH_2$ line is optically thin. Assuming equal excitation temperatures for the ^{12}C and ^{13}C isotopic species, we obtain T_{EX} = 5.3 K. The main isotopic species has an optical depth ranging from 5.6 to 6.8 for a $^{12}C/^{13}C$ ratio ranging from 89 (solar value) to 75 (determined by Wilson, Langer, and Goldsmith

Table 4.1

Molecular Line Parameters for the $2_{12}-1_{01}$ Transitions of ^{12}C and ^{13}C Isotopic Variants of C_3H_2[1]

Source[2]	Species	T_A^* (K)	V_{LSR} (km s^{-1})	ΔV (km s^{-1})
TMC-1	C_3H_2	1.46(0.02)	5.8(0.1)	0.69(0.08)
	$C_2{}^{13}CH_2$	0.11(0.03)	5.7(0.1)	0.68(0.08)
	$^{13}CC_2H_2$	0.04[3]		
Sgr B2[4]	C_3H_2			
	$C^{13}CH_2$	0.020(0.002)	60(3)	21(3)
IRC+10216	$C_2{}^{13}CH_2$	0.016(0.003)	-25.0(2)	22.0(3)

Notes to Table 4.1:

[1] We use the notation $^{13}CC_2H_2$ for the less abundant ^{13}C isotopic species with the ^{13}C lying on the axis of molecular symmetry, while $C_2{}^{13}CH_2$ refers to the more abundant ^{13}C species with the ^{13}C off axis. C_3H_2 refers to the main $^{12}C_3H_2$ isotopic species. Results are expressed in T_A^*, obtained by the standard chopper wheel calibration (Penzias and Burrus 1973). No correction for beam efficiency has been made. Numbers in parentheses refer to 1 σ errors.

[2] Positions (R.A., DEC; 1950) are TMC-1 ($04^h38^m38^s.8$, $25°35'45''$); Sgr B2 ($17^h44^m11^s$, $-28°22'30$); IRC+10216 ($09^h45^m14^s.8$, $13°30'40''$).

[3] Upper limit is 3 σ.

[4] Self-absorbed profile covering the velocity range of 40 - 90 km s^{-1} with a minimum at 60 km s^{-1}.

1981). The column density of C_3H_2 is ~ 1.5 x 10^{14} cm^{-2} with the following additional assumptions: (1) the levels are populated according to LTE at the derived excitation temperature, and (2) the ortho/para ratio is 3. For a hydrogen column density of 10^{22} cm^{-2} (Guélin 1985), the fractional abundance of $C_2{}^{13}CH_2$ is 1.5 x 10^{-8} at the cyanopolyyne peak in TMC-1.

Our upper limit for the less abundant $^{13}CC_2H_2$ isotopic species is consistent with this species being half as abundant as the other ^{13}C isotope, as expected.

4.1.3.2 Sagittarius B2

Observations for Sgr B2 were taken in position switching observing mode with the off position $0^{o}.5$ in azimuth from the Sgr B2 OH position. The C_3H_2 (Figure 4.3) and $C_2{}^{13}CH_2$ (Figure 4.4) observations show quite different profiles. The $C_2{}^{13}CH_2$ spectrum shows a single maximum at $V_{LSR} \approx 60$ km s^{-1} which is 21 ± 3 km s^{-1} wide. The assignment is supported by the published spectrum of the $1_{10} - 1_{01}$ line of C_3H_2, in which the most prominent feature is also at $V_{LSR} \approx 60$ km s^{-1} (Matthews and Irvine 1985). However, the main isotopic species shows a complex profile for the $2_{12} - 1_{01}$ line, with a single peak at $V_{LSR} = 53 \pm 3$ km s^{-1} which is only 10 km s^{-1} wide, a dip near 60 km s^{-1} coinciding with the $C_2{}^{13}CH_2$ peak, and an asymmetric shoulder centered at 75 km s^{-1} extending out to 90 km s^{-1} (cf. Thaddeus, Guélin, and Linke 1981). The spectrum appears to be self-absorbed, with low-excitation gas absorbing emission from a

background, more excited source. Similar, apparently self-absorbed spectra are observed toward Sgr B2 for other molecules, such as HCN (J = 1 - 0), SiO (J = 2 - 1), CO (J = 1 - 0), CH_3CN (J = 1 - 0), $H^{13}CO^+$ (J = 1 - 0), and CS (J = 1 - 0), with all of these profiles showing a pronounced minimum near 60 km s^{-1}, which is the velocity of the peak emission of other molecules such as OCS (J = 9 - 8), ^{13}CO (J = 1 - 0), and $C^{18}O$ (J = 1 - 0) (Scoville, Solomon, and Penzias 1975; Matthews and Sears 1983; Linke, Stark, and Frerking 1981).

Using the rotational temperature of 11 K derived by Vrtilek, Gottlieb, and Thaddeus (1987), a column density is determined assuming the $C_2{}^{13}CH_2$ line is optically thin, assuming a background temperature of 2.7, and assuming an ortho/para ratio of 3. We estimate a column density of C_3H_2 of 3×10^{14} to 6×10^{14} cm^{-2}, where the range of values reflects a $^{12}C/^{13}C$ ratio varying from 20 to 40 (Wannier 1980). The fractional abundance is estimated to range from 1.5×10^{-9} to 3×10^{-9} assuming the H_2 column density is 2×10^{23} cm^{-2} (Guélin 1985; Irvine, Goldsmith, and Hjalmarson 1987).

4.1.3.3 IRC +10216

Our observations of $C_2{}^{13}CH_2$ toward the carbon star IRC +10216 have produced a tentative detection at the expected V_{LSR} of -26 km s^{-1} with the typical line width of 22 ± 3 km s^{-1}. The C_3H_2 profile obtained by Johansson *et al.* (1984b) shows a double-peaked profile which is characteristic of optically thin, partially resolved emission (Olofsson *et al.* 1982). Our $C_2{}^{13}CH_2$ spectrum (Figure 4.5)

has been smoothed to an effective resolution of 2 MHz, and the low signal-to-noise ratio may obscure the expected-double peaked profile (the FCRAO beam is also ~ 50% larger than that at Onsala).

In deriving a column density of C_3H_2, we have adopted an excitation temperature of 12 K, based on Olofsson *et al.* (1982) who find that molecules with large dipole moments similar to C_3H_2 [$\mu(C_3H_2)$ = 3.3 Debye] have excitation temperatures ranging from 11 to 14 K. This procedure yields a beam-averaged column density of about 2×10^{14} cm^{-2} for a $^{12}C/^{13}C$ ratio of 20 (Olofsson *et al.* 1982). Derivation of fractional abundances in a stellar envelope is not straightforward, given the pronounced radial variations in density and temperature. We proceed by comparing the column density of C_3H_2 with that of another optically thin species taken with the same telescope at a similar frequency, to eliminate effects due to varying beam sizes. The HNC J = 1 - 0 spectrum is optically thin in IRC +10216 (M.J. Claussen, private communication), and we derive from this line a column density of 5.2×10^{13} cm^{-2} for an excitation temperature of 13 K. The fractional abundance of HNC in IRC +10216, determined by Olofsson *et al.* (1982), is 3.9×10^{-8}. Therefore, from $[C_3H_2]/[HNC]$, we derive a fractional abundance of C_3H_2 relative to H_2 of $1 - 2 \times 10^{-7}$.

The spectrum in Figure 4.5 also shows three unidentified features which include the doublet at 84122.2 and 84105.4 MHz (lines A and B, respectively), separated by $\Delta\nu$ = 17 MHz. A value of $\Delta\nu$ this small appears to rule out an assignment to ^{13}C-substituted C_4H, while the ^{13}C isotopic variant of C_3N can be eliminated on the basis of

rough estimates of its rotational constant. Interestingly enough, Lucas *et al.* (1986) report an unidentified doublet with similar linewidths and with frequencies centered around 89297 MHz (although one line is tentative and there is some uncertainty as to sideband assignment).

A tentative narrow feature (Figure 4.5, line C) appears at 84206.9 MHz but with a velocity width of 12.5 km s^{-1}, which is very uncharacteristic of IRC +10216. However, a line of similar width was recently identified as possibly masing, vibrationally excited HCN (Lucas *et al.* 1986).

4.1.3.4 Chemical Implications

The interstellar chemistry of C_3H_2 appears to be similar to that of the cyanopolyynes (HC_nN, n = 3, 5, ...) and related species, in that it is noticeably more abundant in the dark cloud TMC-1 than in the giant molecular cloud Sgr B2 (cf. Irvine, Goldsmith, and Hjalmarson 1986), and still more abundant in the envelope of the evolved carbon star IRC +10216. This analogy to the carbon chain species also holds in a comparison with recent theoretical models based on gas phase ion-molecule chemistry, which find reasonable agreement between observed abundances and the calculations at intermediate cloud ages, but predict values much too low at steady state unless the elemental abundance ratio C/O > 1 (Herbst and Leung 1986). These results suggest that the formation of C_3H_2 may be related to that of the linear carbon chains.

4.1.4 Conclusion

We have detected the more abundant ^{13}C-substituted variant of the new interstellar ring molecule, C_3H_2, in TMC-1 and Sgr B2, and we have made a tentative detection in IRC +10216. $C_2{}^{13}CH_2$ appears to be optically thin in all sources and the column density can be deduced from the spectra. An upper limit to the less abundant ^{13}C isotopic variant is consistent with it being half as abundant as the detected species. In the dark cloud TMC-1, C_3H_2 is one of the more abundant organic molecules, having a fractional abundance of $\sim 1.5 \times 10^{-8}$. The fractional abundance of C_3H_2 in IRC +10216 is estimated to be approximately an order of magnitude greater than that in TMC-1. The C_3H_2 profile in Sgr B2 is self-absorbed, and the fractional abundance is estimated from the ^{13}C data to be $\sim 2 \times 10^{-9}$, one order of magnitude less than in TMC-1.

Note added after publication of paper: The line at 84.122 GHz has been identified by Cernicharo *et al.* (1986) as C_5H $^2\Pi_{3/2}$ J=35/2→33/2. The line at 84.105 GHz is thought to be ^{13}CCH.

4.2 Deuterated C_3H_2

Intepretation of the deuteration ratio, the ratio of deuterated molecules to ordinary hydrogen-containing molecular species in interstellar clouds, is crucial to the building of chemical reaction networks and depends on chemical and physical fractionation

mechanisms. From astronomical observations of deuterated molecules, inferred [D]/[H] ratios for certain molecules can also provide limits on the electron abundance, which in turn are important in understanding the evolution of cloud dynamics and the role played by magnetic fields.

The rotational spectra of the deuterated version of C_3H_2 was measured in the laboratory (Bogey *et al.* 1987). Multiple astronomical observations of deuterated species of C_3H_2 were obtained and published by Gerin *et al.* (1987) and Bell *et al.* (1988, 1987, and 1986), while some (including Figure 4.6) were obtained for this dissertation.

The substitution of a deuterium atom for a hydrogen atom results in the loss of ortho-para symmetry. The principal inertial axis is rotated 22° and there is a resulting angle of 8°.3 between the CD bond and the a-inertial axis (cf. Figure 2.1). Consequently, an a-type dipole moment is present with μ_a = 1.3 Debye and the a-type transitions should be observable (frequencies are given in Bogey *et al.* 1987). All transitions observed to date astronomically are b-type.

Nuclear electric quadrupole hyperfine structure due to the presence of a spin equal to 1 in the deuterium atom in C_3HD is resolvable under some dark cloud conditions, since line widths can be on the order of the broadening due to thermal motions in the gas. Due to pressure broadening under terrestrial laboratory conditions, the hyperfine structure has not been resolved in the laboratory. Figure 4.6 shows the emission from 3 isotopomers for the 18 GHz 1_{10} -

Figure 4.6 Spectra of three different isotopic variants of the $1_{10} - 1_{01}$ C_3H_2 transition observed in L1498. The top profile is the more abundant version of the ^{13}C version of C_3H_2. The center spectrum is C_3HD. The resolved deuterium hyperfine structure can be seen and the expected positions and relative intensity of the hyperfine lines are indicated. The bottom profile is $^{12}C_3H_2$. The symmetric downward spikes are artifacts from the frequency switching observing technique. T_A has not been corrected for beam efficiency. Observations were carried out at the NRAO 43 m telescope. The velocity resolution is 0.07 km s^{-1}. Source coordinates are given in Table 3.2.

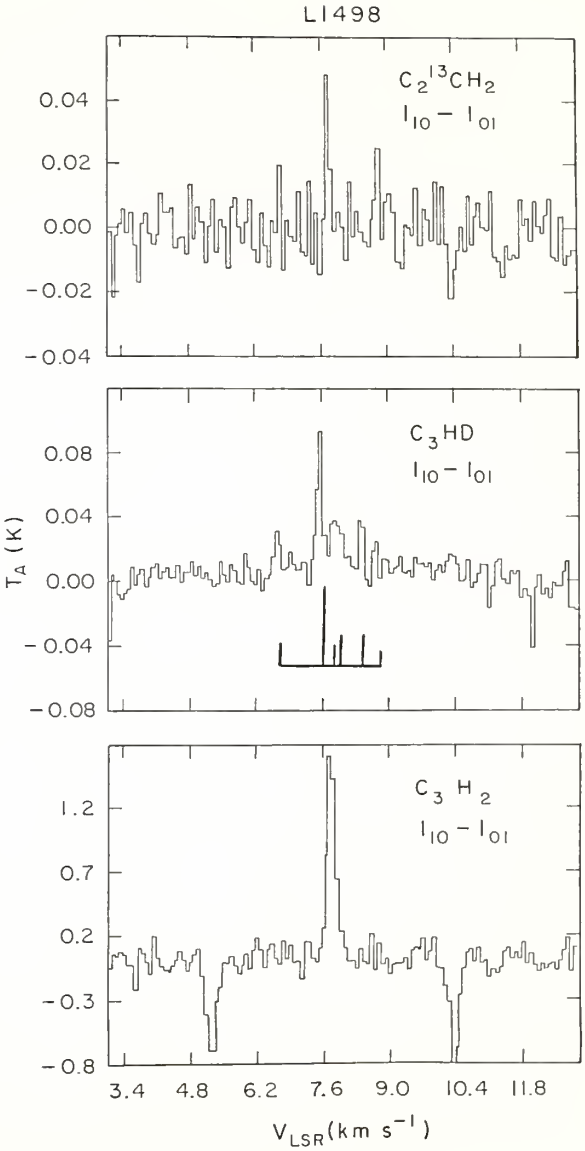
L1498
$C_2{}^{13}CH_2$
$1_{10} - 1_{01}$
0.04
0.02
0.00
-0.02
-0.04
C_3HD
$1_{10} - 1_{01}$
0.08
0.04
0.00
-0.04
-0.08
T_A (K)
C_3H_2
$1_{10} - 1_{01}$
1.2
0.7
0.2
-0.3
-0.8
3.4
4.8
6.2
7.6
9.0
10.4
11.8
V_{LSR}(km s^{-1})

1_{01} C_3H_2 transition observed toward L1498: $C_2{}^{13}CH_2$ (having the ^{13}C substitution off the axis of symmetry - the more abundant case), C_3HD, and the main isotope, C_3H_2. The 6 hyperfine components in C_3HD can be seen with the relative hyperfine intensity scale indicated, and line widths are 0.24 km s^{-1}. The hyperfine structure was also resolved in TMC-1, the dark cloud exhibiting the largest C_3H_2 abundance (Bell *et al.* 1988).

C_3HD abundances were estimated for 12 dark cloud sources and deuteration ratios were determined to range from 0.05 to 0.15 (Gerin *et al.* 1987 and Bell *et al.* 1988). These are among the highest ratios yet observed in the interstelar medium with maximum values as high as the maximum observed $[NH_2D]/[NH_3]$ ratio (Irvine and Knacke 1988).

The cosmic abundance of deuterium relative to hydrogen is 10^{-5}, yet many deuterated molecules have been observed in the interstellar medium (Wooten 1987). Enhancement of many deuterated species is thought to occur via the H_2D^+ ion, which is formed in the following reaction:

$$H_3^+ + HD \rightleftarrows H_2D^+ + H_2. \qquad (4.1)$$

At low temperatures this reaction will proceed more easily in the forward direction, resulting in an enhanced H_2D^+ abundance which then is responsible for propagating the fractionation through reactions with other molecules.

To explain the high C_3HD deuteration ratios observed, reaction pathways more efficient than the simple deuteration scheme,

$$C_3H_2 + H_2D^+ \rightarrow C_3H_2D^+ + H_2 \qquad (4.2)$$

$$C_3H_2D^+ + e^- \rightarrow C_3HD + H \qquad (4.3)$$

are necessary (Bell *et al.* 1986). C_3HD can also be formed in a path parallel to that by which C_3H_2 is formed (equations 2.2, 2.3, and 2.4):

$$C_2HD + C^+ \rightarrow C_3D^+ + H \qquad (4.4)$$

$$C_3D^+ + H_2 \rightarrow C_3H_2D^+ + h\nu \qquad (4.5)$$

$$C_3H_2D^+ + e^- \rightarrow C_3HD + H \qquad (4.6)$$

This reaction series can result in a high deuteration ratio if the Gellene-Porter mechanism (1984; cf. Bell *et al.* 1988) is evoked, which results in a preferential loss of H over D in the dissociative recombination reactions 4.6 and 4.3. Otherwise, if *equal* probability is assumed, the predicted $[C_3HD]/[C_3H_2]$ is underestimated. The expected C_3H_2 deuteration ratio, when the Gellene-Porter enhancement is assumed, is given by Bell *et al.* (1988):

$$[C_3HD]/[C_3H_2] \leq \frac{1.0 \times 10^{-13}}{(10^{-6}\ [e^-] + 3.6 \times 10^{-13})} . \qquad (4.7)$$

To achieve deuteration ratios as high as 15% as seen in many of the sources, the electron abundance relative to molecular hydrogen, $[e^-]$, is required to be $\sim 3 \times 10^{-7}$, which is within the value allowed by theoretical models (Millar and Freeman, 1984; Dalgarno and Lepp 1984).

However, Millar, Bennett and Herbst (1989) have cast doubt on the applicability of the Gellene-Porter mechanism to enhance deuterated species in the case of reactions involving the recombination of ions and electrons. They adopt an equal probability for releasing H or D in reaction 4.6 in their recent time-dependent gas-phase chemistry model of deuterium fractionation. This model satisfactorily accounts for the deuteration ratios of 9 molecular species in TMC-1. A notable discrepancy, however, still rests in the case of C_3H_2 where the theoretical $[C_3HD]/[C_3H_2]$ ratio is low by a factor of about 10 compared to observations. If the Gellene-Porter effect were evoked to increase the $[C_3HD]/[C_3H_2]$ ratio, Millar, Bennett and Herbst (1989) point out that a direct effect would be an enhancement in $[C_2D]/[C_2H]$, contrary to observations (Combes *et al.* 1985). Moreover, recent observations demonstrate that C_4D is one of the lowest fractionated species in TMC-1, having a ratio of $[C_4D]/[C_4H] \sim 0.004$ (Turner, 1989). Since C_3HD is a precursor of C_4D, enhancing $[C_3HD]/[C_3H_2]$ might lead to a large ratio of $[C_4D]/[C_4H]$, in contrast to observations. The anomalously high deuteration ratio of C_3H_2 in dark clouds remains an unresolved question in the present gas-phase chemistry schemes.

CHAPTER 5

MODEL CALCULATIONS

5.1 Basic Spectral Line Interpretation

The observed radiation from a spectral line source should, in principle, allow the observer to extract information on the physical properties of the source. Properties which can affect the line radiation include the density, the abundance of the observed molecule producing the spectral line, the continuum radiation field, and the kinetic temperature. Beginning with the fundamentals of radiative transfer theory, this chapter outlines those aspects essential for deriving molecular cloud physical parameters such as molecular hydrogen density and molecular abundances from spectral lines.

Variation in the observed radiation propagating through a medium which absorbs and emits radiation of frequency ν through the path length dl is given by the the one-dimensional time-independent basic transfer equation:

$$\frac{dI_\nu}{dl} = -\kappa_\nu I_\nu + \varepsilon_\nu \tag{5.1}$$

where I_ν, the specific intensity, is the amount of energy per unit frequency interval centered at the frequency ν, passing through a unit area perpendicular to the direction of propagation per unit time

per unit solid angle. The volume emission coefficient, ε_ν, accounts for spontaneous transitions from the upper energy level i to the lower level j and can be expressed as

$$\varepsilon_\nu = n_i A_{ij} (h\nu_{ij}/4\pi) \varphi(\nu) \tag{5.2}$$

and $\varphi(\nu)$ is the normalized line profile function; n_i is the population in the ith level and A_{ij} is the Einstein A coefficient for spontaneous decay from the ith level to the jth level. In the absence of scattering, the volume absorption coefficient, κ_ν, can be written as:

$$\kappa_\nu = h\nu_{ij}/4\pi \ (n_j B_{ji} - n_i B_{ij}) \ \varphi(\nu) \tag{5.3}$$

where B_{ij} and B_{ji} are the Einstein B coefficients for stimulated emission and absorption between levels i and j.

Since the variation in optical depth, $d\tau_\nu$, is defined as:

$$d\tau_\nu = \kappa_\nu \, dl \ , \tag{5.4}$$

we can express the transfer equation as

$$\frac{dI_\nu}{d\tau_\nu} = -I_\nu + S_\nu \tag{5.5}$$

where S is the source function, defined as $\varepsilon_\nu/\kappa_\nu$, and determines the amount of locally produced emission contributing to I_ν.

The excitation temperature is defined by the Boltzmann law in terms of the relative populations of levels i and j for the transition $i \rightarrow j$:

$$n_i/n_j = (g_i/g_j)\ \exp[(E_j-E_i)/kT_{EX}] \qquad (5.6)$$

where n_i and n_j are the number of molecules per unit volume with energy E_i and E_j, respectively, and g_i is the degeneracy of the ith level (i.e. the number of quantum states with energy E_i), which, apart from the effects of nuclear statistics, equals $2(J_i + 1)$ where J_i is the rotational quantum number of the ith level. S_ν can then be derived from the definitions of ε_ν and κ_ν to be the Planck function at the excitation temperature of the transition (T_{EX}):

$$S_\nu = B_\nu(T_{EX}) = (2h\nu_{ij}^3/c^2)\ (1/(\exp(h\nu_{ij}/kT_{EX}) - 1)) \qquad (5.7)$$

If we integrate the transfer equation along the line of sight, a solution for the emerging specific intensity for a plane parallel slab is of the form:

$$I_\nu = I_{BG}\exp(-\tau_{L\nu}) + \int_0^{\tau_{L\nu}} \exp(-\tau'_\nu)\ S_\nu(\tau'_\nu)\ d\tau'_\nu\ , \qquad (5.8)$$

where $\tau_{L\nu}$ is the total optical depth over the distance L (as a function of frequency) and τ_ν' in this case is integrated from the front edge of the cloud into the cloud interior. The solution can be interpreted as the sum of two terms: the background intensity I_{BG}

incident on the cloud (which in the cases lacking continuum background is the 2.7 K cosmic microwave background) diminished by absorption through the cloud ($e^{-\tau_{L\nu}}$) plus the integrated source function within the cloud attenuated by absorption through the cloud. The difficulty in the solution of the radiative transfer problem, in effect, reduces to determining the source function as a function of position and frequency. In the simple case where the source function is constant over τ_ν (i.e. constant with position), it can be removed from the integral in equation 5.8 and expressed as a Planck function evaluated at T_{EX}. Following integration, equation 5.8 then reduces to

$$I_\nu = I_{BG}\exp(-\tau_\nu) + B_\nu(T_{EX})\ [1 - \exp(\tau_{L\nu})]. \qquad (5.9)$$

The emerging intensity therefore depends on the total optical depth $\tau_{L\nu}$, and the excitation temperature along the line of sight. These quantities are determined by the cloud properties such as density, abundance, and kinetic temperature. Usually when observing a spectral line, the quantity of interest is the intensity of a spectral line measured with respect to the neighboring continuum. The background contribution, measured outside the line, is subtracted from the total contribution to the observed line intensity, and we have

$$\Delta I_\nu = (B_\nu(T_{EX}) - I_{BG})\ [1 - \exp(-\tau_\nu)]. \qquad (5.10)$$

It is customary to define a brightness temperature of the line, T_B, such that T_B is the temperature for which the Planck function (equation 5.7), expressed in the limit where $h\nu_{ij} << kT$, would result in the observed intensity, ΔI_ν:

$$\frac{2kT_B\nu_{ij}^2}{c^2} = \Delta I_\nu \ . \tag{5.11}$$

The resultant brightness temperature can then be expressed as:

$$T_B(\nu) = \frac{h\nu}{k}\left(\frac{1}{\exp(h\nu/kT_{Ex}) - 1} - \frac{1}{(\exp(h\nu/kT_{BG}) - 1}\right)[1 - \exp(-\tau_\nu)] \tag{5.12}$$

This expression allows us, in principle, to determine source properties such as optical depth and T_{EX} from the observed brightness temperature, T_B. From these, one can proceed to deduce some simple properties of a molecular cloud from observations of C_3H_2 such as the column density of the molecule (N), i.e. the number of molecules observed along the line of sight of the telescope, and the H_2 volume density $n(H_2)$. This requires determining T_{EX}, which in turn is a function of the level populations.

5.2 Determining the Level Populations

To determine the abundance of a molecule, one should in principle determine the population distribution of that molecule in

all possible energy levels. Since we only observe a finite number of transitions, we must make assumptions about the distribution of the populations in the other levels in order to deduce the total abundance of the molecule. Assuming conditions of thermal equilibrium, where T_{EX} is the same for all levels (defined in this case as rotation temperature T_{ROT}), the levels are filled according to a Boltzmann distribution governed by T_{ROT}. A partition function is then defined for asymmetric molecules, such as C_3H_2 (Townes and Schawlow 1975), by

$$Q = \sum_i g_i g_I \exp(-E_i/kT_{ROT}) \tag{5.13}$$

where g_I is the reduced nuclear spin statistical weight factor. This factor is equal to $(I+1)(2I+1)/(2I+1)^2 = 3/4$ for ortho C_3H_2, and is equal to $I(2I+1)/(2I+1)^2 = 1/4$ for the para species (Townes and Schawlow 1975). The fractional population in level i (f_i) is then expressed as:

$$f_i = \frac{g_i g_I \exp(E_i/kT_{ROT})}{Q} . \tag{5.14}$$

The population of each rotational level is determined by the competition between the collisional and radiative processes which are attempting to populate and depopulate the levels. The rate of change of population in the jth level expressed as the summation from all

collisional and radiative contributions from the ith levels to the jth level under statistical equilibrium is:

$$\frac{dn_j}{dt} = \sum_i (n_i A_{ij} + n_i B_{ij} \bar{J} - n_j B_{ji} \bar{J} + n_i C_{ij} - n_j C_{ji}) = 0 \qquad (5.15)$$

where the first 3 terms are the contributions resulting from radiative processes and the last 2 terms are due to collisional processes. $\bar{J}$ is the average intensity integrated over the line profile and averaged over all directions:

$$\bar{J} = \frac{1}{4\pi} \int_0^{\infty} \int^{4\pi} I_\nu \, \varphi(\nu) \, d\Omega \, d\nu \, . \qquad (5.16)$$

The A coefficient is expressed as

$$A_{ij} = \frac{64\pi^4 \nu_{ij}^3 \quad \mu_0^2 \, S_{ij}}{3hc^3 \quad 2J_i + 1} \qquad (5.17)$$

where S_{ij} is the transition strength of the $i \rightarrow j$ transition and μ_0 is the permanent electric dipole moment. For C_3H_2, μ_0 is 3.4 Debye (Lee, Bunge and Schaefer 1985; Kanata, Yammamoto, and Saito 1987). The stimulated and spontaneous coefficients are related by:

$$A_{ij} = (2h\nu_{ij}^3/c^2) \, B_{ij} \quad \text{and} \quad B_{ji} = (g_i/g_j) \, B_{ij}. \qquad (5.18)$$

C_{ij} and C_{ji} are the downward and upward collisional rates, which depend on the gas velocity (governed by the kinetic temperature, T_{Kin}) and the density of the colliders, mostly H_2. A fundamental problem remains: that of determining the intensity in equation (5.15). Through stimulated absorption and stimulated emission, the radiation affects the level populations locally, yet $\bar{J}$ is also the product of many contributions from other locations in the source. If the transitions are optically thin, the emitted photons will easily escape from the cloud and the intensity is given by the cosmic background radiation and approximated by the Planck function at the microwave background temperature T_{BG} (T_{BG} = 2.7 K when no continuum is produced by dust and no non-thermal processes contribute). However, if the transitions are optically thick, photons emitted in one part of the cloud will be absorbed elsewhere and the successive interactions will contribute to the radiation intensity, an effect called radiative trapping. While we are attempting to solve a *local* population problem, we can have many parts of the cloud radiatively coupled. To determine the mean radiation intensity for optically thick cases, we must incorporate radiative transfer.

To actually obtain a general solution to the coupled equations describing both the statistical equilibrium and radiative transfer requires a prohibitive amount of computing time except in cases of very simple geometry.

5.3 Large Velocity Gradient Method

To simplify the radiative transfer problem, a method was developed by Sobolev (1960) and utilized by Castor (1970), Lucy (1971) and others, called the Sobolev approximation or the Large Velocity Gradient (LVG) method. Both names are used interchangeably in this paper. Goldreich and Kwan (1974) refined this method for application to spectral lines in molecular clouds. The Sobolev technique assumes that a large velocity gradient (dv/dr) exists throughout a spherically collapsing cloud with the condition that the cloud thermal velocity (v_{th}) is small compared to the collapse velocity. When the velocity gradient is large, emitted photons can escape from the medium in one direct flight since no absorption or emission is possible beyond the local medium; photons will not be absorbed by molecules Doppler shifted from the rest frequency of the emission. By using the Sobolev approximation, we are able to make the necessary corrections for the radiative trapping effects of C_3H_2, for which the stronger transitions are thought to be optically thick.

The essential question to determine is: how far can a photon travel before being absorbed? At any particular point in the cloud, the fate of each photon is determined simply by its probability of escape, β, and the local source function. Hence, we are justified in removing the source function from the integral in (5.8). Any photon surviving beyond the distance, $L = v_{th}/(dv/dr)$ will escape from the medium. The transfer equation can be rewritten (de Jong, Chu and Dalgarno 1975) as:

$$\bar{J}_\nu = [1 - \beta(r)]\ S_\nu(T_{EX}, r) + \beta(r)\ B_\nu(T_{BG})\ . \qquad (5.19)$$

Here β is the probability that a photon emitted in a particular transition at the radial distance r will escape from the cloud. An expression for the escape probability is given by Goldreich and Kwan (1974) for the special case of a collapsing sphere of uniform density and velocity proportional to radial distance (r):

$$\beta(r) = [1-\exp(-\tau)]/\tau\ , \qquad (5.20)$$

where τ is the peak optical depth of the transition. For the limiting case where all photons escape from the medium (τ is very small), $\beta = 1$ and the average intensity (equation 5.19) reduces to the blackbody radiation field at the 2.7 K background temperature; in the other limit where no photons escape (τ is very large), $\beta \to 0$ and the mean intensity reduces simply to the local source function $S_\nu(T_{EX}, r)$. From the definition of τ (equation 5.4):

$$d\tau_{ij} = \frac{A_{ij} c^2 g_i n_j}{8\pi\nu_{ij}^2 g_j} [1 - \exp(-h\nu/kT_{EX})]\ \varphi(\nu')dl, \qquad (5.21)$$

where ν', the frequency of the photon in the local frame of the emitting molecules equals $[\nu - (v/c)\ \nu_{ij}]$, ν is the frequency of the photon as viewed from the observers frame, and ν_{ij} is the rest frequency of the emitted photon. The optical depth can now be

expressed as:

$$\tau = \frac{A_{ij} c^2 g_i n_j}{8\pi\nu_{ij}^2 g_j} [1 - \exp(-h\nu/kT_{EX})] \int_0^L \varphi[\nu - (v/c)\nu_{ij}]dl. \quad (5.22)$$

Contribution to the integral of τ_ν is only from within the small region around the position where $\nu' = 0$ (i.e. $(v/c)\ \nu_{ij} = \nu$); thus,

$$d\nu = \frac{\nu_{ij}}{c} \frac{dv}{dr} dl. \quad (5.23)$$

Substituting the above expression into equation 5.22, and making the assumption that properties such as T_{EX}, n_i, dv/dr are constant in the region, τ_ν can be expressed as:

$$\tau_\nu = \frac{A_{ij}\ c^3 g_i}{8\pi\nu_{ij}^3 g_j}\ f_i\ (1 - \exp(-h\nu_{ij}/kT_{EX}))\ \frac{X}{(dv/dr)}\ n(H_2). \quad (5.24)$$

The velocity gradient in the cloud is dv/dr and is frequently approximated by $(\Delta v)/L$, the velocity width of the line divided by the source size. The molecular hydrogen volume density is $n(H_2)$; f_i is the fraction of the total population existing in the ith level, and X is the fractional abundance of the molecule with respect to molecular hydrogen. The total column density of molecules, N, is equal to (X) x $n(H_2)$ x L.

The LVG program solves first the equation of statistical equilibrium, and equations 5.6, 5.7, 5.19, 5.20 and 5.24 are used to express $\bar{J}_\nu$ in terms of the level populations, resulting in a system of non-linear equations which can then be solved for the population in each of the levels. For each transition, the values of T_{EX} and τ are calculated, and finally the true brightness temperature (T_B) is determined from equation 5.12.

The validity of the Sobolev approximation is contingent upon the condition that the whole cloud under consideration is undergoing a collapse with a systematic large velocity gradient. Observational evidence for this kind of collapse in molecular clouds does not exist. The limitations intensify in the case of quiescent dark clouds, which have narrow linewidths, generally on the order of 0.5 km s^{-1}. Much of the observed velocity widths from such narrow lines is attributed to thermal motions, especially in the case of L1498 (section 6.3) where linewidths are only 0.25 km s^{-1}. Thus different parts of the cloud are *not* truly radiatively decoupled in these cases.

5.3.1 Uniform Density Model for C_3H_2: Methodology

Our uniform density LVG model is that used by Avery and Green (1989) and developed by Goldreich and Kwan (1974) and de Jong, Chu, and Dalgarno (1975). Collisional excitation rates for C_3H_2 calculated using the coupled states approximation by Avery and Green (1989) were used for a cloud having a kinetic temperature, T_{KIN}, of

10 K. As the rates were calculated using helium atoms as the colliders, a factor of $\sqrt{2}$ was incorporated in the cross section calculations to account for larger reduced mass when assuming molecular hydrogen colliders instead of helium. The model has been constructed assuming a uniform density, spherically collapsing cloud, and employs the formalism described in section 5.4. Since the ortho and para symmetry species of C_3H_2 can be treated as 2 distinct species (see section 2.1), the LVG solution was applied separately for the lowest 17 para levels ranging up to 43 K above the ground state and 24 ortho levels up to 65 K above the ground state. An ortho:para abundance ratio (O:P) was assumed to be the ratio of the statistical weights, 3:1. We subsequently determined an ortho to para ratio of C_3H_2 in dark clouds independently by solving separately for both ortho and para abundances (section 6.6).

In order to quantitatively evaluate the goodness of fit for the models applied to the observed sources, we determined the value of chi-squared, χ^2, which is a quantity characterizing the discrepancy between the model results and the observed data, weighted by the individual root mean square (rms) uncertainty in each measurement:

$$\chi^2 = \sum_i (T_B - T_M)_i^{\,2} / \sigma_i^{\,2} , \qquad (5.25)$$

where T_B and T_M are the observed and model brightness temperatures of the individual transitions and σ^2 is the variance of the individual measurement. The variance is taken to be the sum in quadrature of the 1 sigma (1σ) rms noise of the observations and a calibration

uncertainty assumed to be 10% of the brightness temperature for all of the observations except those carried out at 46, 51, and 122 GHz. For these 3 observations a more conservative calibration error of 20% of the intensity was adopted, since these lines are more severely effected by O_2 atmospheric absorption. As a result, the uncertainty in the weaker lines is dominated by the noise rms while the error in the stronger lines is dominated by the calibration uncertainty. The numerator in equation 5.25 describes the spread of the observations with respect to the model, while the denominator is a measure of the expected spread.

In order to compare results of different models or results for different sources, a more useful parameter to calculate is the *reduced* chi-squared:

$$\tilde{\chi}^2 = \chi^2 / \text{nfree} \tag{5.26}$$

where nfree is the number of degrees of freedom in the calculation: the difference between the number of transitions in the model and the number of free parameters in the calculation. For the LVG uniform density model, the number of free parameters is 2: the volume density of molecular hydrogen, $n(H_2)$ and the abundance parameter X/(dv/dr).

In reality, the test to determine the lowest $\tilde{\chi}^2$ provides no simple answer to the question of whether the model fits the data (or vice versa). If the deviations of the model results from the observations (or vice versa) correspond to a normal distribution as can be expected, we would obtain a small $\tilde{\chi}^2$ value. When the

dispersion of the observed values from the results is approximately equal to the expected spread of the observations, we can expect $\tilde{\chi}^2$ to be close to 1. If $\tilde{\chi}^2$ is large, the model being used to describe the observations is probably not a satisfactory one. If $\tilde{\chi}^2$ is much less than 1, this is an unlikely situation and it is possible that the uncertainties in the observations are overestimated.

A procedure was developed to search the entire space of $n(H_2)$ - X/(dv/dr) for the best fit of the data as designated by the lowest value of $\tilde{\chi}^2$. Employing the idea proposed by Bevington (1969), a search is carried out first varying $n(H_2)$ by small increments keeping X/(dv/dr) constant and determining $\tilde{\chi}^2$ for each successive step, proceeding in the direction of *decreasing* $\tilde{\chi}^2$. When $\tilde{\chi}^2$ begins to increase, the procedure repeats the process in the X/(dv/dr) dimension until a minimum of $\tilde{\chi}^2$ in that direction is reached, etc. After the solution converges, the final 3 points are fit to a parabola to determine the final solution to the fit parameters. The error associated with the fit is based on these final 3 points which, in effect, describe the gradient around the minimum value. However since X/(dv/dr) and $n(H_2)$ are not completely independent parameters (X depends on molecular hydrogen density), the calculated errors are underestimated as the correlation is not taken into account. As increments are made throughout parameter space $\tilde{\chi}^2$ is recalculated. The minumum $\tilde{\chi}^2$ determined "by eye" from the contour plots of $\tilde{\chi}^2$ as a function of $n(H_2)$ and X/(dv/dr) (Chapter 6) may not necessarily be identical to what is determined more accurately from the search routine. For every increment in each of the independent parameters,

the value of chi-squared is recalculated directly following interpolation of the model brightness temperatures. $\tilde{\chi}^2$ is *not* simply interpolated from the contour plots.

5.3.2 Uniform Density LVG Results: General Interpretation

We have observed a variety of C_3H_2 transitions for use in the model calculations. Table 5.1 describes the transitions involved in this study and various properties associated with them.

It is instructive to illustrate the LVG results through some examples and to note which regions of parameter space can typify physical conditions in molecular clouds. Avery and Green (1989) present calculated ratios of numerous pairs of C_3H_2 transitions and interpret their behavior as functions of $n(H_2)$ and $X/(dv/dr)$.

LVG results are shown, for example, in Figure 5.1 for the 2_{20}-2_{11} 21 GHz para transition, where the constant brightness temperature contours are plotted as functions of $n(H_2)$and $X/(dv/dr)$. Plotted on the axes are the log values of the 2 parameters we are solving for in the LVG calculation: $X/(dv/dr)$ and $n(H_2)$. Recall that X is the fractional abundance of C_3H_2 relative to H_2. The column density of C_3H_2 can be estimated by:

$$\frac{N(C_3H_2)}{\Delta V} = X/(dv/dr)(\mathrm{pc\ s\ km^{-1}}) \times n(H_2)(\mathrm{cm^{-3}}) \times 3\times10^{18}(\mathrm{cm/pc}) \qquad (5.27)$$

TABLE 5.1

Parameters of Observed C_3H_2 Transitions

Transition	Frequency[1] (GHz)	E/k (K) [2]	A (s^{-1})
ortho:			
$1_{10}-1_{01}$	18.343	0.9	4.2×10^{-7}
$2_{12}-1_{01}$	85.338	4.1	2.6×10^{-5}
$2_{21}-1_{10}$	122.023	6.7	7.5×10^{-5}
$3_{12}-3_{03}$	82.966	13.7	1.1×10^{-5}
$3_{30}-2_{21}$	216.278	17.1	2.1×10^{-4}
para:			
$1_{11}-0_{00}$	51.841	2.5	6.4×10^{-6}
$2_{02}-1_{11}$	82.093	6.4	2.1×10^{-5}
$2_{11}-2_{02}$	46.755	8.7	2.9×10^{-6}
$2_{20}-2_{11}$	21.587	9.7	6.3×10^{-7}
$3_{22}-3_{13}$	84.727	16.1	1.1×10^{-5}

Notes for Table 5.1:

[1] Frequencies are from Thaddeus, Vrtilek and Gottlieb (1985)

[2] E/k is the energy (in temperature units) of the upper level above the ground ortho or ground para states.

Figure 5.1 Constant brightness temperature contours for the $2_{20} - 2_{11}$ 21 GHz transition from LVG calculations. Results are for a uniform density source with a kinetic temperature of 10 K. Contour levels range from -1.2 to 7.0 K in steps of 0.82 K. Levels -1.2, 2.1, and 6.2 are represented by dashed lines of increasing thickness.

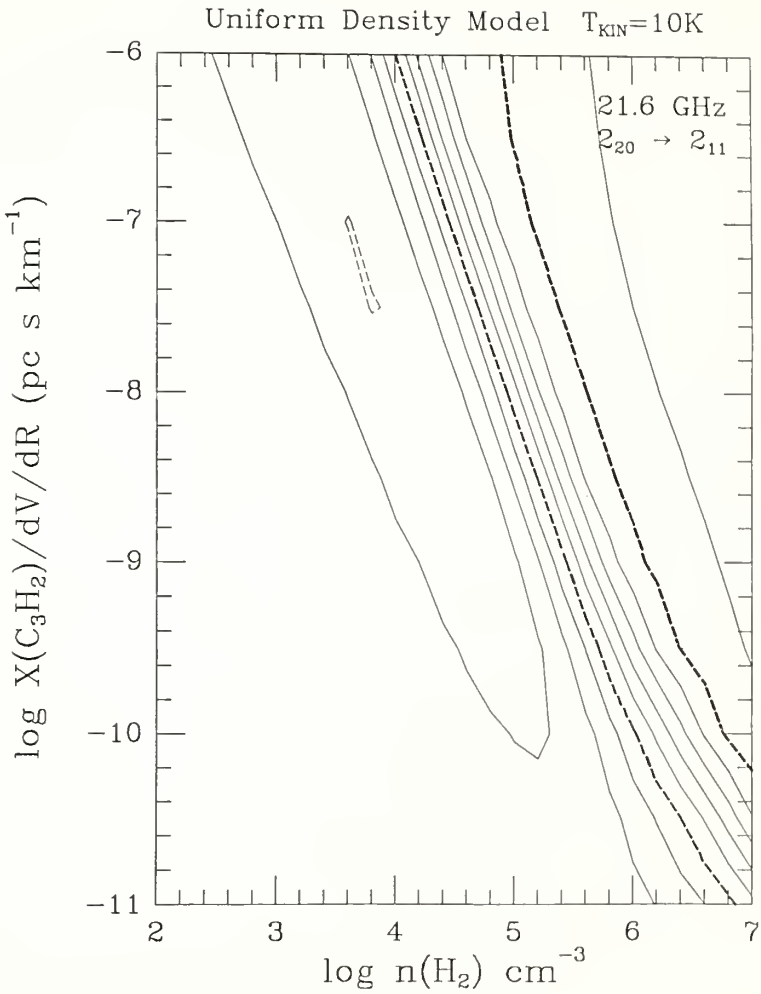
Uniform Density Model T_{KIN}=10K
21.6 GHz
$2_{20} \rightarrow 2_{11}$
log $X(C_3H_2)/dV/dR$ (pc s km^{-1})
log $n(H_2)$ cm^{-3}
−6
−7
−8
−9
−10
−11
2
3
4
5
6
7

when we assume, as is commonly done, that dv/dr can be estimated from the extent of the source, (L), and the line velocity width, Δv. It is only necessary, therefore, to estimate the velocity width of the line in order to determine the column density.

The behavior of the 21 GHz C_3H_2 line is an interesting feature of this molecule, giving it potentially useful diagnostic properties. There is a wide regime in $n(H_2)$, X/(dv/dr) space, including conditions which typify dark clouds, diffuse clouds and some even denser molecular clouds ($n(H_2) > 10^5$ cm^{-3}) where the 21 GHz transition is predicted to appear in absorption against the microwave background. At higher densities, the "refrigeration effect" of this line is quenched, and the line is predicted to be in emission. Figure 5.2 shows contours of calculated optical depths and excitation temperatures for the 21 GHz transition. The contour for T_{EX} = 2.7 K separates the emission and absorption regions. The thermalization plateau where $T_{EX} = T_{KIN}$ lies in a region where $n(H_2) \geq 1.6\times10^6 cm^{-3}$ and $X/(dv/dr) > 10^{-9}$ pc s km^{-1}. As also seen in Figure 5.1, the maximum absorption corresponds to a $T_B = -1.2$ K and, as the results from Chapter 6 show, this low absorption value presents a difficulty for the models to match observations quantitatively. This transition has indeed been reported in absorption in molecular clouds associated with HII regions and in dark clouds. Cox, Güsten, and Henkel (1987) detect this transition in emission in the planetary nebula, NGC7027.

Figures 5.3 and 5.4 show the behavior of the 18 GHz $1_{10} - 1_{01}$ optical depth, brightness temperature, and excitation temperature. The effect of radiative trapping can be observed in this plot (and in

Figure 5.2 Constant T_{Ex} and tau contours from LVG calculations for the 2_{20} - 2_{11} 21 GHz transition. Results are for a uniform density source with a kinetic temperature of 10 K. T_{EX} contours (dashed lines) range from 1.4 K to 10.0 K in steps of 0.11 K. Tau contours (solid lines) range from 0.1 to 10.0 in steps of 0.10 K. The $n(H_2)$, X/(dv/dr) region to the left of the contour for T_{Ex} = 2.7 K (bold dash-dot line) is where the line is predicted to be in absorption. To the right of this contour, the 21 GHz line is predicted to be in emission.

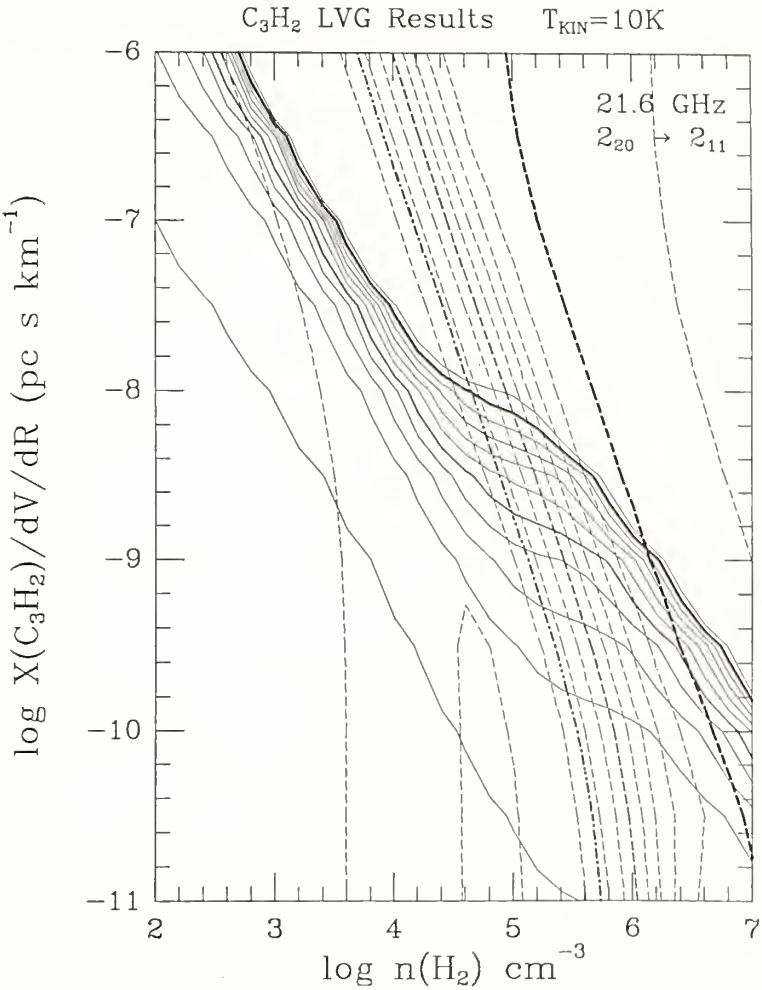
C_3H_2 LVG Results T_{KIN}=10K
21.6 GHz
$2_{20} \rightarrow 2_{11}$
log $X(C_3H_2)/dV/dR$ (pc s km^{-1})
log $n(H_2)$ cm^{-3}
−6
−7
−8
−9
−10
−11
2
3
4
5
6
7

Figure 5.3 Constant brightness temperature contours from LVG calculations for the the $1_{10} - 1_{01}$ 18 GHz transition. Results are for a uniform density source with a kinetic temperature of 10 K. Contour levels range from 0.0 to 20.0 K in steps of 2.0 K. Levels 0, 8, and 18 are represented by dashed lines of increasing thickness.

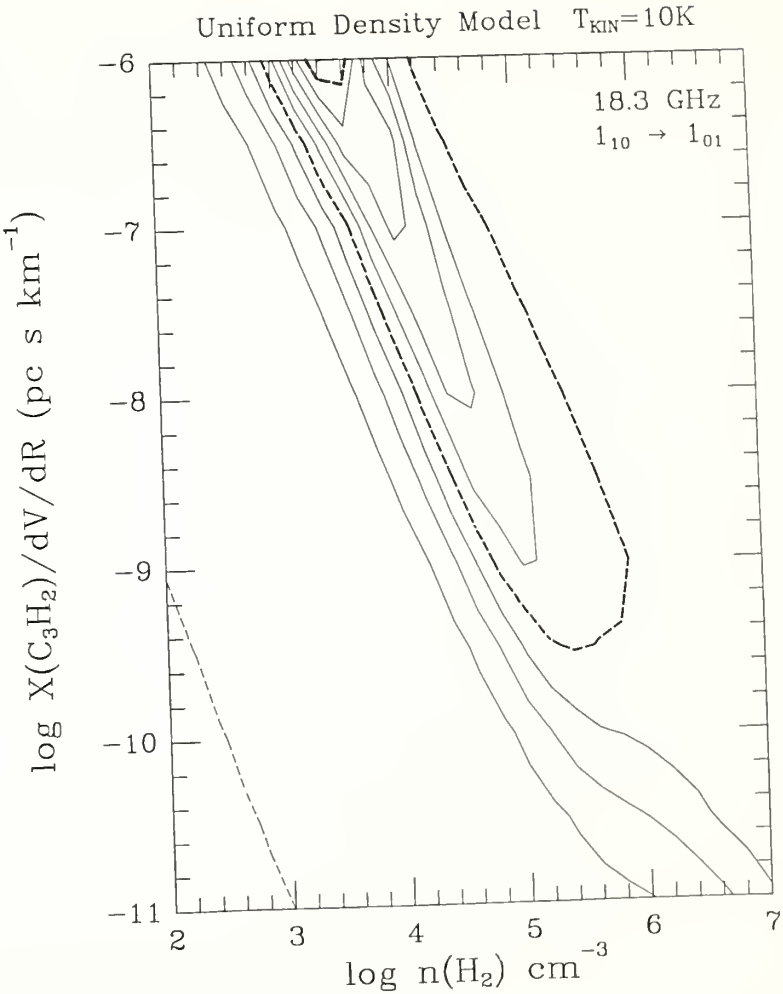
Uniform Density Model T_{KIN}=10K
18.3 GHz
$1_{10} \rightarrow 1_{01}$
log $X(C_3H_2)/dV/dR$ (pc s km^{-1})
log $n(H_2)$ cm^{-3}
−6
−7
−8
−9
−10
−11
2
3
4
5
6
7

Figure 5.4 Constant T_{Ex} and tau contours from LVG calculations for the $1_{10} - 1_{01}$ 18 GHz transition. Results are for a uniform density source with a kinetic temperature of 10 K. T_{EX} contours (dashed lines) range from -1.0 K to 20.0 K in steps of 2.1 K. Tau contours (solid lines) range from -0.02 to 10.0 in steps of 1.0 K. The superthermal region is indicated. The hatched area at high $n(H_2)$, X/(dv/dr) values, is where the T_{EX} and tau are negative.

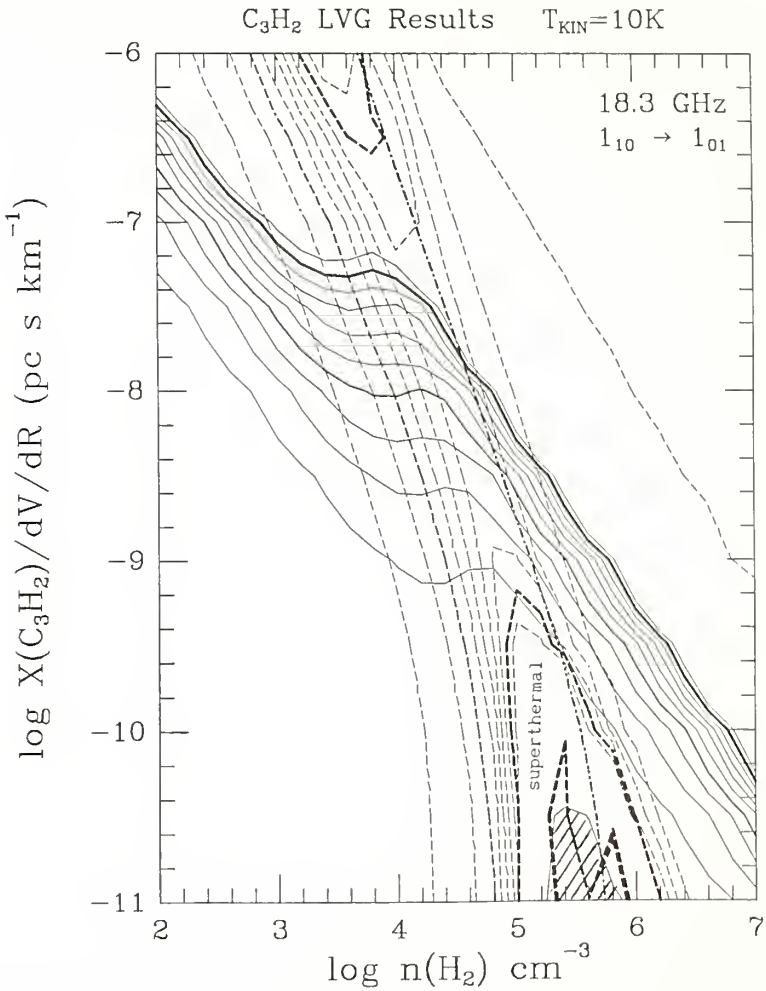
C_3H_2 LVG Results T_{KIN}=10K
18.3 GHz
$1_{10} \rightarrow 1_{01}$
superthermal
log $X(C_3H_2)/dV/dR$ (pc s km^{-1})
log $n(H_2)$ cm^{-3}
−6
−7
−8
−9
−10
−11
2
3
4
5
6
7

Figure 5.2) in the regions where the T_{EX} contours deviate from the vertical. As the opacity increases, the line intensity becomes independent of τ, and is equal to $J_\nu(T_{EX}) - J_\nu(T_{BG})$. The 18.3 GHz transition shows an interesting feature, as it become superthermal where the excitation temperature contours turn over (the hatched region) in Figure 5.4. This occurs in a relatively high density, low abundance region. This can more obviously be seen in Figure 5.5, where the behavior of T_{EX}, tau, and T_B as functions of $n(H_2)$ for the ortho lines are plotted individually for $X/(dv/dr) = 10^{-8}$ pc s km^{-1}, typical for dark clouds. At extremely low densities, the excitation temperature can decrease to that of the cosmic background temperature and at extremely high densities, the excitation temperature approaches the kinetic temperature of 10 K. In between, T_{EX} for the $1_{10} - 1_{01}$ transition begins a steep rise as thermalization is approached and finally becomes superthermal ($T_{EX} > T_{KIN}$). This effect can also be seen in a less dramatic way for the 85.3 GHz transition and in the $1_{11} - 0_{00}$ 51.8 GHz para transition (Figure 5.6). At the densities at which the superthermal effects occur, collisions are very effective in populating the upper levels of these transitions and eventually the upper states become *overpopulated*, resulting in a negative excitation temperature. This region is delineated in Figure 5.4 for the 18 GHz transition between $n(H_2) = 10^5$ to 10^6 cm^{-3} and $X/(dv/dr)$ less than 4×10^{-11} pc s km^{-1}. The optical depth is negative but very low, preventing sufficient amplification to observe a masing effect.

Figure 5.5 LVG results for the observed ortho lines. T_{EX}, τ, and T_B are given as functions of molecular hydrogen density for a uniform density source with a kinetic temperature of 10 K. Results are for $X/(dv/dr) = 1\times10^{-8}$ pc s km^{-1}.

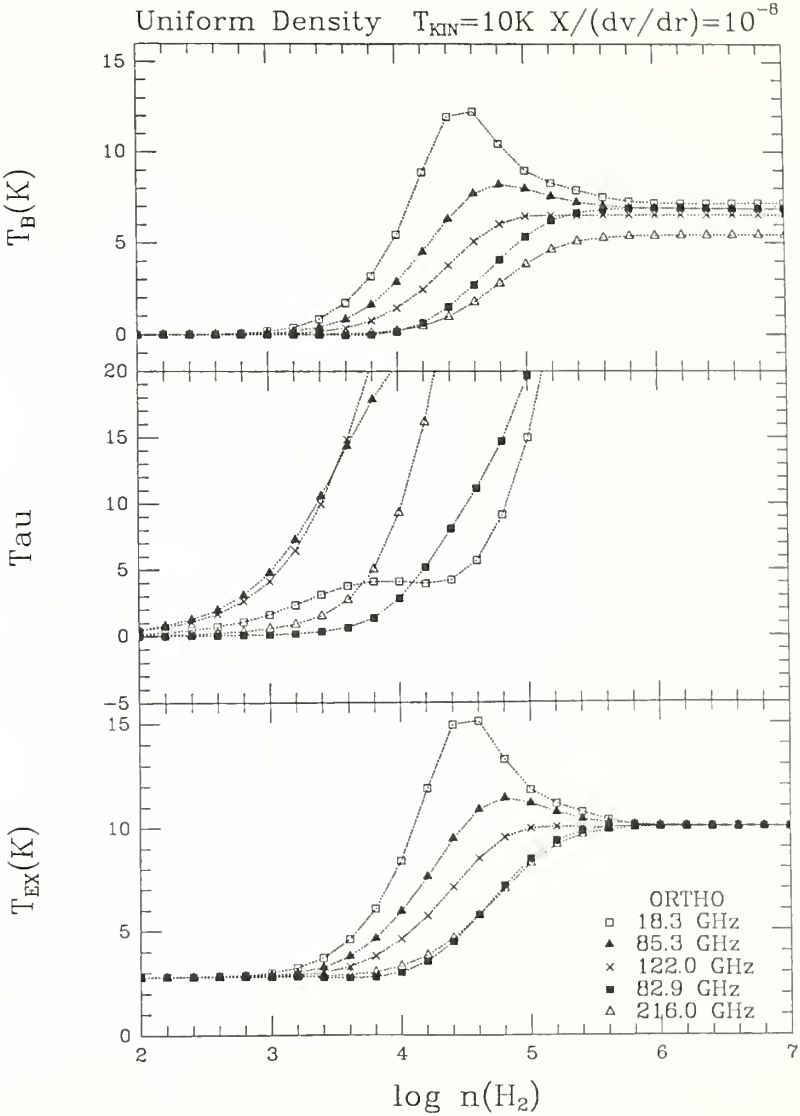
Uniform Density T_{KIN}=10K X/(dv/dr)=10^{-8}
T_B(K)
Tau
T_{EX}(K)
log n(H_2)
ORTHO
18.3 GHz
85.3 GHz
122.0 GHz
82.9 GHz
216.0 GHz

Figure 5.6 LVG results for the observed para lines. T_{EX}, τ, and T_B are given as functions of molecular hydrogen density for a uniform density source with a kinetic temperature of 10 K. Results are for $X/(dv/dr) = 1\times10^{-B}$ pc s km^{-1}.

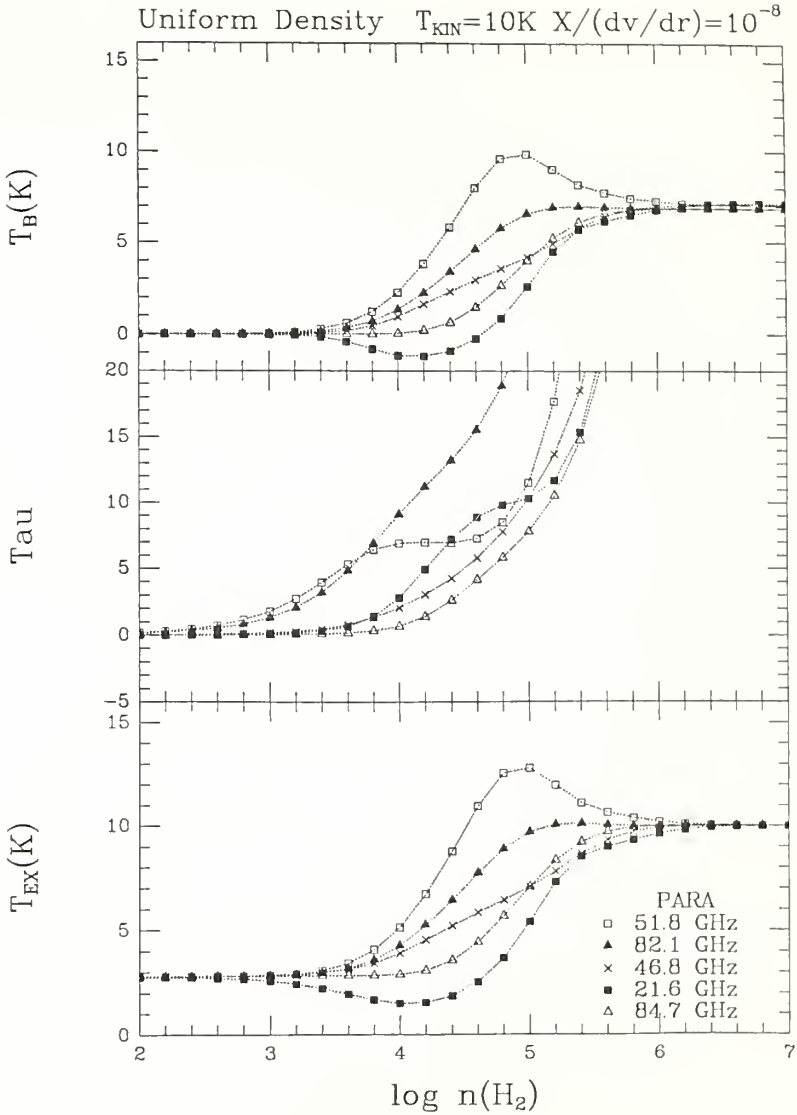
Uniform Density T_{KIN}=10K X/(dv/dr)=10^{-8}
T_B(K)
Tau
T_{EX}(K)
log n(H_2)
PARA
51.8 GHz
82.1 GHz
46.8 GHz
21.6 GHz
84.7 GHz

5.3.3 Two Component Model Description

Molecular clouds are not necessarily uniform in density. To take a simple step beyond the limits of the uniform density model, we have constructed a 2 component model consisting of a dense core surrounded by a less dense halo. This configuration is an attempt to remedy the problem in matching the 21 GHz observations (described in Chapter 6) by providing a low density halo for the needed additional absorption. Within the context of the LVG approximation, physical parameters such as T_{EX} and τ, for example, at any given location (i.e., the core) are independent of conditions elsewhere (i.e., the halo). This simple, yet limited, 2-component model attempts to avoid a prohibitive full radiative transfer solution for a multi-density configuration, and we benefit from the simplicity of the LVG calculation. We derive a new transfer equation constructed from local emission and absorption terms:

$$\begin{aligned} T_B = {} & J_\nu(T_{EX(h)})\ [1 - \exp(-\tau_h)]\ [1 + \exp-(\tau_c + \tau_h)] \\ & - J_\nu(T_{bg})\ [1 - \exp-(\tau_c + 2\tau_h)] \\ & + J_\nu(T_{EX(c)})\ \exp(-\tau_h)\ [1 - \exp\ (-\tau_c)] \end{aligned} \tag{5.28}$$

where

$$J_\nu(T) = h\nu/k\ [\exp(h\nu/kT) - 1]^{-1} \quad . \tag{5.29}$$

T_B is the observed brightness temperature, which takes into account subtraction of the background contribution consistent with the

observing technique. The terms $T_{EX(h)}$ and $T_{EX(c)}$ are excitation temperatures for the halo and core, and T_{BG} is the background contribution which, in the case of the dark clouds, is 2.7 K. The halo and core opacities are denoted by τ_h and τ_c. Equation 5.28 can be interpreted by considering the 3 terms separately. The first term is the sum of frontside halo contribution given by $J_\nu(T_{EX})[1 - \exp(-\tau_h)]$ plus the backside halo contribution attenuated by the core $[\exp(-\tau_c)]$ and frontside halo $[\exp(-\tau_h)]$; the second term is the background contribution attenuated through the front and backside halos $[\exp(-2\tau_h)]$ and the core $[\exp(-\tau_c)]$; the third term describes the core contribution attenuated by the frontside halo. We solve this new transfer equation based on optical depths and excitation temperatures determined from LVG calculations assuming a kinetic temperature of 10 K for both components.

Initially the parameter X/(dv/dr) remains constant for both the core and the halo, leaving 3 parameters to solve for: X/(dv/dr) and both a core and halo hydrogen density, n(core) and n(halo). Then we allow for different X/(dv/dr) in the core and halo - thus creating a 2-component model with 4 parameters to be varied independently while seeking the best fit physical parameters. In many cases, it is not necessarily beneficial to increase the number of free parameters, thereby decreasing the number of degrees of freedom. If the source is truly optimized with 3 parameters, or even 2 parameters (uniform density), decreasing the number of degrees of freedom may, in fact, *increase* the value of $\tilde{\chi}^2$.

Caution should be emphasized in the use of this simple 2-component model. The two components are treated independently in the sense that the LVG assumption is used to decouple the radiative interactions originating at one point in the source from others. However, in the expression for the observed intensity (equation 5.27) contributions from the separate regions are allowed to interact only in the sense that they are permitted to attenuate neighboring contributions. Model limitations would not be as severe for this two component model, for example, in the situation where the "halo" component is a separate foreground cloud. Radiative coupling in this case can become negligible if the solid angles of the mutual radiation contribution from the neighboring clouds is a small fraction of the total surrounding background radiation.

We signify a denser component versus a less dense component interchangeably as components 1 and 2, or core and halo. In some cases the terms core and halo are misleading when the densities do not contrast significantly.

5.3.4 Interpretation of the Two Component Model

Contours of constant brightness temperature are plotted for the 2-component model as functions of n(halo) and n(core) for a specific X/(dv/dr) value. Examples for the 18 and 21 GHz transitions can be seen in Figures 5.7 and 5.8. These figures can be interpreted in conjunction with Figures 5.5 and 5.6. Notice, for example, that when n(core) ~ $10^{4.5}$ to $10^{5.5}$ cm^{-3} and the halo density is low (less than

Figure 5.7 Constant brightness contours from the 2-component model for the $2_{20} - 2_{11}$ 21 GHz transition with X/(dv/dr) = 1×10^{-8} pc s km^{-1}. Contour values range from -1.2 to 7.2 K in steps of 0.84 K. Levels -1.2, 2.2, and 6.4 are represented by dashed lines of increasing thickness.

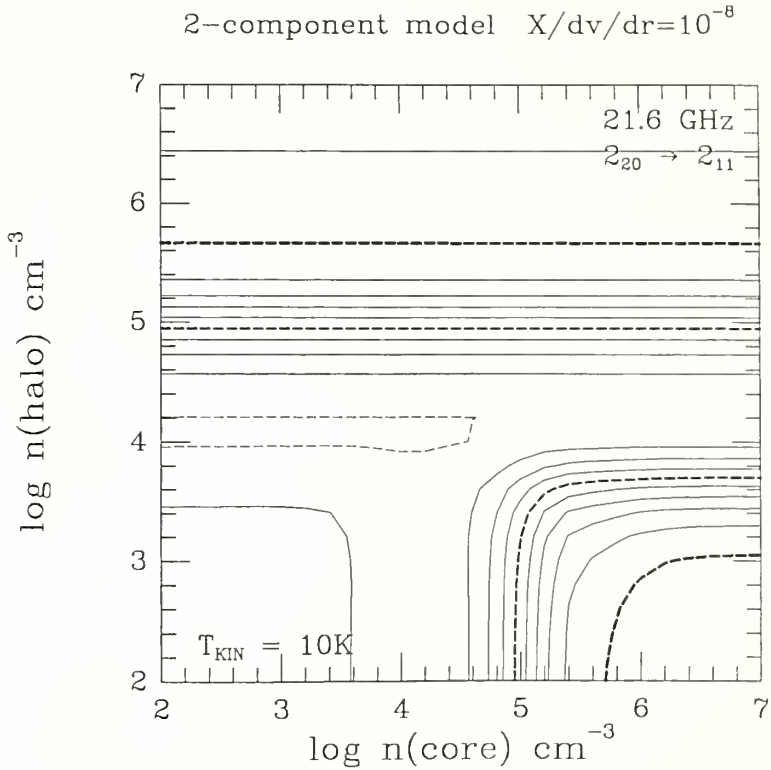
2-component model X/dv/dr=10^-8
21.6 GHz
2_20 → 2_11
T_KIN = 10K
log n(halo) cm^-3
log n(core) cm^-3
2
3
4
5
6
7

Figure 5.8 Constant brightness contours from the 2-component model for the $1_{10} - 1_{01}$ 18 GHz transition with X/(dv/dr) = 1×10^{-8} pc s km^{-1}. Contour values range from 0.0 to 12.0 K in steps of 1.2 K. Levels 0.0, 4.8, and 12.0 are represented by dashed lines of increasing thickness.

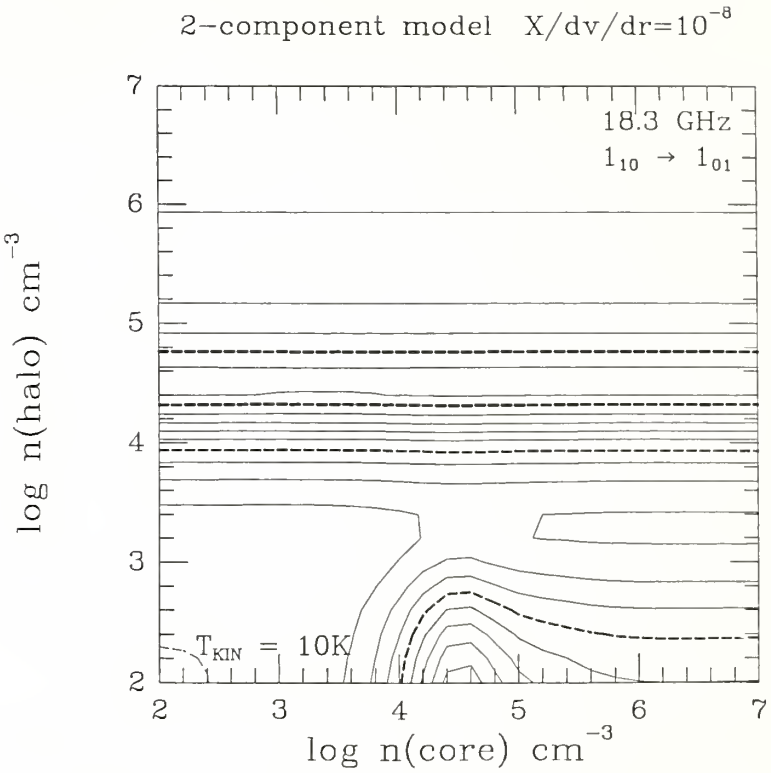
2-component model X/dv/dr=10^-8
18.3 GHz
1_10 → 1_01
T_KIN = 10K
log n(halo) cm^-3
log n(core) cm^-3
2
3
4
5
6
7

$10^{3.5}$ cm^{-3}) for the 2_{20} - 2_{11} transition (Figure 5.7), the optical depth of the halo is negligible we can "see" through the halo to the core. As the halo density increases, it begins to absorb some of the core emission, until optical depths are very large in the halo (n(halo) > $10^{4.5}$ cm^{-3}) and we can only "see" the halo - approaching a single component case comprising only a halo.

The results and limitations of the models are discussed in Chapter 6.

CHAPTER 6

ANALYSES OF OBSERVATIONS

6.1 Data Acquisition and Calibration

The data being used for the modeling of dark clouds consist of 4 to 10 different C_3H_2 transitions having energies (E/k) above the ground state ranging from 1 K to 17 K. Table 6.1 lists telescope information for the observations.

In addition, observations of the $1_{10} - 1_{01}$ transition were carried out August 1986 at the 100 m Effelsberg. The telescope was equipped with a K-band maser receiver together with a 1024 channel autocorrelator, operated as two 512 channel spectrometers of 3.12 MHz bandwidth each, giving a velocity resolution of 0.1 km s^{-1} at 18.3 GHz. The telescope half power beam width (HPBW) at this frequency is 55". The main beam temperature scale was determined by continuum measurements of NGC7027 with an assumed flux density of 5.8 Jy. Data obtained from maps made at the 100 m in the $1_{10}-1_{01}$ transition provided information on source size.

Details on the observing procedures and telescope parameters for the NRAO 43 m 18.3 and 21.8 GHz observations are discussed in section 3.2. Observations were carried out between 1985 and 1988. For these observations where the antenna temperatures were determined via a noise tube, there is no atmospheric attenuation naturally accounted for. This effect was estimated from tipping measurements and used to

Table 6.1

Observing Parameters

Transition	Frequency	η[1]	Telescope
$1_{10}-1_{01}$	18.3	0.33	43 m NRAO
$2_{12}-1_{01}$	85.3	0.69	14 m FCRAO
$2_{21}-1_{10}$	122.0	0.70	"
$3_{12}-3_{03}$	82.9	0.69	"
$3_{30}-2_{21}$	216.3	0.45	"
$1_{11}-0_{00}$	51.8	0.59	"
$2_{02}-1_{11}$	82.1	0.69	"
$2_{11}-2_{02}$	46.8	0.59	"
$2_{20}-2_{11}$	21.6	0.26	43 m NRAO
$3_{22}-3_{13}$	84.7	0.69	14 m FCRAO

Notes to Table 6.1:

[1] η refers to either η_{fss} for FCRAO observations or η_B (beam efficiency) for NRAO observation.

correct the antenna temperature values. However, at these wavelengths (~1.4 cm) the atmospheric effect is probably < 5%. The gain variations as a function of hour angle were also taken into account in the values presented in this chapter.

The chopper wheel method used to calibrate the observations at 7, 3 and 1 mm at the 14 m FCRAO antenna corrects for the rearward spillover and ohmic losses (Kutner and Ulich 1981). For the part of the beam pattern which observes the sky excluding the source contribution, the forward spillover correction (η_{fss}) is necessary to correct from T_A^* (direct chopper wheel result) to T_R^*. Inherent in the technique of determining T_A^* is the uncertainty in the measurement of the system temperature, which is a scaling factor. There is a further correction factor (C_{fac}) resulting from the ambient temperature differing from the sky temperature. This correction factor can be estimated from opacity estimates derived from standard tipping measurements (Kenny and Taylor 1988). Due to the atmospheric O_2 absorption, observations for the 46.8, 51.8, and 122.0 GHz transitions at FCRAO were corrected using C_{fac} values ranging from 1.05 to 1.2. More details conserning the observations at the 14 m telescope are described in section 3.2. The FCRAO observations were obtained during 1985 to 1988.

Finally, to correct to brightness temperature, T_B, which is the value used in the calculations, a factor accounting for the coupling of the source to the beam, η_c, was estimated from mapping information. Main beam brightness temperatures (T_B) are determined using a source coupling factor:

$$\eta_c = (1 + (\vartheta_B/\vartheta_{S_x})^2)^{-0.5} (1 + (\vartheta_B/\vartheta_{S_y})^2)^{-0.5} \qquad (6.1)$$

where ϑ_B is the telescope HPBW and ϑ_{S_x} and ϑ_{s_y} are the source half power widths in the 2 dimensions in the plane of the sky.

In the following sections observations for several dark cloud sources are presented and interpreted in light of the modeling scheme described in Chapter 5.

6.2 TMC-1

6.2.1 Observations

The Taurus Molecular Cloud One (TMC-1), always known for its richness in molecules, proves to also be a wealthy source of C_3H_2. Ten C_3H_2 transitions observed in wavelengths ranging from 1.3 cm to 1.3 mm were used to analyze this source. Maps of C_3H_2 reveal a conspicuous well known filamentary structure, elongated in the NW-SE direction, also seen in other molecules (Snell, Langer and Frerking 1982; Olano, Walmsley and Wilson 1988). The extent of the 18 GHz 1_{10}- 1_{01} C_3H_2 emission can be seen in maps of the T_B and integrated intensity (Figure 6.1) obtained at the 100 m antenna. Map grid spacing is 30", 1/2 of the telescope HPBW at 18.3 GHz. The emission peaks near the well known peak position of the long chain organic molecules known as cyanopolyynes: RA = $04^h38^m38^s.6$; DEC = $25^\circ35'45''$,

Figure 6.1 Brightness temperature contours (left) and integrated intensity (right) of the $1_{10} - 1_{01}$ C_3H_2 transition in TMC-1. Brightness temperature contour values are 2.0 to 8.0 in steps of 0.6 K. Levels 2.0, 4.4 and 7.4 K are represented by dashed lines of increasing thickness. Integrated brightness contours range from 1.0 to 4.5 in steps of .35 K km s^{-1}. Levels 1.0, 2.4 and 4.15 are represented by dashed lines of increasing thickness.

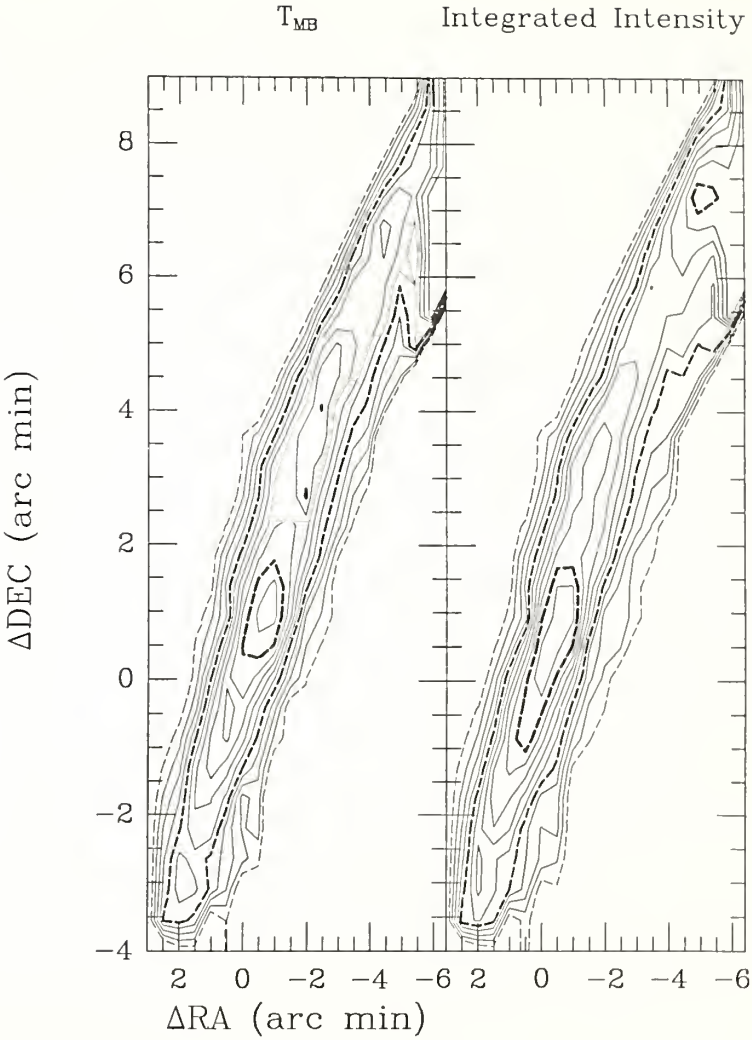
T_{MB}
Integrated Intensity
8
6
4
2
0
−2
−4
ΔDEC (arc min)
2
0
−2
−4
−6
2
0
−2
−4
−6
ΔRA (arc min)

denoted by the offsets (ΔRA,ΔDEC) = (0,0). However, the peak C_3H_2 position appears to be 40" west and 1' north of the (0,0) position, an offset which is considerably larger than the pointing errors of ±10". The intensity decreases by about 40% toward the northwest at the (-4,6) position where NH_3 is known to peak (Tölle *et al.* 1981; Olano, Walmsley and Wilson 1988). The map of T_B appears more fragmented than that of the integrated intensity. The spatial extent of the emission to 1/2 peak intensity as seen in C_3H_2 is approximately 2' x 17'. At a distance of 140 pc this corresponds to dimensions of 0.08 pc x 0.7 pc, which are smaller than those observed in CS, CH_3OH and $C^{18}O$ emission (Snell, Langer and Frerking 1982; Langer, Frerking and Wilson 1986; Friberg *et al.* 1988) and larger than those found for the cyanopolyynes and NH_3 (Tölle *et al.* 1981).

Individual 1_{10}-1_{01} spectra from the 100 m map, spaced by 90" along the ridge, are displayed in Figure 6.2. A variety of line profiles is seen, with half widths ranging from 0.55 km s^{-1} in the south east (0.8,-1.2) to a 1.5 km s^{-1} line in the north (-5.1,7.4). Line center V_{LSR} values range from 5.2 to 6.3 km s^{-1}. This may be due, in part, to blending of several velocity components. Line broadening due to optical depth effects is also a possibility. Snell, Langer and Frerking (1982) conclude that 6 fragments in TMC-1, of roughly 0.2 pc in size, account for the various line widths and central velocities. The sharp fall off across the ridge can also be seen in the spectra observed perpendicular to the ridge at the (0,0) position (Figure 6.3).

Figure 6.2 Spectra observed along the ridge in TMC-1. These observations of the $1_{10}-1_{01}$ transition of C_3H_2 were obtained at the 100 m Effelsberg telescope. Spectra are taken at 90" spacings. The offsets indicated for each profile are in arc minutes with respect to RA: $04^h38^h38^s$ and DEC: $25^o35'45$. The velocity resolution is ~ 0.1 km s^{-1}.

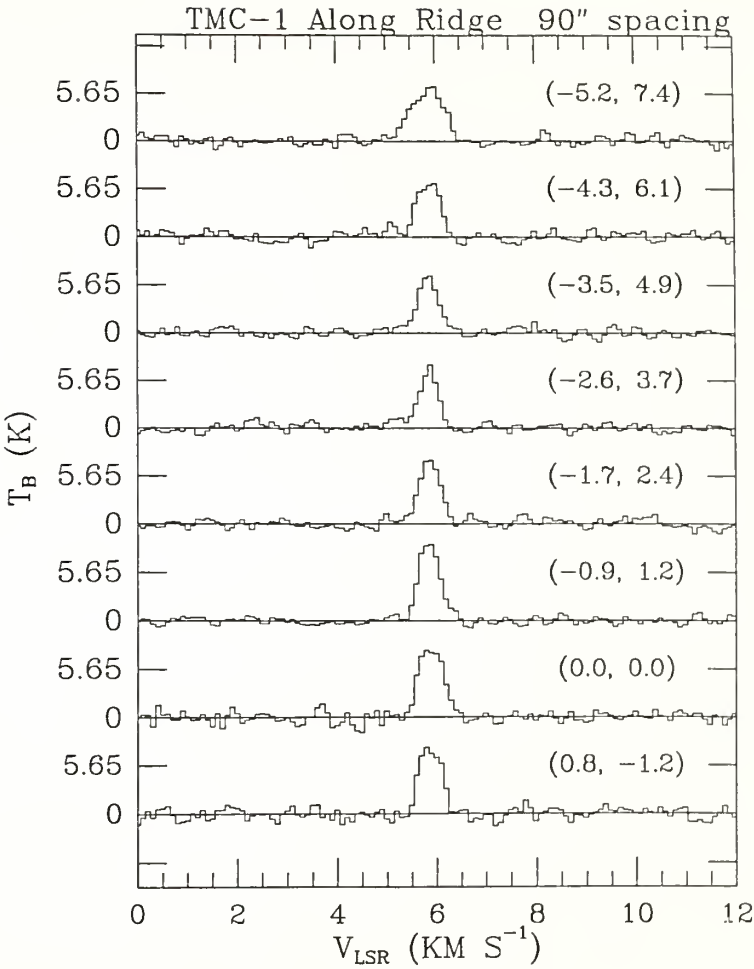
TMC−1 Along Ridge 90″ spacing
(−5.2, 7.4)
(−4.3, 6.1)
(−3.5, 4.9)
(−2.6, 3.7)
(−1.7, 2.4)
(−0.9, 1.2)
(0.0, 0.0)
(0.8, −1.2)
5.65
0
T_B (K)
0
2
4
6
8
10
12
V_{LSR} (KM S^{-1})

Figure 6.3 Spectra observed across the ridge in TMC-1 at the (0,0) position. These observations are of the $1_{10}-1_{01}$ C_3H_2 transition were obtained at the 100 m Effelsberg telescope. Spectra are taken at 90" spacings.
The offsets indicated for each profile are in arc minutes with respect to RA: $04^h38^h38^s$ and DEC: $25^o35'45$.

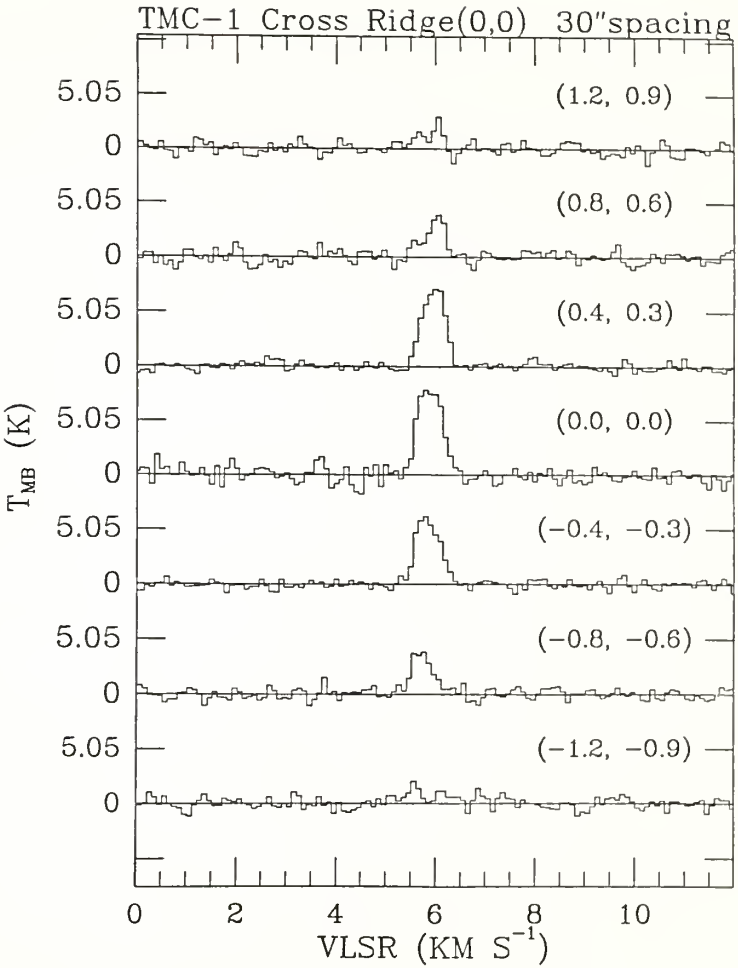
TMC−1 Cross Ridge(0,0) 30″spacing
5.05
0
(1.2, 0.9)
(0.8, 0.6)
(0.4, 0.3)
(0.0, 0.0)
(−0.4, −0.3)
(−0.8, −0.6)
(−1.2, −0.9)
T_{MB} (K)
0
2
4
6
8
10
VLSR (KM S^{-1})

Spectra along the TMC-1 ridge through the (0,0) position obtained with the NRAO 43 m telescope are presented in Figure 6.4 toward similar but not identical positions. The effect of the larger beam at the 43 m telescope (1.'8) is not very apparent - aside from the prominent double peaked spectra at the (0,0) position, which is likely due to multiple fragments within the beam.

The distribution of the $2_{20} - 2_{11}$ 21 GHz absorption along the TMC-1 ridge (Figure 6.5) is similar to that for the $1_{10} - 1_{01}$ 18 GHz emission line, with both having a similar velocity structure. The $2_{11} - 2_{02}$ (46.8 GHz) and $2_{21} - 1_{10}$ (122 GHz) transitions are shown toward 5 positions at 3.'8 spacings along the ridge in Figures 6.6 and 6.7. The presence of multiple velocity components is apparent in the 46.8 GHz spectra. The line profile just southeast of the (0,0) position shows a velocity component shifted 0.4 km s^{-1} lower than that just northwest of the (0,0) position, while the (0,0) profile is wide, containing both velocity components. The remaining transitions from TMC-1 have been observed only toward the (-4,6) and (0,0) positions.

Figures 6.8a and 6.8b show the complete collection of the 10 ortho and para transitions of C_3H_2 observed toward the (0,0) position in TMC-1 (Table 6.2). This is our largest number of observed C_3H_2 transitions for any one source. Except for the para $3_{22} - 3_{12}$ (84.7 GHz) and ortho $3_{30} - 2_{21}$ (216 GHz) transitions, all lines have similar widths (~0.5 - 0.6 km s^{-1}). The two exceptions are narrow (.23 to .3 km s^{-1}), have relatively high excitation requirements (E/k = 16 and 17 K above the ground levels) and are weak lines with low

Figure 6.4 Spectra observed along the ridge in TMC-1. These observations are of the $1_{10}-1_{01}$ C_3H_2 transition were obtained at the 43 m NRAO telescope. Spectra are taken at 1.'9 spacings. The offsets indicated for each profile are in arc minutes with respect to RA: $04^h38^h38^s$ and DEC: $25^\circ35'45$. The velocity resolution is 0.8 km s^{-1}, similar to that of Figure 6.2.

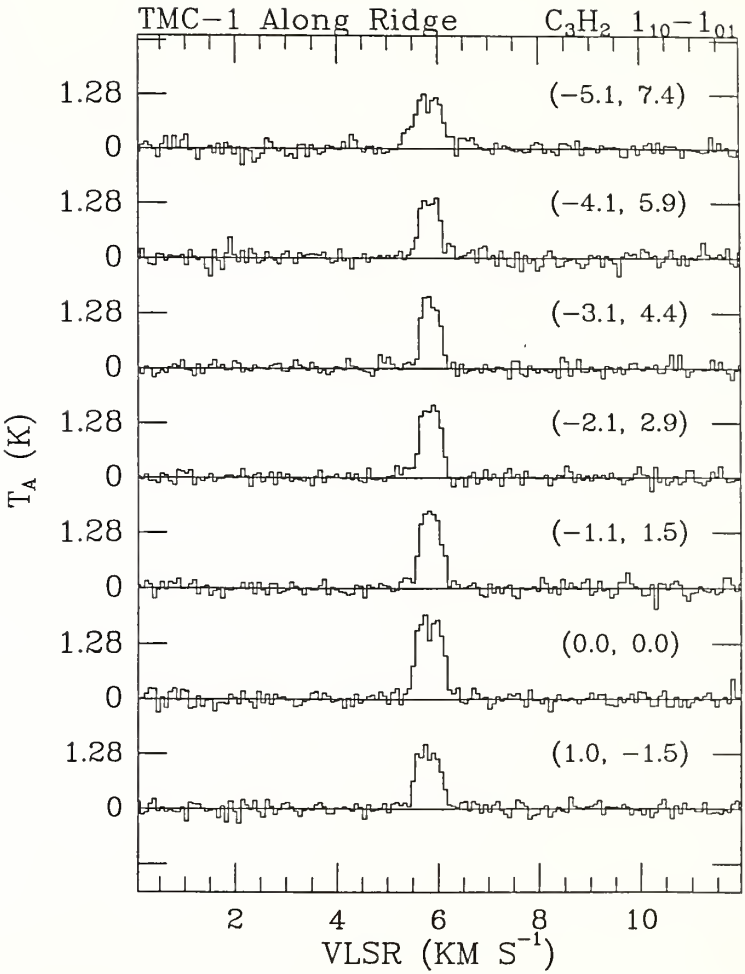
TMC−1 Along Ridge
C_3H_2 $1_{10}-1_{01}$
1.28
0
(−5.1, 7.4)
(−4.1, 5.9)
(−3.1, 4.4)
(−2.1, 2.9)
(−1.1, 1.5)
(0.0, 0.0)
(1.0, −1.5)
T_A (K)
2
4
6
8
10
VLSR (KM S^{-1})

Figure 6.5 C_3H_2 $2_{20}-2_{11}$ spectra observed along the ridge in TMC-1. Observations were obtained at the 43 m NRAO telescope. Spectra are taken at 1.'9 spacings. The offsets indicated for each profile are in arc minutes with respect to RA: $04^h38^h38^s$ and DEC: $25^\circ35'45$. The velocity resolution is similar to that in Figure 6.4.

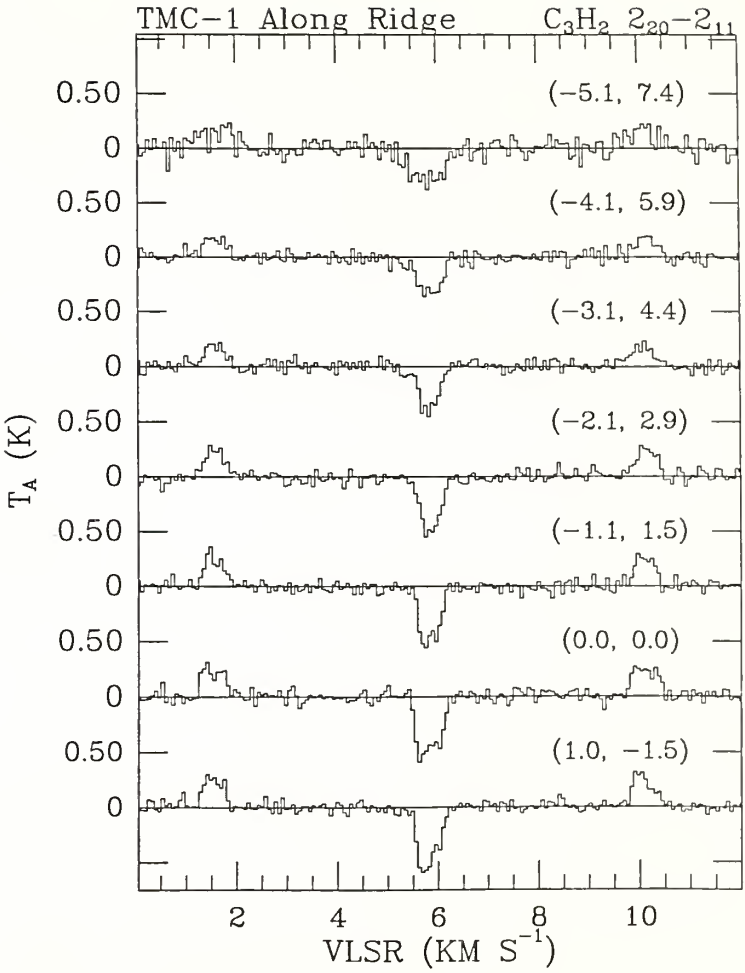
TMC−1 Along Ridge
C_3H_2 $2_{20}-2_{11}$
0.50
0
(−5.1, 7.4)
(−4.1, 5.9)
(−3.1, 4.4)
(−2.1, 2.9)
(−1.1, 1.5)
(0.0, 0.0)
(1.0, −1.5)
T_A (K)
2
4
6
8
10
VLSR (KM S^{-1})

Figure 6.6 $2_{11}-2_{02}$ C_3H_2 spectra observed along ridge in TMC-1. Observations were obtained with the 14 m FCRAO telescope. Spectra are taken at 3.'8 spacings. The offsets indicated for each profile are in arc minutes with respect to RA: $04^h38^h38^s$ and DEC: 25°35'45. The velocity resolution is 0.08 km s^{-1}.

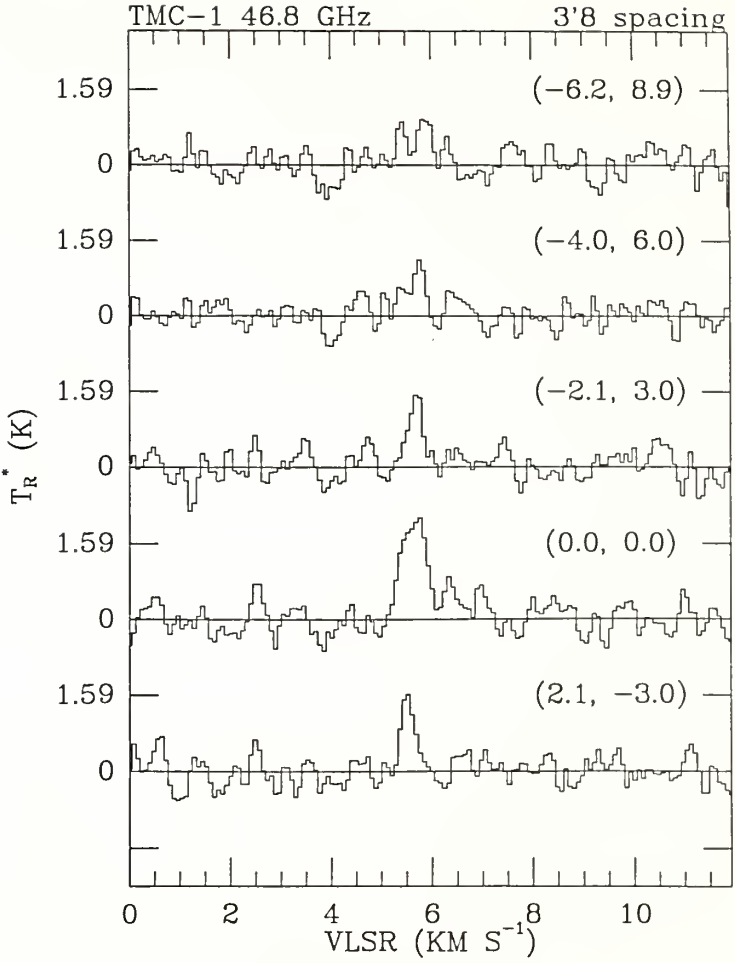
TMC−1 46.8 GHz
3'8 spacing
1.59
0
(−6.2, 8.9)
(−4.0, 6.0)
(−2.1, 3.0)
(0.0, 0.0)
(2.1, −3.0)
T_R^* (K)
0
2
4
6
8
10
VLSR (KM S^{-1})

Figure 6.7 $2_{21}-1_{10}$ C_3H_2 spectra observed along the ridge in TMC-1. Observations were obtained with the 14 m FCRAO telescope. Spectra are taken at 3.'8 spacings. The offsets indicated for each profile are in arc minutes with respect to RA: $04^h38^h38^s$ and DEC: $25^\circ35'45$. The velocity resolution is 0.06 km s^{-1}.

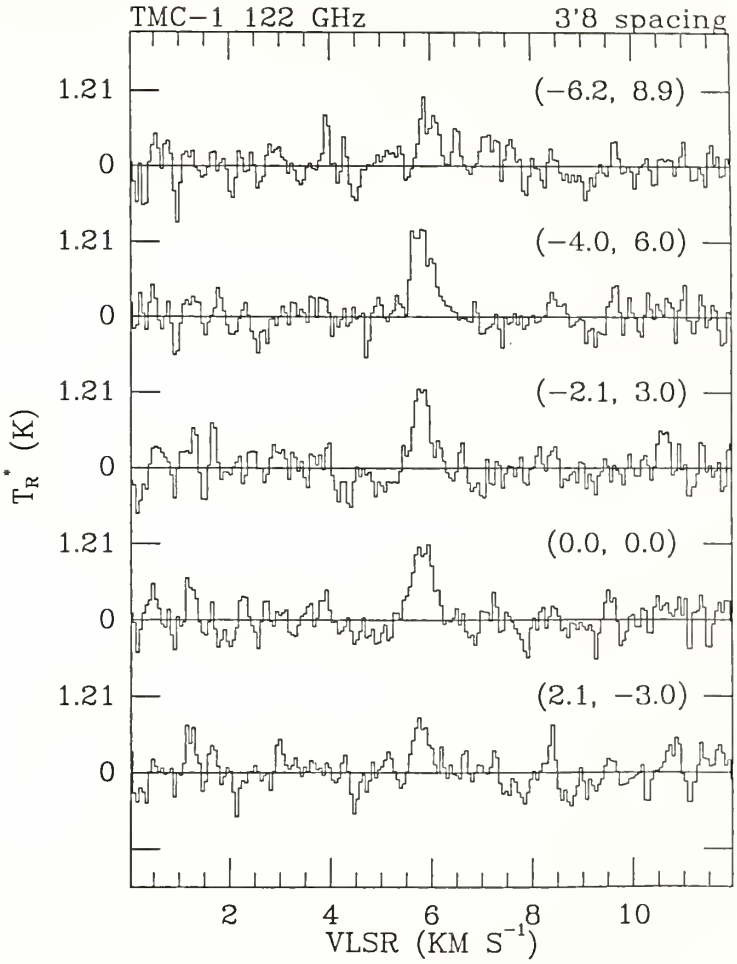
TMC−1 122 GHz
3'8 spacing
1.21
0
(−6.2, 8.9)
(−4.0, 6.0)
(−2.1, 3.0)
(0.0, 0.0)
(2.1, −3.0)
T_R^* (K)
2
4
6
8
10
VLSR (KM S^{-1})

Figure 6.8a,b Observed C_3H_2 spectra in TMC-1. For each of the ortho (a) and para (b) profiles the transition, frequency and energy above the ground state (K) are indicated. The intensities have been corrected for atmospheric attenuation and source-beam coupling (described in section 6.1). Table 6.1 contains the telescope parameters for the observations.

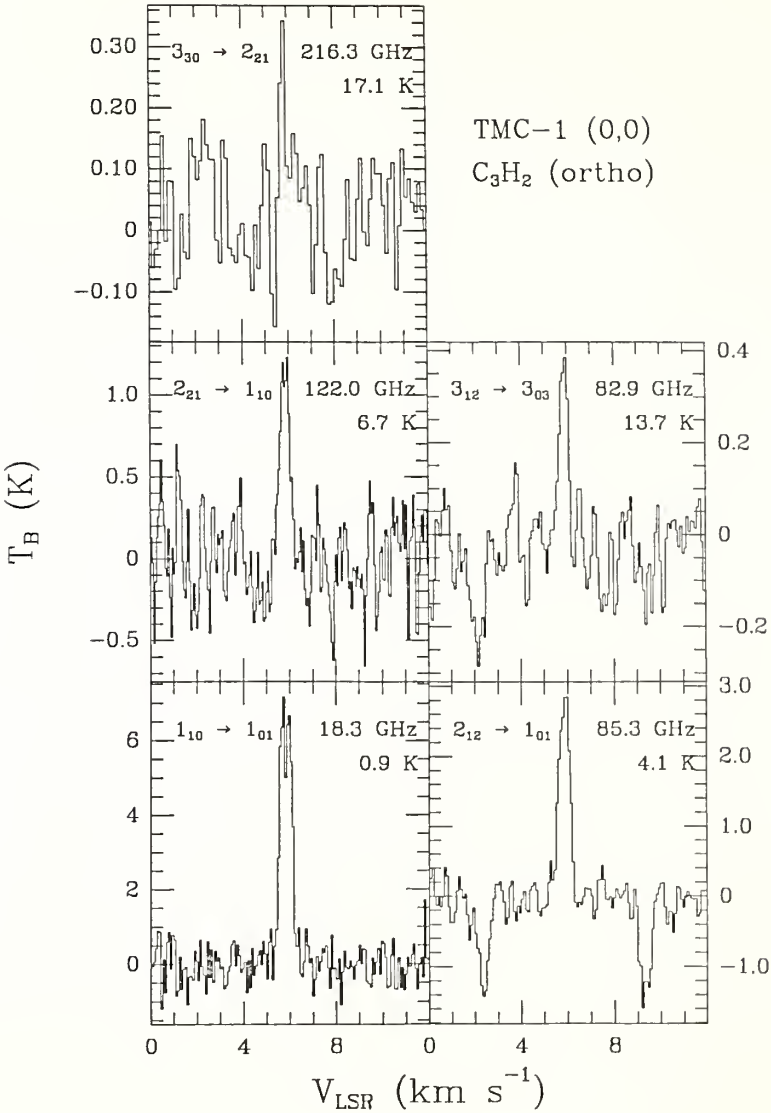
TMC−1 (0,0)
C3H2 (ortho)
3_30 → 2_21
216.3 GHz
17.1 K
2_21 → 1_10
122.0 GHz
6.7 K
3_12 → 3_03
82.9 GHz
13.7 K
1_10 → 1_01
18.3 GHz
0.9 K
2_12 → 1_01
85.3 GHz
4.1 K
T_B (K)
V_LSR (km s^-1)

(a)

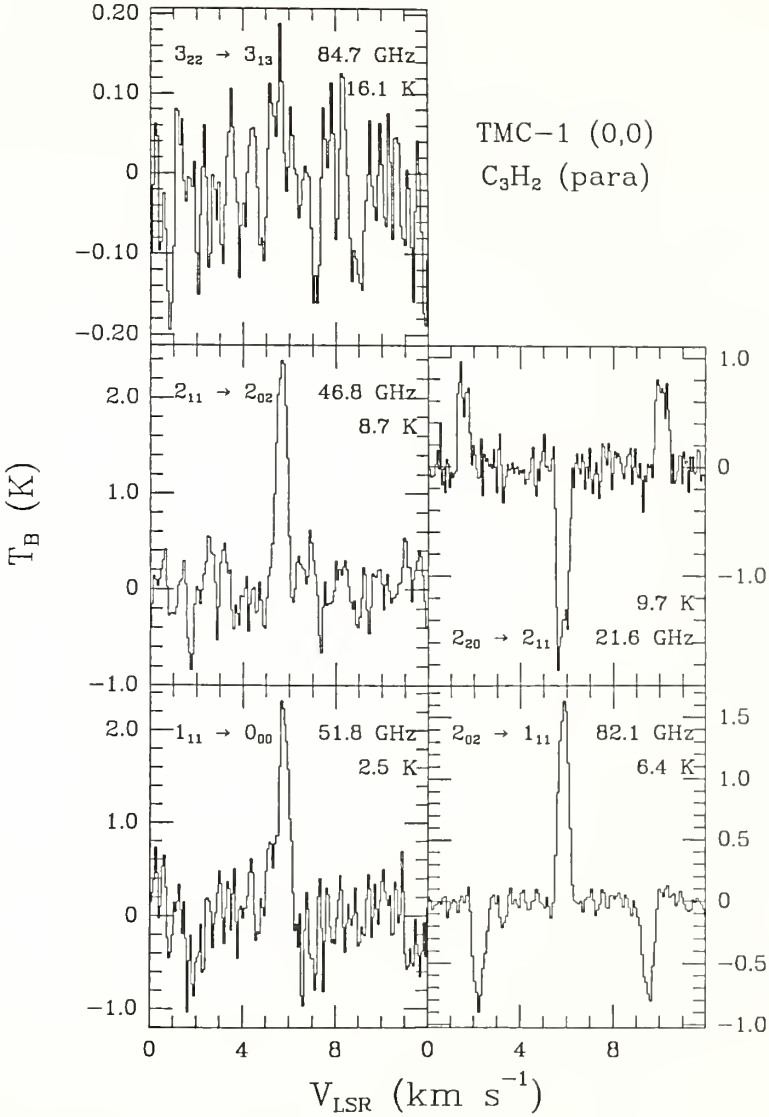
TMC−1 (0,0)
C_3H_2 (para)
$3_{22} \rightarrow 3_{13}$ 84.7 GHz
16.1 K
$2_{11} \rightarrow 2_{02}$ 46.8 GHz
8.7 K
$2_{20} \rightarrow 2_{11}$ 21.6 GHz
9.7 K
$1_{11} \rightarrow 0_{00}$ 51.8 GHz
2.5 K
$2_{02} \rightarrow 1_{11}$ 82.1 GHz
6.4 K
T_B (K)
V_{LSR} (km s^{-1})

(b)

Table 6.2

Summary of TMC-1 C_3H_2 Observations

Position[1] (ΔRA, ΔDEC)	Line	Frequency[2] (GHz)	T_B[3] (K)	σ[4] (K)	V_{LSR}	ΔV[5]	resol
					.....(km s^{-1}).....		
(0,0)	$1_{10}-1_{01}$	18.3	6.6	0.35	5.73	0.58	0.09
	$2_{12}-1_{01}$	85.3	2.9	0.20	5.97	0.60	0.09
	$2_{21}-1_{10}$	122.0	1.2	0.26	5.94	0.46	0.06
	$3_{12}-3_{03}$	82.9	0.37	0.12	5.96	0.46	0.10
	$3_{30}-2_{21}$	216.3	0.33	0.11	5.85	0.23	0.14
	$1_{11}-0_{00}$	51.8	2.3	0.34	5.67	0.61	0.07
	$2_{02}-1_{11}$	82.1	1.6	0.10	5.88	0.49	0.09
	$2_{11}-2_{02}$	46.8	2.4	0.24	5.52	0.32	0.08
	$2_{20}-2_{11}$	21.6	-1.8	0.45	5.62	0.49	0.08
	$3_{22}-3_{13}$	84.7	0.20	0.10	5.60	0.51	0.09
(-4,6)	$1_{10}-1_{01}$	18.3	4.82	0.42	5.97	0.49	0.09
	$2_{12}-1_{01}$	85.3	2.10	0.20	5.93	0.47	0.09
	$2_{21}-1_{10}$	122.0	1.40	0.23	5.82	0.51	0.06
	$1_{11}-0_{00}$	51.8	1.51	0.28	5.81	0.42	0.07
	$2_{02}-1_{11}$	82.1	1.27	0.14	5.88	0.63	0.18
	$2_{11}-2_{02}$	46.8	1.18	0.24	5.76	0.41	0.08
	$2_{20}-2_{11}$	21.6	-1.2	0.37	5.76	0.56	0.08
(2,-3)	$1_{10}-1_{01}$	18.3	4.39	0.42	5.73	0.53	0.09
	$2_{21}-1_{10}$	122.0	0.96	0.27	5.76	0.38	0.06
	$2_{11}-2_{02}$	46.8	1.6	0.30	5.53	0.32	0.08
	$2_{20}-2_{11}$	21.6	-1.8	0.48	5.68	0.61	0.08

(continued on next page)

Table 6.2

(continued)

Position[1] (Δra, Δdec)	Line	Frequency[2] (GHz)	T_B[3] (K)	σ[4] (K)	V_{LSR}	ΔV[5]	resol
					.....(km s^{-1}).....		
(-2,3)	$1_{10}-1_{01}$	18.3	5.15	0.33	5.89	0.50	0.09
	$2_{21}-1_{10}$	122.0	1.40	0.28	5.76	0.34	0.06
	$2_{11}-2_{02}$	46.8	1.5	0.40	5.68	0.33	0.08
	$2_{20}-2_{11}$	21.6	1.7	0.52	5.76	0.44	0.08

Notes to Table 6.2:

[1] Position offsets are in arc minutes relative to RA: $04^h38^m38^s$; DEC: 25°35'45".

[2] Frequencies are from Thaddeus, Vrtilek, and Gottlieb (1985).

[3] T_B refers to brightness temperatures corrected for atmosphere, antenna gain and source - beam coupling (described in section 6.1).

[4] Refers to the 1 σ noise rms of the baseline.

[5] ΔV is the full width at half maximum, in km s^{-1}, of the observed line.

signal-to-noise ratio (S/N). The mean velocity width of all the TMC-1 lines is 0.49 km s^{-1} with a standard deviation of 0.12 km s^{-1}. Notice also the refrigeration effect of the $2_{20} - 2_{11}$ (21 GHz) transition observed in absorption against the 2.7 K cosmic microwave background, while all other lines are seen in emission.

6.2.2 Model Results

The results for both the uniform density model and the 2-component model will be explored throughly for TMC-1 as an example.

$\tilde{\chi}^2$ contours for the TMC-1 (0,0) position are shown in Figure 6.9 as a function of log X/(dv/dr) and log $n(H_2)$ for the uniform density model. The parameters which fit the model to observations most successfully are chosen to correspond to the minumum contour. Since 10 transitions were used for this calculation with 2 free parameters, the number of degrees of freedom is 8. While there seem to be several minimum regions, an isolated "best fit" minimum can be seen in the figure, and the search routine (described in section 5.4) evaluates $\tilde{\chi}^2$ throughout the $n(H_2)$, X/(dv/dr) plane to locate the minimum at $n(H_2) = 6.2\times10^3$ cm^{-3} and X/(dv/dr) = 3.3×10^{-8} pc s km^{-1} with $\tilde{\chi}^2 = 2.5$. These fit parameters for the (0,0) position correspond to a column density of $C_3H_2 = 3.0(\pm1.2) \times 10^{14}$ cm^{-2} based on a mean velocity line width of 0.49 km s^{-1}. If we consider the other "minimum" region seen in the figure at log $n(H_2)$ = 4.5 and log X/(dv/dr) = -9.0, a $\tilde{\chi}^2$ value of 4.0 is determined. The difference bbetween a fit of 2.5 and 4.0 for 8 free parameters is not very

Figure 6.9 $\tilde{\chi}^2$ contours of the uniform density model results for TMC-1 (0,0). The number of degrees of freedom (nfree) = 8. Contour values range from 3.0 to 30.0 in steps of 2.7. Levels 13.8 and 27.3 are represented by dashed contours of increasing thickness.

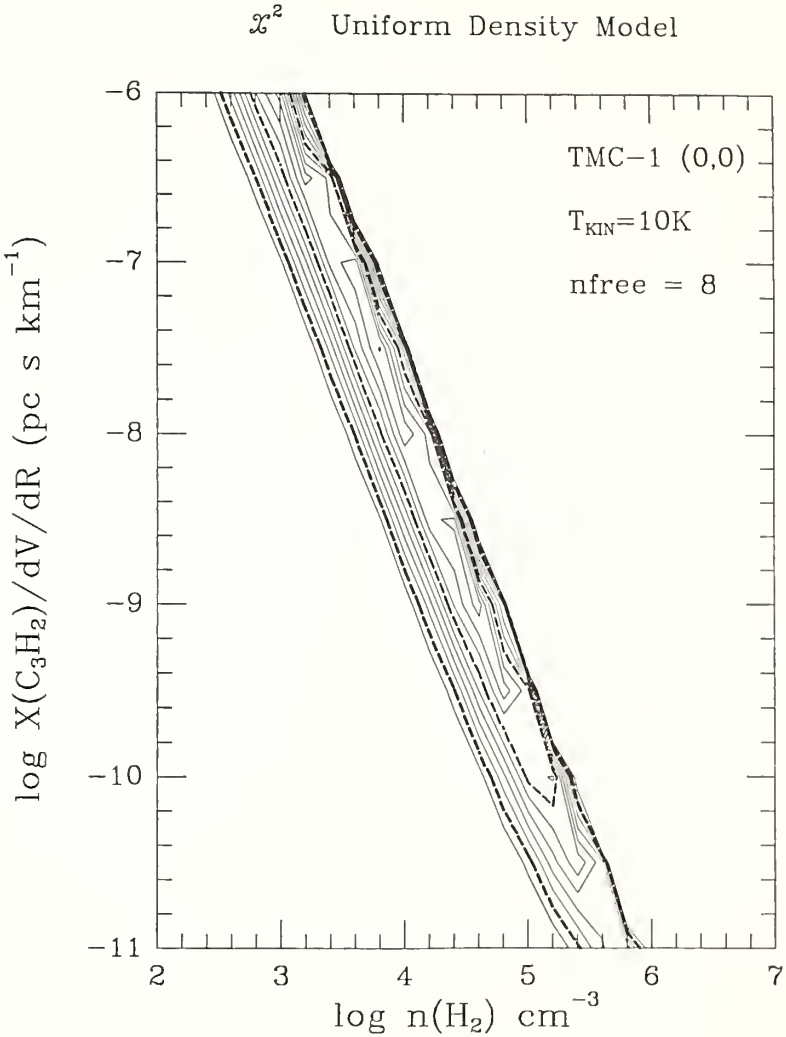
χ^2 Uniform Density Model
TMC−1 (0,0)
T_{KIN}=10K
nfree = 8
log X(C_3H_2)/dV/dR (pc s km^{-1})
log n(H_2) cm^{-3}
−6
−7
−8
−9
−10
−11
2
3
4
5
6
7

significant. It is perhaps more reasonable to conclude that the best fit includes the "valley" of contours (Figure 6.8) ranging from log $X/(dv/dr) = -9.2$ to -7.0 and log $n(H_2) = 3.3$ to 4.6. The column density range in this case is 3.7×10^{13} to 3.0×10^{14} cm^{-2}. We will, however, proceed with the analysis assuming a best fit solution for $\tilde{\chi}^2 = 2.5$.

A comparison of the observations with the model predictions for T_B for this best fit uniform density solution for TMC-1 (0,0) where $\tilde{\chi}^2 = 2.5$ is shown in Figure 6.10 for 5 ortho lines plotted as a function of E/k (K) above the ground ortho level and 5 para lines plotted as a function of E/k (K) above the ground para level. The 1σ formal error bars (described in section 5.4.1) are indicated in the figure. All but 3 of the model predictions lie within 1σ of the observations, with the most deviant results being the underpredicted para 46.8 and 21.6 GHz transitions. It is interesting to note that the upper level of the $2_{11}-2_{02}$ 46.8 GHz transition is the lower level of the $2_{20}-2_{11}$ 21.8 GHz absorption transition (see energy level diagram, Figure 2.2). Underestimating the emission in the 46.8 GHz line as the model does requires insufficient population in the 2_{11} level, which is also consistent with underpredicting the $2_{20}-2_{11}$ absorption. The 21 GHz line fails to be successfully predicted in other sources discussed in this chapter. Table 6.3 describes the model results for this solution.

The uniform density model can be more useful if additional parameters can constrain the solutions for $X/(dv/dr)$ and $n(H_2)$. We notice that optical depth contours (Figure 5.2) might be useful in

Figure 6.10 Comparison of model with observations for the uniform density model in TMC-1 (0,0). Brightness temperatures are indicated for the ortho lines (top) and para lines (bottom) as functions of E/k (K) above the respective ortho or para levels. Each transition is indicated by frequency (GHz) above the data points. The fit parameters, $n(H_2)$ and X/(dv/dr) are indicated along with the $\tilde{\chi}^2$ value for the fit.

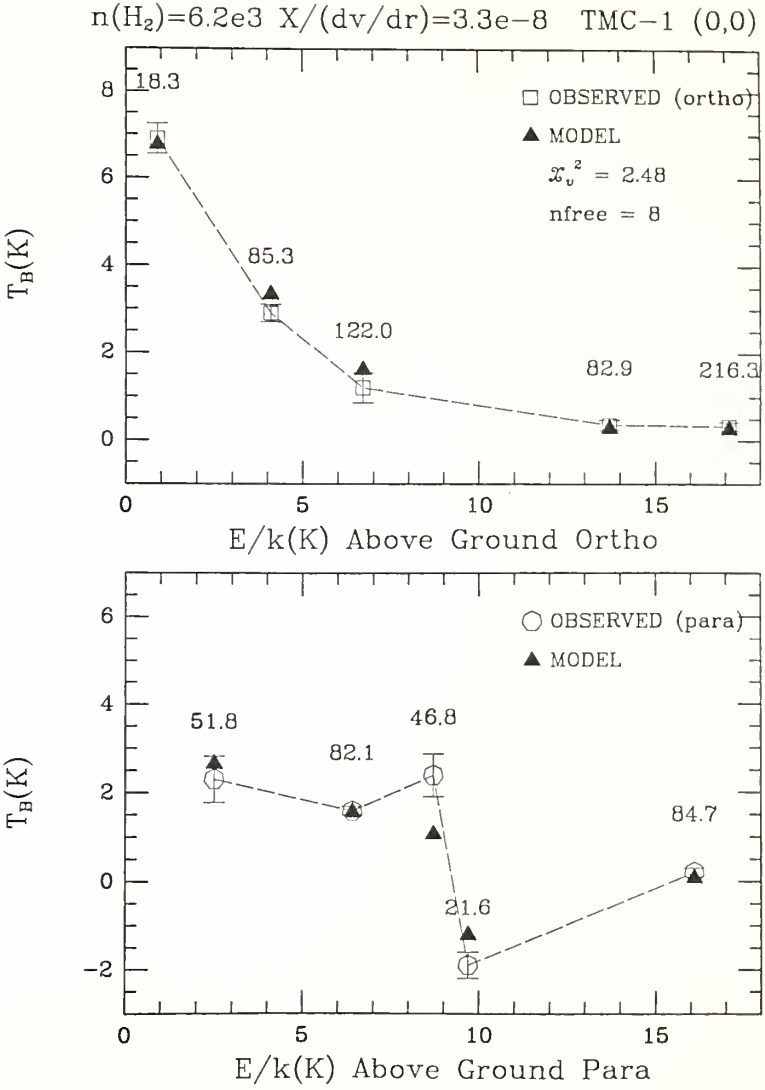
n(H2)=6.2e3 X/(dv/dr)=3.3e−8 TMC−1 (0,0)
OBSERVED (ortho)
MODEL
χ_ν² = 2.48
nfree = 8
18.3
85.3
122.0
82.9
216.3
T_B(K)
E/k(K) Above Ground Ortho
OBSERVED (para)
MODEL
51.8
82.1
46.8
21.6
84.7
T_B(K)
E/k(K) Above Ground Para

Table 6.3

Summary of Model Results for TMC-1 (Uniform Density)[1]

Position[2] (ΔRA, ΔDEC)	log n (cm^{-3})	log X/(dv/dr) (pc s km^{-1})	$\tilde{\chi}^2[\nu]$[3]	N (C_3H_2) (cm^{-2})
(0,0)	3.79(.35)	-7.48(.45)	2.5[8]	$3.0(1.2)\times10^{14}$
Transition		TEX(K)	τ	
$1_{10}-1_{01}$		9.59	7.18	
$2_{12}-1_{01}$		6.39	38.86	
$2_{21}-1_{10}$		4.78	53.20	
$3_{12}-3_{03}$		3.13	6.28	
$3_{30}-2_{21}$		3.41	20.24	
$1_{11}-0_{00}$		5.53	12.73	
$2_{02}-1_{11}$		4.53	17.80	
$2_{11}-2_{02}$		3.94	4.40	
$2_{20}-2_{11}$		1.55	6.06	
$3_{22}-3_{13}$		2.90	1.58	
(-4,6)	3.95(.25)	-8.01(.18)	0.9[5]	$1.3(.32)\times10^{14}$
$1_{10}-1_{01}$		7.69	4.06	
$2_{12}-1_{01}$		5.53	19.59	
$2_{21}-1_{10}$		4.34	24.78	
$1_{11}-0_{00}$		4.83	6.69	
$2_{02}-1_{11}$		4.08	8.36	

(continued on next page)

Table 6.3

(continued)

Position[2] (Δra, Δdec)	log n (cm^{-3})	log X/(dv/dr) (pc s km^{-1})	$\tilde{\chi}^2[\nu]$[3]	N (C_3H_2) (cm^{-2})
(-4,6)	3.95(.25)	-8.01(.18)	0.9[5]	$1.3(.32)\times10^{14}$
	$2_{11}-2_{02}$	3.77	1.82	
	$2_{20}-2_{11}$	1.57	2.38	
(2,-3)	3.44(.30)	-7.52(.25)	3.4[2]	$1.1(.4) \times 10^{14}$
	Transition	TEx(K)	τ	
	$1_{10}-1_{01}$	7.55	7.01	
	$2_{21}-1_{10}$	4.15	42.78	
	$2_{11}-2_{02}$	3.57	3.09	
	$2_{20}-2_{11}$	1.65	3.66	
(-2,3)	3.99(.22)	-8.01(.27)	1.3[2]	$1.2(.42)\times10^{14}$
	$1_{10}-1_{01}$	8.24	4.08	
	$2_{21}-1_{10}$	4.53	26.33	
	$2_{11}-2_{02}$	3.89	2.00	
	$2_{20}-2_{11}$	1.53	2.71	

Notes to Table 6.3:

[1] Values in parentheses are 1 σ errors.

[2] Position offsets are in arc minutes relative to RA: $04^h38^m38^s$;

DEC: $25^\circ35'45''$.

[3] Values in brackets are the number of degrees of freedom

this repect. In Figure 6.11 optical depth contours from the uniform density model, which correspond to the values obtained for the 1_{10} - 1_{01} and 2_{12} - 1_{01} C_3H_2 lines as determined from the corresponding $C^{13}C_2H_2$ transitions, are overlaid on the $\tilde{\chi}^2$ contours for TMC-1 (0,0). The optical depth contours intersect the "valley" of minimum $\tilde{\chi}^2$ to constrain the column density to 5.7(±1.5) x10^{13} cm^{-2} and $n(H_2)$ to 3 - 4 x10^4 cm^{-3}. The spread in solutions includes the uncertainty in optical depths which rely on an assumed $^{12}C/^{13}C$ isotope ratio (see section 4.1.3). Parameters for this solution are listed in Table 6.4. For 5 of the transitions, the model fit is beyond the 1 sigma uncertainty of the observations (Figure 6.12).

An LVG model incorporating two density components (described in section 5.4.3) was calculated to determine if this configuration could more narrowly confine the the physical parameters. Similar values of X/(dv/dr) for the two components are assumed at first, leaving 3 parameters to solve for: molecular hydrogen density of the denser component n_1, and for the less dense component n_2, and one X/(dv/dr) for both components. The value of the best fit $\tilde{\chi}^2$, now with 7 degrees of freedom, is reduced to 1.6 compared to 2.5 from the uniform density case. The model and observations are compared in Figure 6.13 for the "best fit" 2 component solution for TMC-1 (0,0). This result leaves only 2 of the fitted points outside of the uncertainties. The parameters of this solution give n_1= 3.4x10^4 cm^{-3}, n_2 = 2.6x10^4 cm^{-3} and X/(dv/dr) = 1.5x10^{-9} pc s km^{-1}. These parameters result in a column density of 8.0(±3.9) x 10^{13} cm^{-2} for the denser component and a nearly similar column density of

Figure 6.11. $\tilde{\chi}^2$ contours for the uniform density model in TMC-1 intersected by optical depth contours. $\tilde{\chi}^2$ contours are described in Figure 6.9. The optical depth values for the $1_{10}-1_{01}$ (single dotted contour) and the $2_{12}-1_{01}$ C_3H_2 transitions (single dash-dot contour) are obtained from isotopic observations.

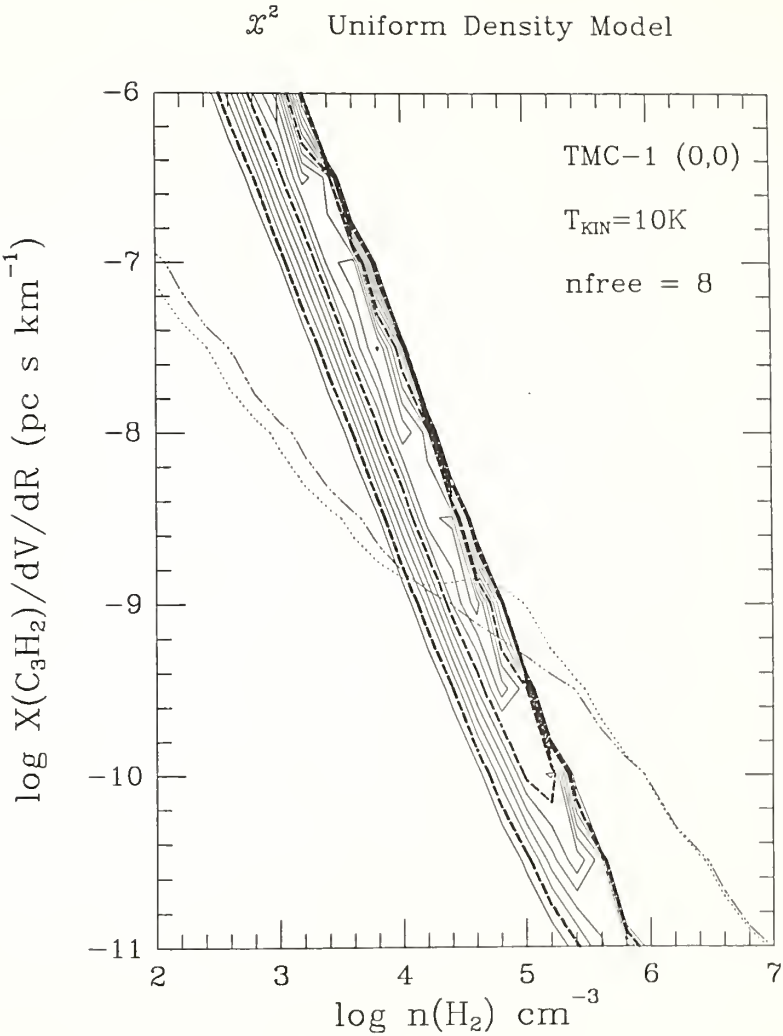
χ^2 Uniform Density Model
TMC−1 (0,0)
T_{KIN}=10K
nfree = 8
log $X(C_3H_2)/dV/dR$ (pc s km^{-1})
log $n(H_2)$ cm^{-3}
−6
−7
−8
−9
−10
−11
2
3
4
5
6
7

Table 6.4

Summary of Model Results for TMC-1(0,0) With Opacity Constraints

log n (cm^{-3})	log X/dv/dr ($pc\ s\ km^{-1}$)	$\tilde{\chi}^2[\nu]$	N (C_3H_2) (cm^{-2})
4.57(.22)	-8.98(.18)	4.0[10]	$5.9(1.3)\times10^{13}$

Transition	TEX(K)	τ
$1_{10}-1_{01}$	11.54	1.12
$2_{12}-1_{01}$	6.52	7.05
$2_{21}-1_{10}$	5.08	9.62
$3_{12}-3_{03}$	3.26	1.26
$3_{30}-2_{21}$	3.53	4.06
$1_{10}-0_{00}$	6.01	2.12
$2_{02}-1_{11}$	4.67	3.22
$2_{11}-2_{02}$	4.81	0.72
$2_{20}-2_{11}$	1.44	1.33
$3_{22}-3_{13}$	3.25	0.31

Notation is the same as for Table 6.3.

Figure 6.12 Comparison of model with observations for the uniform density model in TMC-1 (0,0) obtained with optical depth constraints. Brightness temperatures are indicated for the ortho lines (top) and para lines (bottom) as functions of E/k (K) above the respective ortho or para levels.
Each transition is indicated by frequency (GHz) above the data points. The fit parameters, $n(H_2)$ and X/(dv/dr) are indicated along with the $\tilde{\chi}^2$ value for the fit. Source coordinates are given in Table 6.2.

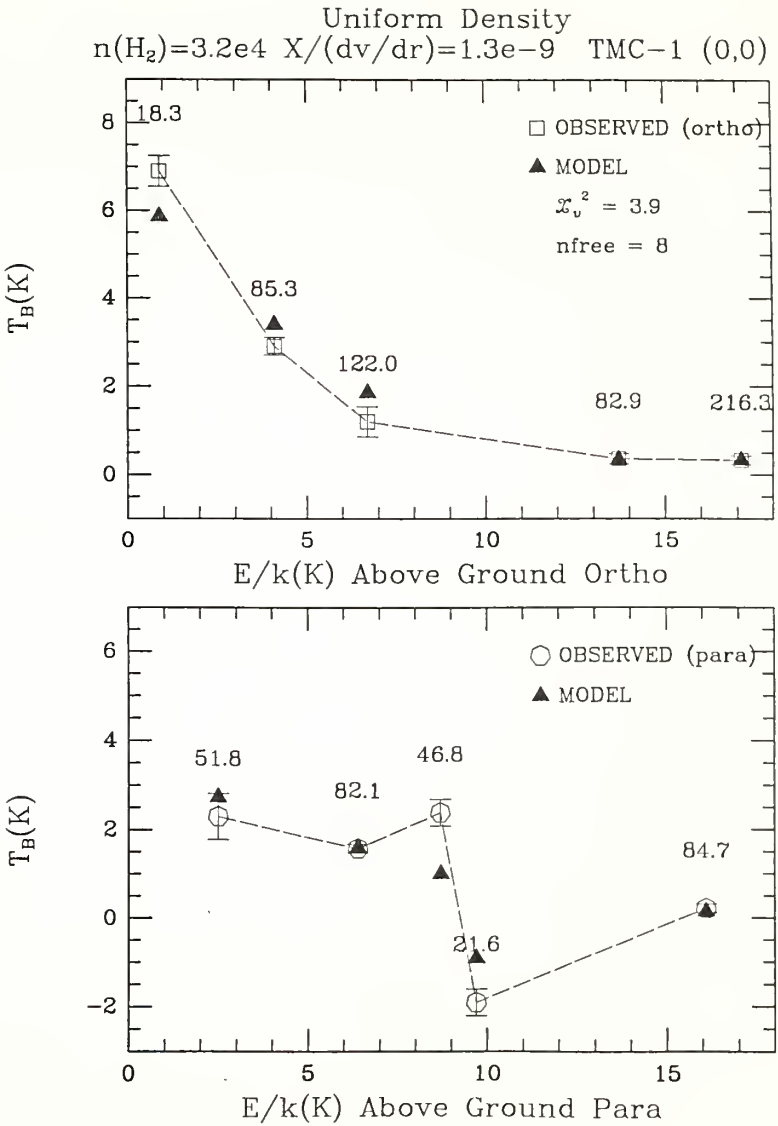
Uniform Density
n(H2)=3.2e4 X/(dv/dr)=1.3e-9 TMC-1 (0,0)
OBSERVED (ortho)
MODEL
χ_ν^2 = 3.9
nfree = 8
18.3
85.3
122.0
82.9
216.3
T_B(K)
E/k(K) Above Ground Ortho
OBSERVED (para)
MODEL
51.8
82.1
46.8
21.6
84.7
T_B(K)
E/k(K) Above Ground Para

Figure 6.13 Comparison of model with observations for the 2-component model in TMC-1 (0,0). Brightness temperatures are indicated for the ortho lines (top) and para lines (bottom) as functions of E/k (K) above the respective ortho or para levels. Each transition is indicated by frequency (GHz) above the data points. The fit parameters, $n(H_2)$ and X/(dv/dr) are indicated along with the $\tilde{\chi}^2$ value for the fit.

TMC−1 (0,0)

n(c)=3.4e4 n(h)=2.65e4 X/(dv/dr)=1.5e−9

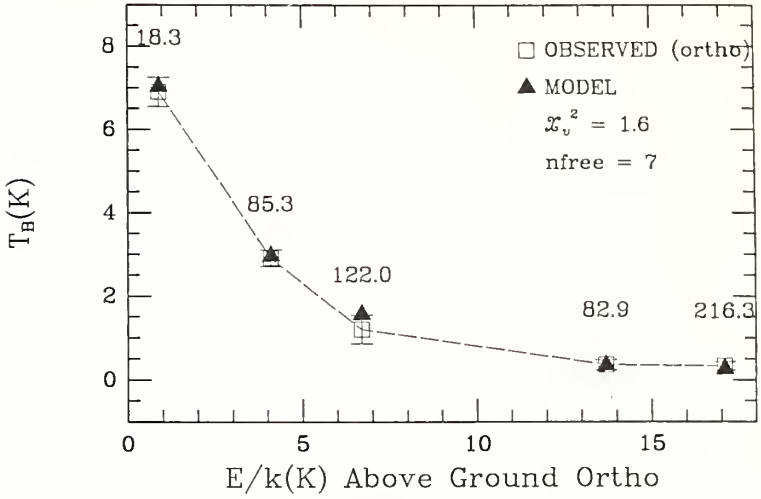

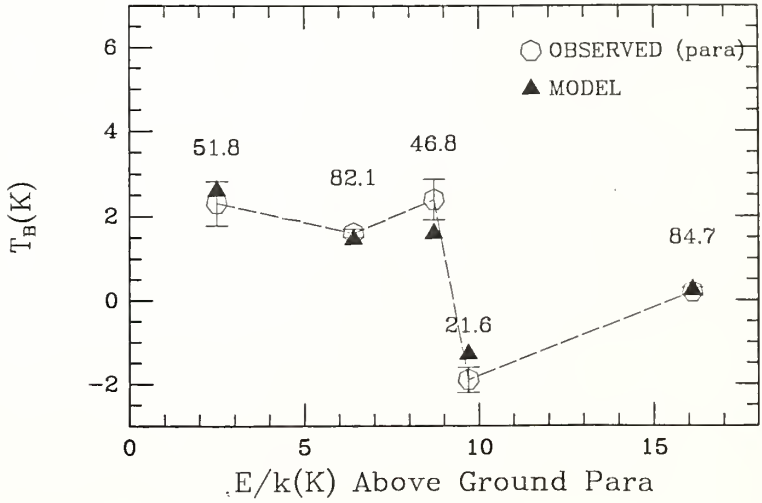

$6.2(\pm 3.0)\times 10^{13}$ cm^{-3} for the less dense component. This is a total column density through both cloud components of 1.4×10^{14} cm^{-2}, consistent with the values of 1 to 3×10^{14} cm^{-2} reported from isotopic observations in Madden *et al.* (1986) and Bell *et al.* (1988) but inconsistent with optical depths derived from these observations. Although the model converges to a solution with two components of similar densities, the results are not consistent with the uniform density model discussed above. A different mechanism is occuring in the 2-component model, as more possibilities are present for absorption in the 21 GHz transition with the additional component. This is illustrated by the 2-component transfer in equation 5.28. Referring to the contours of $\tilde{\chi}^2$ for the uniform density model (Figure 6.8), we can see that this "2 component" solution seems to lie in the vicinity of the second minimum discussed above. The fit parameters for this 2-component solution are given in Table 6.5. Since n_1 and n_2 are similar, excitation temperatures and opacities do not contrast greatly in the two components.

We also explored the case of 2-components with 4 variables, now allowing X/(dv/dr) to vary independently in each of the components, resulting in 6 degrees of freedom. This model converges to a solution having identical X/(dv/dr) values in the 2 components, which is the same value as that determined by the 2-component model with 3 parameters. The new model does not succeeed in lowering $\tilde{\chi}^2$, so that there is no evidence for different core and halo abundances of C_3H_2 at this position in TMC-1.

Table 6.5

Summary of Model Results for TMC-1 (2 Component Model)

Position (ΔRA,ΔDEC)	$\log n_1$ (cm^{-3})	$\log n_2$ (cm^{-3})	log X/dv/dr ($pc\ s\ km^{-1}$)	$\tilde{\chi}^2[\nu]$	N_1 (10^{13} cm^{-2})	N_2 (10^{13} cm^{-2})
(0,0)	4.53(.13)	4.42(.13)	-8.83(.25)	1.6[7]	8.0(2.4)	6.2(1.9)

Transition	T_{ex_1}(K)	τ_1	T_{ex_2}(K)	τ_2
$1_{10}-1_{01}$	11.6	1.46	9.57	1.48
$2_{12}-1_{01}$	6.87	8.96	6.00	8.40
$2_{21}-1_{10}$	5.33	12.49	4.71	11.19
$3_{12}-3_{03}$	3.41	1.90	3.14	1.40
$3_{30}-2_{21}$	3.67	6.04	3.40	4.48
$1_{11}-0_{00}$	6.31	2.65	5.43	2.63
$2_{02}-1_{11}$	4.88	4.21	4.40	3.74
$2_{11}-2_{02}$	4.81	1.04	4.47	0.84
$2_{20}-2_{11}$	1.51	1.87	1.46	1.44
$3_{22}-3_{13}$	3.28	0.51	3.16	0.35

(-4,6)	4.23(.35)	4.05(.23)	-8.30(2)	0.6[4]	11.3(.35)	8.4(2.0)

$1_{10}-1_{01}$	10.07	2.93	7.53	2.97
$2_{12}-1_{01}$	6.62	16.28	5.35	14.55
$2_{21}-1_{10}$	5.10	12.44	4.25	18.46
$1_{11}-0_{00}$	5.88	5.08	4.73	4.90
$2_{02}-1_{11}$	4.72	7.59	4.02	6.19
$2_{11}-2_{02}$	4.32	1.93	3.84	1.36
$2_{20}-2_{11}$	1.53	3.08	1.57	1.99

Table 6.5

(continued)

Position[2] (ΔRA,ΔDEC)	log n_1[3] (cm^{-3})	log n_2 (cm^{-3})	log X/dv/dr ($pc\ s\ km^{-1}$)	$\tilde{\chi}^2[\nu]$	N_1 (10^{14} cm^{-2})	N_2
(2,-3)	4.56(.17)	4.16(.16)	-8.72(.14)	1.8[1]	9.5(2.8)	3.8(1.1)
	Transition	TEX_1(K)	τ_1	TEX_2(K)	τ_2	
	$1_{10}-1_{01}$	12.86	1.71	6.51	1.76	
	$2_{21}-1_{10}$	5.86	15.40	3.85	9.86	
	$2_{11}-2_{02}$	5.01	1.40	3.83	0.63	
	$2_{20}-2_{11}$	1.60	2.52	1.55	0.86	
(-2,3)	4.43(.23)	4.19(.20)	-8.54(.12)	0.9[1]	11.(.34)	6.2(1.9)
	$1_{10}-1_{01}$	11.65	2.07	7.74	2.16	
	$2_{21}-1_{10}$	5.54	17.29	4.28	13.49	
	$2_{11}-2_{02}$	4.71	1.49	3.98	0.92	
	$2_{20}-2_{11}$	1.53	2.57	1.48	1.32	

Notates to Table 6.5:

[1] Values in parentheses are 1 σ errors.

[2] Position offsets are in arc minutes relative to RA: $04^h38^m38^s$; DEC: $25^\circ35'45''$.

[3] The higher and lower density components are denotes n_1 and n_2, respectively.

The position of the NH_3 peak in TMC-1 (offset from the (0,0) position by 4' west and 6' north) was also analyzed, since the possible chemical differences between this position and the cyanopolyyne peak are of interest. A composite of 4 para lines and 3 ortho lines is shown in Figure 6.14, and observed line parameters are described in Table 6.2. The search routine determined the best fit for the uniform density model to be $n(H_2) = 8.9\times10^3$ cm^{-3} and $X/(dv/dr) = 9.8\times10^{-9}$ pc s km^{-1}, which gives $\tilde{\chi}^2 = 0.97$, and we conclude that the model provides an acceptable interpretation of the data. In this uniform density model the number of free parameters is 5, and virtually all of the calculated intensities fall within the uncertainties of the data (Figure 6.15). A column density of $1.3(\pm0.3)\times10^{14}$ cm^{-2} for this position is approximately a factor of 2 smaller than that of the (0,0) position as determined from the uniform density solution.

The 2 component model with 3 free parameters and 4 degrees of freedom gives a best fit of $\tilde{\chi}^2 = 0.6$ at the TMC-1 NH_3 peak. Such a low $\tilde{\chi}^2$ implies that there is a large probability that the discrepancies between the model predictions and observations are likely to be due to random fluctuations. The parameters for this solution are $n_1 = 1.7\times10^4$ cm^{-3}, $n_2 = 1.1\times10^4$ cm^{-3}, and $X/(dv/dr) = 5\times10^{-9}$ pc s km^{-1} resulting in $N(C_3H_2) = 12.5\times10^{13}$ and 8.3×10^{13} cm^{-2} for the 2 regions (i.e., total column density = 2.1×10^{14} cm^{-2}). Such values are about 50% greater than the column densities for the (0,0) position using this model. The parameters determined for this solution are listed in Table 6.5.

Figure 6.14 Observed C_3H_2 spectra in TMC-1(-4,6). For each of the ortho (right column) and para (left column) profiles the transition, frequency and energy above the ground state (K) are indicated. Table 6.1 contains the telescope parameters for the observations and Table 6.2 contains source coordinates.

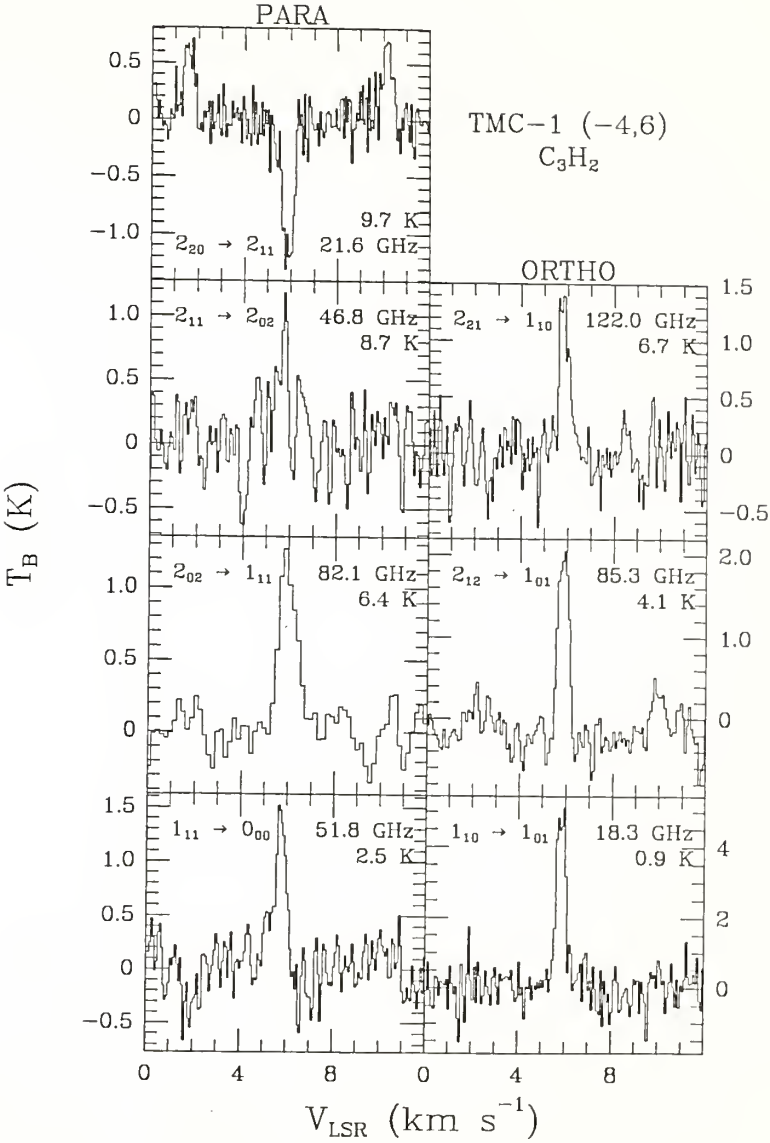
PARA
ORTHO
TMC−1 (−4,6)
C_3H_2
$2_{20} \rightarrow 2_{11}$ 9.7 K 21.6 GHz
$2_{11} \rightarrow 2_{02}$ 46.8 GHz 8.7 K
$2_{21} \rightarrow 1_{10}$ 122.0 GHz 6.7 K
$2_{02} \rightarrow 1_{11}$ 82.1 GHz 6.4 K
$2_{12} \rightarrow 1_{01}$ 85.3 GHz 4.1 K
$1_{11} \rightarrow 0_{00}$ 51.8 GHz 2.5 K
$1_{10} \rightarrow 1_{01}$ 18.3 GHz 0.9 K
T_B (K)
V_{LSR} (km s^{-1})

Figure 6.15 Comparison of the uniform density model results and observations for TMC-1(-4,6). Description is the same as that for Figure 6.12.

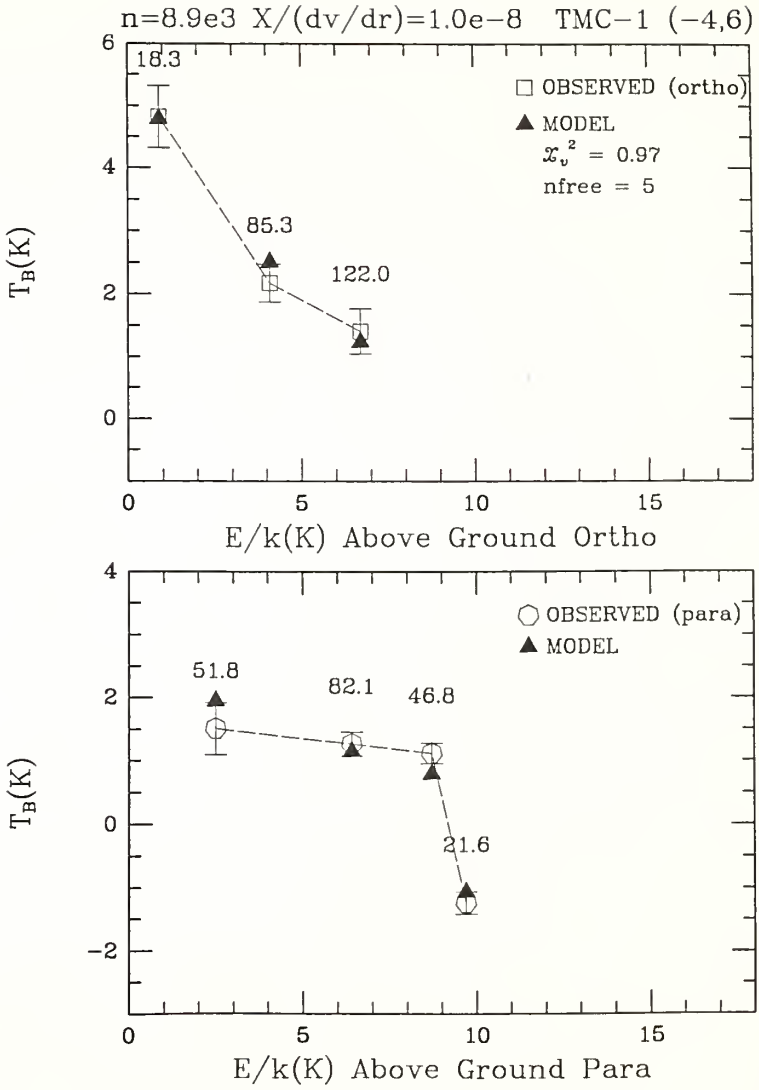
n=8.9e3 X/(dv/dr)=1.0e−8 TMC−1 (−4,6)
OBSERVED (ortho)
MODEL
χ_ν^2 = 0.97
nfree = 5
18.3
85.3
122.0
T_B(K)
E/k(K) Above Ground Ortho
OBSERVED (para)
MODEL
51.8
82.1
46.8
21.6
T_B(K)
E/k(K) Above Ground Para

For 2 other points along the ridge we have observed 4 C_3H_2 transitions and find that the 2 component model improves the $\tilde{\chi}^2$ value for the (2,-3) position and the uniform density model adequately describes the observations from the (-2,3) position. Tables 6.3 and 6.5 describe the model results.

6.2.3 Summary

We conclude that the overall sensitivity of the intensity of these particular transitions to density and abundance is limited. We notice, however, that by incorporating optical depth information derived from isotopic observations, the abundance and density can be well constrained with the uniform density model. For the (0,0) position in TMC-1, the column density is determined to be 5.7(±1.5) $\times 10^{13}$ cm^{-2} and $n(H_2)$ is 3 to 4 $\times 10^4$ cm^{-3}, lying within the "valley" of minimum $\tilde{\chi}^2$ contours. This results in a fractional abundance of C_3H_2 relative to H_2 of 5.7×10^{-9}, assuming $N(H_2) \sim 10^{22}$ cm^{-2} (Irvine, Goldsmith, and Hjalmarson 1987). Without this constraint, we can only specify a wide range of acceptable parameters: $n(H_2) = 2\times 10^3$ to 4×10^4 cm^{-3} and $N(C_3H_2) = 3.7\times 10^{13}$ to 3.0×10^{14} cm^{-2}. Column densities estimated from C_3H_2 isotopic data and assuming LTE conditions (Madden *et al.* 1986; Bell *et al.* 1988) result in overestimating column densities by approximately 100%. In TMC-1, we have isotopic C_3H_2 observations only at the (0,0) position, and therefore are not able to properly constrain the solutions for the other positions.

The 21 GHz transition provides a particularly difficult challenge to model, in that the depth of absorption is underpredicted in these models. To attempt to decrease this discrepancy, the model strives to converge to a minimum $\tilde{\chi}^2$ at the limiting maximum absorption region, which is at low densities and high column densities. This is evident in Figure 6.16, which displays contours of constant brightness temperature values corresponding to the TMC-1 observations. Notice the region delineated by the 21 GHz transition. The 21 GHz contour represented in the figure is the greatest depth of absorption that the model calculates for this transition; the observed value exceeds that of the model and needs a deeper absorption to be properly fitted. Optical depths for the 18 and 85 GHz transitions derived from the optimum $\tilde{\chi}^2$ solutions (without considering the isotopic species), therefore, are high with respect to those estimated with the previously obtained ^{13}C-substituted C_3H_2 observations (Madden *et al.* 1986; Bell *et al.* 1988). Predicted values for the 21 GHz transition are particularly sensitive to the collision rates. We are calculating (T_{EX} - T_{BG}) which, in this case, is a *small* value critically dependent upon the comparative rate of populating the 2_{20} and 2_{11} levels.

In the 2-component model, the 2_{20} - 2_{11} transition is absorbed again in the less dense component, thereby permitting interaction between the two components, while the single component model strictly obeys the rules governing the LVG approximation. The two component model *does* improve the 21 GHz predictions somewhat, but not

Figure 6.16a,b Lines of constant brightness temperatures in TMC-1 (0,0). Para (a) and ortho (b) contours are the uniform density model results which correspond to the observed values. The para 21.6 GHz contour (long dashes) is the limiting depth in absorption that the model calculates and is underpredicted with respect to the observations.

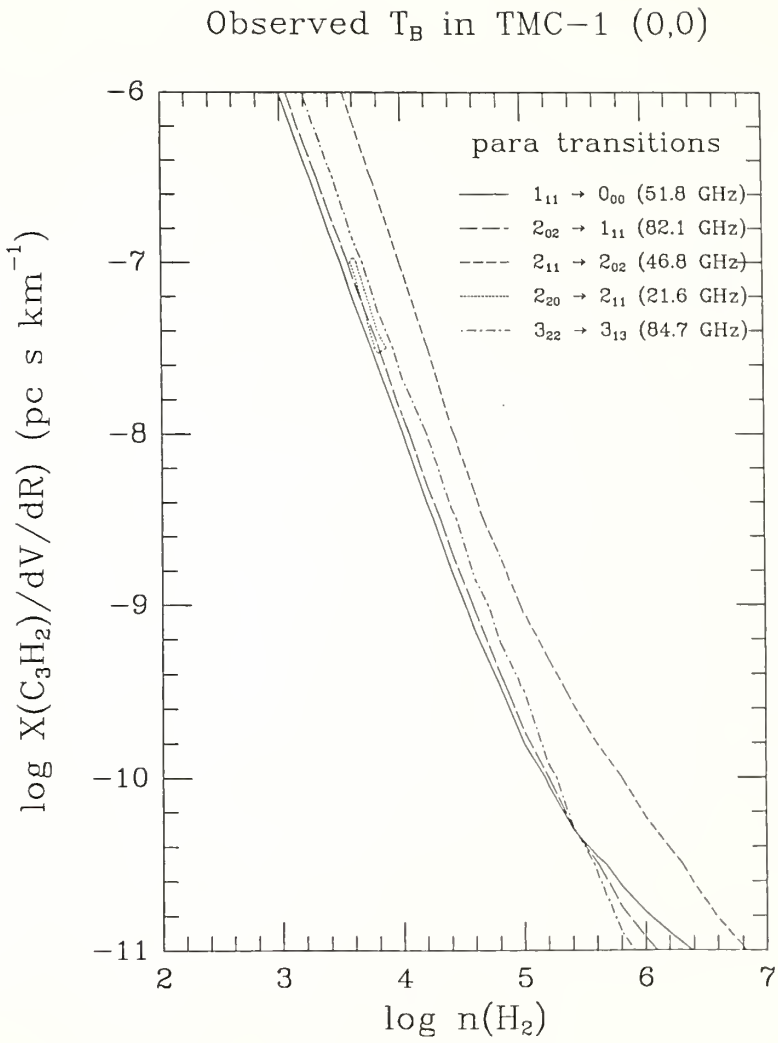
Observed T_B in TMC−1 (0,0)
para transitions
$1_{11} \rightarrow 0_{00}$ (51.8 GHz)
$2_{02} \rightarrow 1_{11}$ (82.1 GHz)
$2_{11} \rightarrow 2_{02}$ (46.8 GHz)
$2_{20} \rightarrow 2_{11}$ (21.6 GHz)
$3_{22} \rightarrow 3_{13}$ (84.7 GHz)
log $X(C_3H_2)/dV/dR)$ (pc s km^{-1})
log $n(H_2)$
−6
−7
−8
−9
−10
−11
2
3
4
5
6
7

(a)

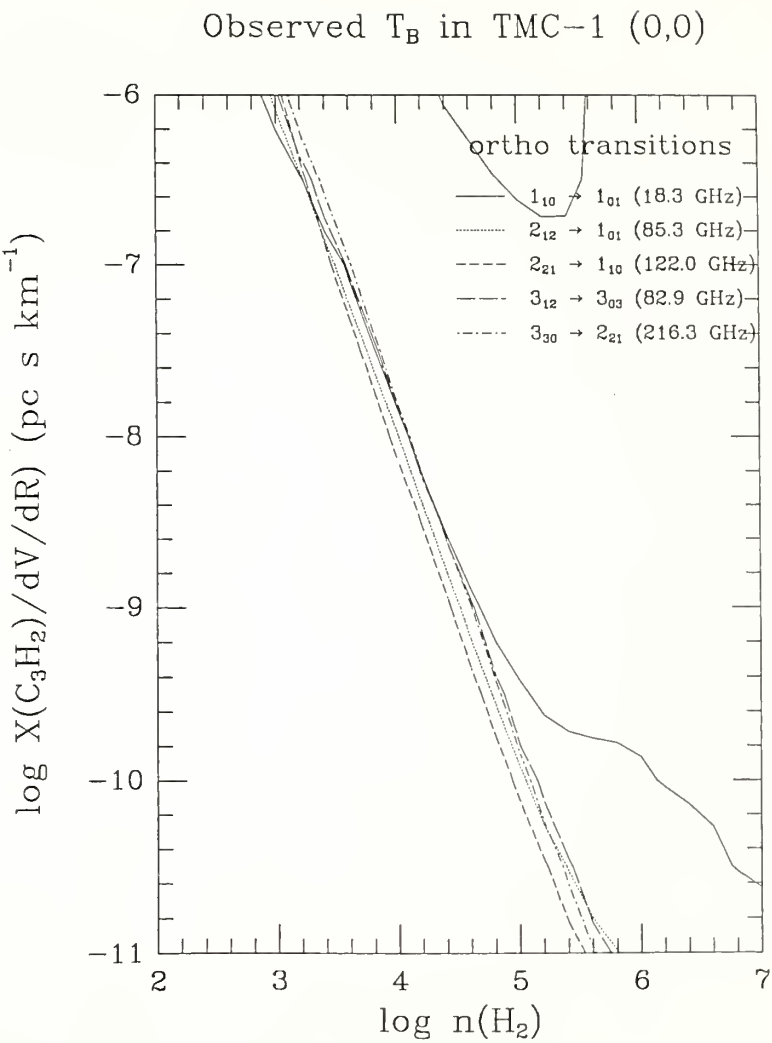
Observed T_B in TMC-1 (0,0)
ortho transitions
$1_{10} \rightarrow 1_{01}$ (18.3 GHz)
$2_{12} \rightarrow 1_{01}$ (85.3 GHz)
$2_{21} \rightarrow 1_{10}$ (122.0 GHz)
$3_{12} \rightarrow 3_{03}$ (82.9 GHz)
$3_{30} \rightarrow 2_{21}$ (216.3 GHz)
log $X(C_3H_2)/dV/dR)$ (pc s km^{-1})
log $n(H_2)$
-6
-7
-8
-9
-10
-11
2
3
4
5
6
7

(b)

remarkably. Consequently, the trend for the 2-component model is to drive the solutions to a higher density, lower abundance region.

From these results it is difficult to present a general view of the C_3H_2 abundance and density distribution in several positions along the ridge in TMC-1. Without optical depth constraints at the other positions, the range of column densities and $n(H_2)$ determined by the uniform density model is too broad. It would be interesting to be able to confine the parameters better, since the variation of abundance and $n(H_2)$ in TMC-1 has been a topic of debate. Bujarrabal *et al.* (1981) find that the abundance of the carbon chain molecules relative to other molecules (NH_3, HCO^+, and CS) does not vary significantly along the ridge and that variations in H_2 density by a factor of 3 account for the variation in observed line intensities. Conclusions drawn by Olano, Walmsley and Wilson (1988), however, are that large abundance gradients are present within TMC-1 in addition to density gradients.

For the 2-component model C_3H_2 does not show very contrasting density components in TMC-1 and, within the uncertainty estimates, the density remains relatively constant along the ridge with a mean value for the denser component being 2.9×10^4 cm^{-3} while that for the less dense component is 1.7×10^4 cm^{-3}. C_3H_2 column densities are larger in the higher density component, ranging from 8.0×10^{13} to 1.3×10^{14} cm^{-3}, while the less dense component shows column density variations of 3.8 to $8.4\times10^{13}cm^{-2}$. These results are consistent with a *total* C_3H_2 column density which remains constant ($\sim1.5\times10^{14}$) along the ridge. The estimates from the 2-component model fall within the

"valley" of lowest $\tilde{\chi}^2$ region seen in the uniform density $\tilde{\chi}^2$ contour plots (Figures 6.9), but give consistently larger column density estimates than the uniform density model results constrained by optical depths.

Whether TMC-1 is better modeled with a uniform density configuration or a multi-component model has been a topic of discussion for other molecular emission. Bujarrabal *et al.* (1981) and Avery *et al.* (1982) argue that the densities derived from observations of HC_5N and HC_3N are not consistent with a single density model and require a multi-component configuration. On the other hand, Schloerb, Snell and Young (1983) favor a model such that the density is uniform at a value of $5\text{-}10\times10^4$ cm^{-3} but the model does not explain one particularly deviant transition of HC_3N. Within the limitations of our models, a multi-component model is not very convincing.

Due to the uncertainties and ambiguities of the results, we conclude that the observations are consistent with a uniform (or nearly uniform) density model in TMC-1. Variations along the ridge do not appear to be particularly striking in either $n(H_2)$ or C_3H_2 column density. Such a model can constrain the molecular hydrogen density and C_3H_2 column density well in TMC-1 if additional constraints are provided from optical depth measurements determined from isotopic observations. The model *qualitatively* predicts all of the transitions well, including the 21 GHz absorption line, but underpredicts the depth of absorption.

6.3 L1498

6.3.1 Observations and Model Results

L1498 also proved to be a source rich in C_3H_2, as shown in Figure 6.17. Four para and 3 ortho transitions were observed, ranging in energy above the ground level from 1 to 14 K. The 2_{20}-2_{11} 21 GHz transition is seen in absorption, as in all dark clouds and giant molecular clouds observed to date. The line widths seen in L1498 are the narrowest seen in dark clouds, near the thermal width of the 10 K source. Table 6.6 summarizes the observed line parameters. Integrated intensity and brightness temperature contour maps in the 2_{12}-1_{01} 85 GHz transition made at FCRAO in full beam width spacing (Figure 6.18) reveal a well defined source 2.5′x 3.5′ in half intensity size, with a peak 54" east and slightly south of the reference position (source coordinates given in Table 6.6).

Seven C_3H_2 lines were analyzed with the uniform density model using 5 degrees of freedom. Reduced chi-squared contours over the $n(H_2)$, X/(dv/dr) plane are shown in Figure 6.19. A valley in the contours, as for TMC-1, can be seen ranging in density from 1.0×10^3 to 1.6×10^4 cm^{-3} with a spread of over 2 orders of magnitudes in X/(dv/dr) values. This corresponds to column density values ranging from 1.4×10^{13} to 2.2×10^{14} cm^{-2}. When the optical depth of the 1_{10} - 1_{01} C_3H_2 line as determined from the corresponding $C^{13}C_2H_2$ transition is also included in determining the solution, a higher molecular hydrogen density and lower abundance are implied. The resulting

Figure 6.17 Observed C_3H_2 spectra in L1498. Description is the same as that for Figure 6.14. Table 6.6 contains source coordinates.

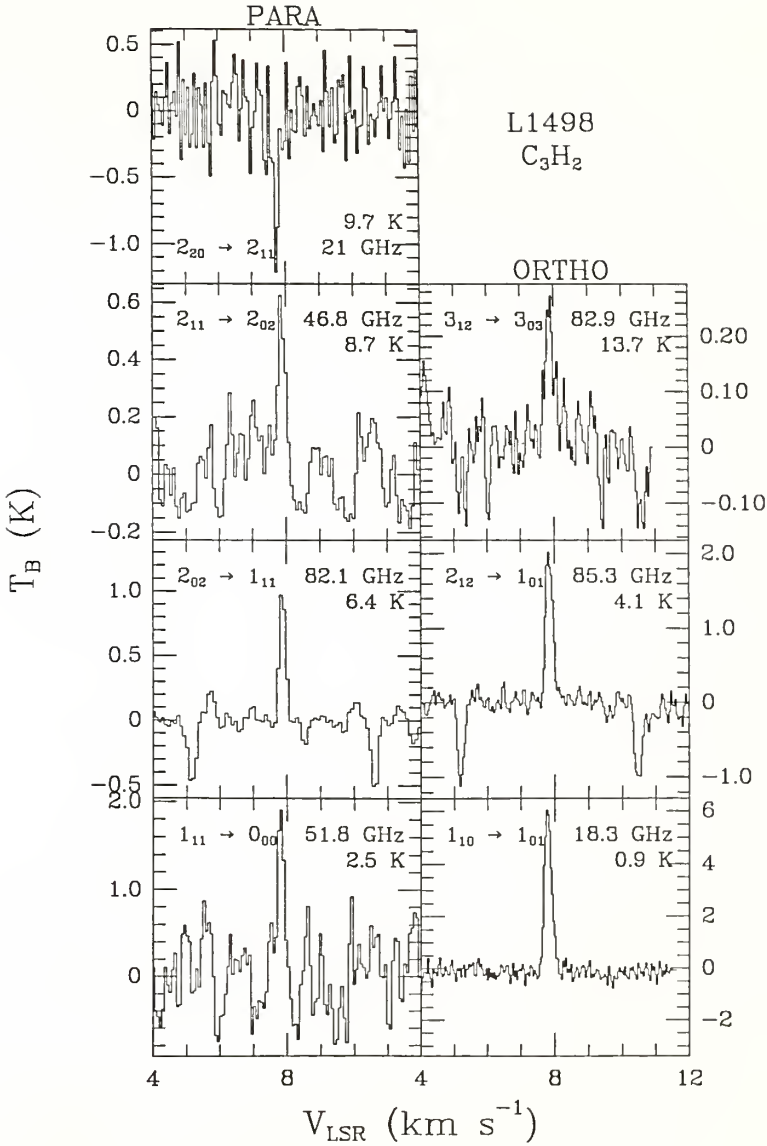
PARA
ORTHO
L1498
C_3H_2
$2_{20} \rightarrow 2_{11}$ 9.7 K 21 GHz
$2_{11} \rightarrow 2_{02}$ 46.8 GHz 8.7 K
$3_{12} \rightarrow 3_{03}$ 82.9 GHz 13.7 K
$2_{02} \rightarrow 1_{11}$ 82.1 GHz 6.4 K
$2_{12} \rightarrow 1_{01}$ 85.3 GHz 4.1 K
$1_{11} \rightarrow 0_{00}$ 51.8 GHz 2.5 K
$1_{10} \rightarrow 1_{01}$ 18.3 GHz 0.9 K
T_B (K)
V_{LSR} (km s^{-1})

Table 6.6

Summmary of L1498 C_3H_2 Observations

Position (RA/DEC)	Transition	Frequency (GHz)	T_B (K)	σ (K)	V_{LSR}	ΔV	resol
					.....(km s^{-1})....		
$04^h07^m50^s$	$1_{10}-1_{01}$	18.3	6.10	0.22	7.76	0.25	0.04
$25^\circ02'13''$	$2_{12}-1_{01}$	85.3	1.9	0.11	7.82	0.26	0.04
	$3_{12}-3_{03}$	82.9	0.27	0.10	7.91	0.29	0.05
	$1_{11}-0_{00}$	51.8	1.75	0.36	7.83	0.25	0.07
	$2_{02}-1_{11}$	82.1	1.0	0.10	7.84	0.23	0.09
	$2_{11}-2_{02}$	46.8	0.62	0.12	7.84	0.27	0.08
	$2_{20}-2_{11}$	21.6	-1.1	0.24	7.73	0.21	0.07

Notation is the same as for Table 6.2.

Figure 6.18 Integrated intensity (YINT) and antenna temperature (YMAX) contours for L1498. Observations are from the 14 m FCRAO telescope. YINT contours range from 0.0 to 0.45 K km s^{-1} in steps of 0.05 K. Ymax contour values range from 0.0 to 1.0 K in steps of 0.2 K. DALP and DDEC are offsets of RA and DEC, respectively, in arc minutes with respect to the source coordinates in Table 6.6.

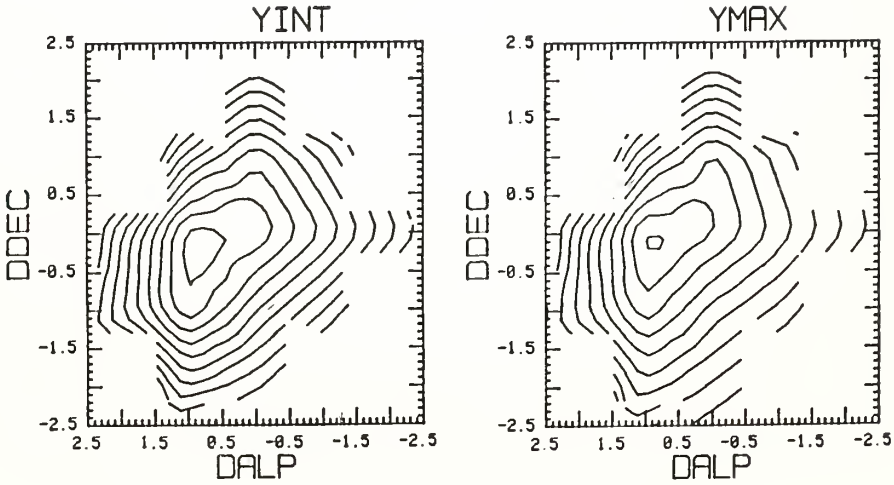
YINT
YMAX
DDEC
DALP
2.5
1.5
0.5
-0.5
-1.5
-2.5

Figure 6.19. $\tilde{\chi}^2$ contours for the uniform density model in L1498 intersected by an optical depth contour. $\tilde{\chi}^2$ contours are 3.0 to 30.0 in steps of 2.7 K. Levels 13.8 and 27.3 K are represented by dashed contours with increasing thickness. The optical depth value for the $1_{10}-1_{01}$ (single dotted contour) C_3H_2 transition is obtained from isotopic observations.

χ^2 Uniform Density Model

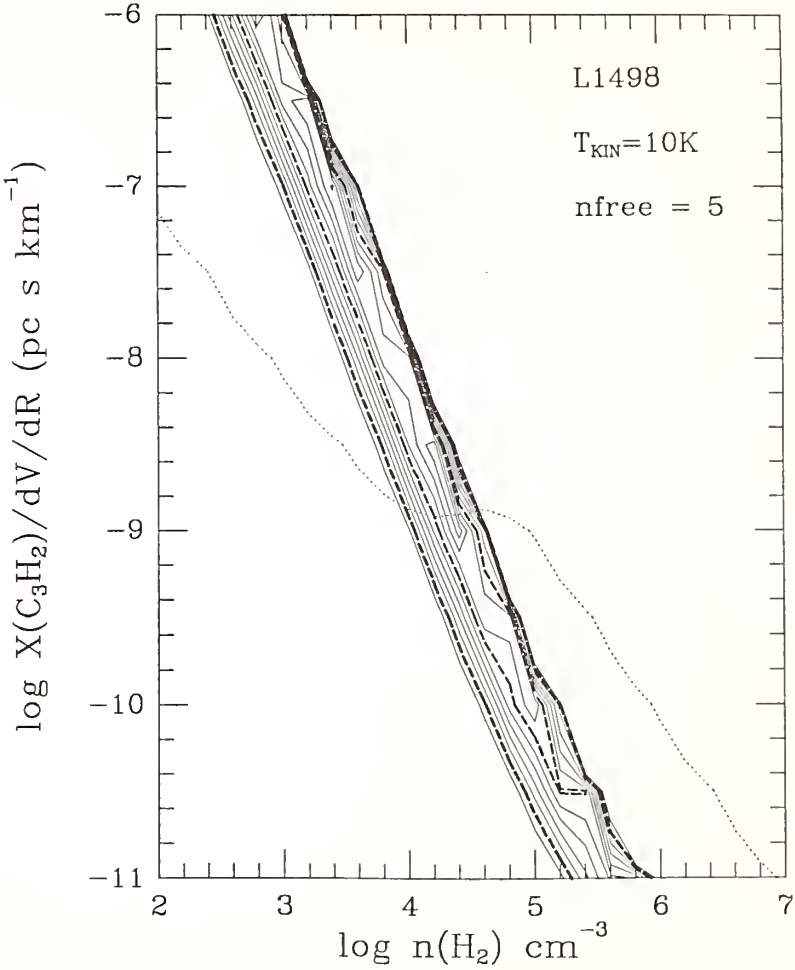

$n(H_2)$, 2.6×10^4 cm^{-3}, is almost an order of magnitude higher than the best solution without matching the optical depth. Table 6.7 lists the model results. For these parameters, the predicted intensities are consistent with the 7 observed lines within one standard deviation with the exception of the 85 GHz line and possibly the 18 GHz transition (Figure 6.20). The column density derived from these parameters is $2.1(\pm1.1)\times10^{13}$ cm^{-2} assuming a velocity width if 0.25 km s^{-1}, a factor of 3 smaller than the value deduced by Bell *et al.* (1988). The fractional abundance of C_3H_2 relative to H_2 is ~ 2×10^{-9}. The 46 and 21 GHz data points, which are misfitted in the TMC-1(0,0) model results, are acceptably predicted in this case, but the 18 GHz line is not.

6.3.2 Summary

The uniform density model fitted the observations well, and it is not necessary to invoke a multi-component configuration in this case. As in the case of TMC-1, we have used the optical depth information determined from the observations of the $1_{10} - 1_{01}$ $C^{13}C_2H_2$ transition to constrain the solution. The column density and molecular hydrogen density are found to be $2.1(\pm1.6)\times10^{13}$ cm^{-2} and $2.6(1.0)\times10^4$ cm^{-3}, respectively, similar in $n(H_2)$ to TMC-1 but smaller in column density by a factor of 3. The solutions are listed in Table 6.7. Two of the model predictions for the lower energy ortho lines fall beyond the 1 sigma uncertainty level, but not by more than than 2 sigma. This model gives a column density esitmate

Table 6.7

Summary of Model Results for L1498 (Uniform Density)[1]

log n (cm^{-3})	log X/dv/dr (pc s km^{-1})	$\tilde{\chi}^2[\nu]$[2]	N (C_3H_2) (cm^{-2})
4.12(.28)	-8.96(.18)	3.7[5]	$2.1(1.5)\times10^{13}$

Transition	TEX(K)	τ
$1_{10}-1_{01}$	8.54	1.22
$2_{12}-1_{01}$	5.42	6.62
$3_{12}-3_{03}$	4.32	8.42
$1_{10}-0_{00}$	4.94	2.13
$2_{02}-1_{11}$	4.11	2.76
$2_{11}-2_{02}$	4.35	0.55
$2_{20}-3_{13}$	1.43	0.92

Notes to Table 6.7:

[1] Values in parentheses are 1σ errors.

Results are constrained by isotopic observations.

[2] Value in brackets is the number of degrees of freedom.

Figure 6.20 Comparison with the uniform density model results and observations in L1498. Descriptions are the same as Figure 6.12. Source coordinates are in Table 6.6.

Uniform Density Model

n=2.6e4 X/(dv/dr)=1.1e−9 L1498

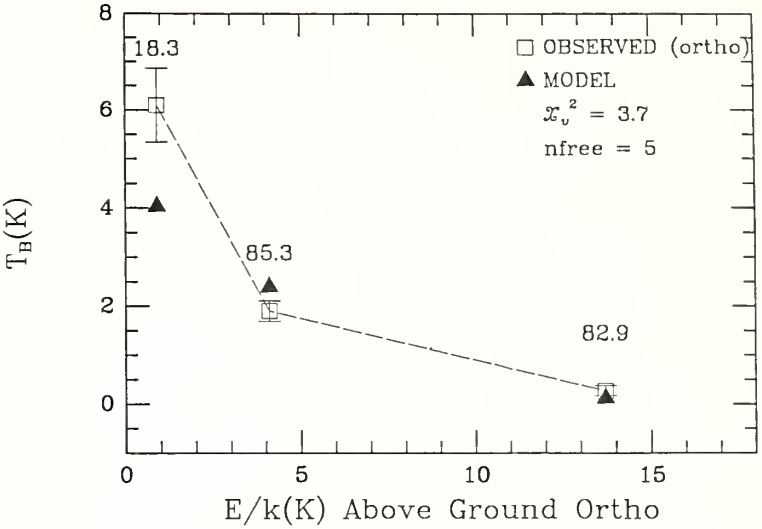

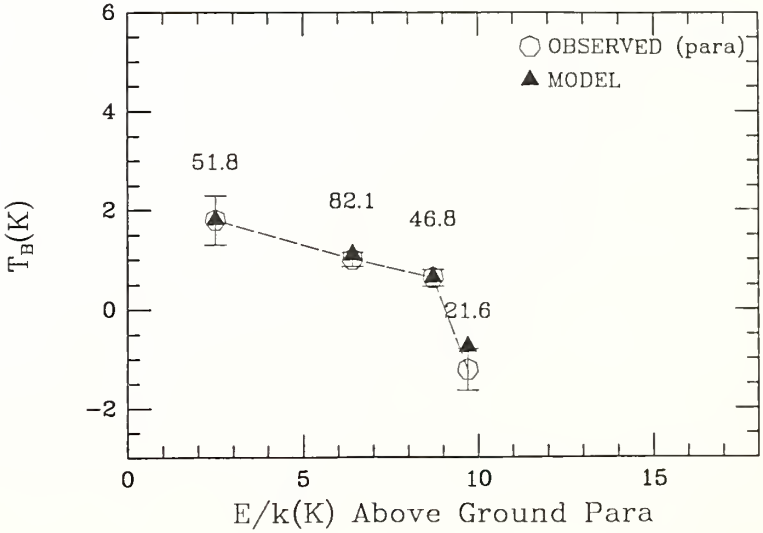

of 2.1×10^{13} cm^{-2}, smaller than the value of 6×10^{13} cm^{-2} derived using the isotopic data and assuming LTE conditions by Bell *et al.* (1988).

6.4 L134N

6.4.1 Observations and Model Results

L134N is a dark cloud well studied at radio wavelengths and is known to be a rich source of molecular emission and to be void of internal energy sources. From a recent intensive molecular study of this region (Swade 1989a), a high density core with an $n(H_2)$ of 3×10^4 cm^{-3} is seen in maps of NH_3, $H^{13}CO^+$ and other hydrocarbons, similar to the density determined by Snell (1981) using formaldehyde. Surrounding this core region, $C^{18}O$ is excited in gas with an order of magnitude lower density. The C_3H_2 distribution in L134N is similar to that of ammonia, with a half intensity width of 5.1 arc minutes (Swade 1989a; Swade 1989b).

The 4 para and 3 ortho C_3H_2 lines observed toward the peak C_3H_2 position are presented in Figure 6.21. These lines cover a range of energy above the ground state from 0.9 to 9.7 K and do not cover the highest range in energy observed, for example, in TMC-1. Observational parameters for the 7 transitions are listed in Table 6.8. The lines are generally narrow, with a mean velocity width of 0.29 km s^{-1} (standard deviation = 0.07 km s^{-1}). Except for the 85 GHz and 46 GHz transitions, all of the lines were observed with a velocity resolution of about 0.08 km s^{-1}. The exceptions were

Figure 6.21 Observed C_3H_2 transitions in L134N. Descriptions are the same as Figure 6.14. Source coordinates are given in Table 6.8.

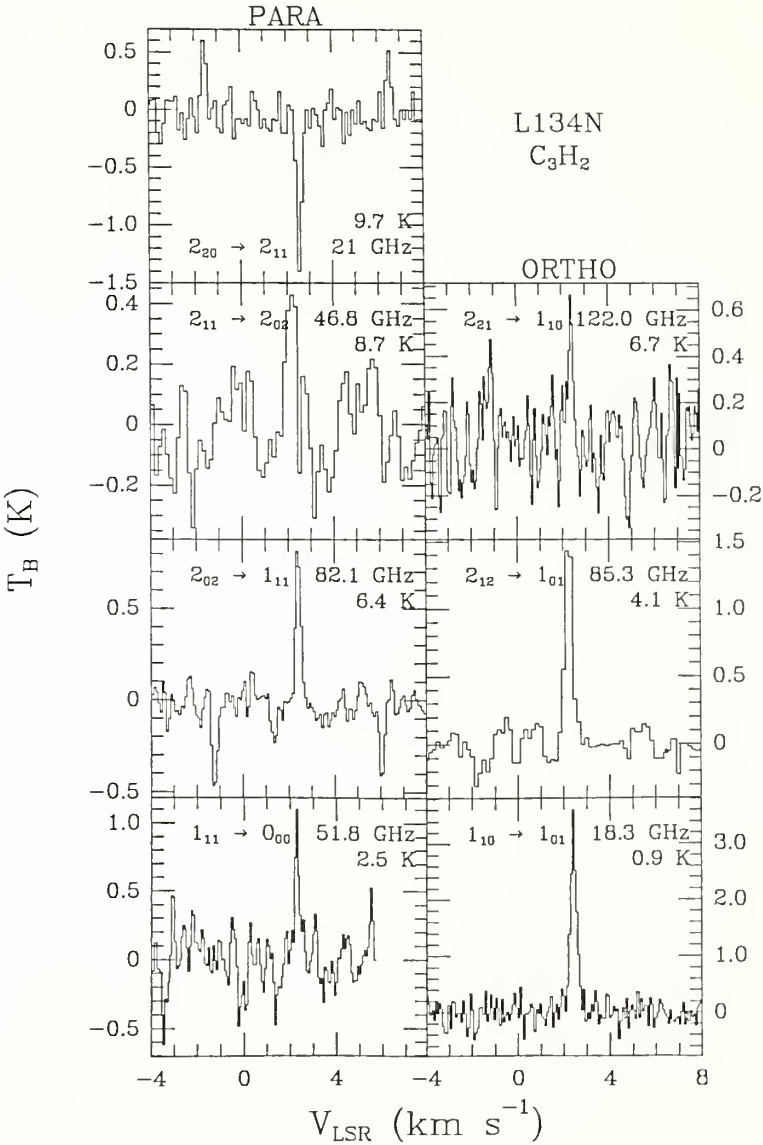
PARA
ORTHO
L134N
C_3H_2
$2_{20} \rightarrow 2_{11}$ 21 GHz 9.7 K
$2_{11} \rightarrow 2_{02}$ 46.8 GHz 8.7 K
$2_{21} \rightarrow 1_{10}$ 122.0 GHz 6.7 K
$2_{02} \rightarrow 1_{11}$ 82.1 GHz 6.4 K
$2_{12} \rightarrow 1_{01}$ 85.3 GHz 4.1 K
$1_{11} \rightarrow 0_{00}$ 51.8 GHz 2.5 K
$1_{10} \rightarrow 1_{01}$ 18.3 GHz 0.9 K
T_B (K)
V_{LSR} (km s^{-1})

Table 6.8

Summary of L134N C_3H_2 Observations

Position (ra/dec)	Transition	Frequency (GHz)	T_B (K)	σ (K)	V_{LSR}	ΔV	resol
					.....(km s^{-1}).....		
$15^h51^m32^s.4$	$1_{10}-1_{01}$	18.3	3.61	0.20	2.40	0.27	0.09
$-02°40'30''$	$2_{12}-1_{01}$	85.3	1.44	0.15	2.28	0.41	0.17
	$2_{21}-1_{10}$	122.0	0.66	0.16	2.39	0.28	0.06
	$1_{11}-0_{00}$	51.8	1.01	0.20	2.33	0.25	0.07
	$2_{02}-1_{11}$	82.1	0.82	0.07	2.37	0.22	0.09
	$2_{11}-2_{02}$	46.8	0.43	0.13	2.19	0.36	0.16
	$2_{20}-2_{11}$	21.6	-1.4	0.17	2.42	0.23	0.08

Notation is the same as for Table 6.2.

observed at half the resolution of the others, and the velocity widths for these lie at the higher extreme and thus they may be underesolved. Limited mapping was carried out in the $2_{12}-1_{01}$ and $1_{10}-1_{01}$ transitions by Swade (1989a). In determining a true brightness temperature for our C_3H_2 lines, we adopt a unity filling factor as was done by Swade (1989a).

When the minimum $\tilde{\chi}^2$ is constrained by the $1_{10} - 1_{01}$ $C^{13}C_2H_2$ optical depth, the solution converges to $n(H_2) = 3.2\times10^4$ cm^{-3} and $X/(dv/dr) = 4.3\times10^{-10}$ pc s km^{-1}. This implies a column density of $1.2(\pm0.9)\times10^{13}$ cm^{-2} assuming a mean line width of 0.29 km s^{-1}. Thus, a fractional abundance of C_3H_2 relative to H_2 is estimated to be 1.2×10^{-9}. The line parameters for this fit are in Table 6.9. As in the case for the other sources, the 21 GHz absorption line is underestimated by the model, along with the 18 GHz line (Figure 6.22). In addition, the 85 and 122 GHz ortho lines are overestimated. Without the constraint from the isotopic data, the solution would converge to a best fit for a low molecular hydrogen density (3.6×10^3), driven again by the best fit for the 21 GHz absorption line.

6.4.2 Summary

Our results show that C_3H_2 has a column density in L134N of 1.2×10^{13} cm^{-2}, consistent with the estimate by Swade (1989a) under optically thin and LTE assumptions using the $1_{10}-1_{01}$ 18 GHz and $2_{12}-1_{01}$ 85 GHz transitions. The LVG model indicates low to moderate

Table 6.9

Summary of Model Results for L134N (Uniform Density)

log n (cm^{-3})	log X/dv/dr (pc s km^{-1})	$\tilde{\chi}^2[\nu]$	N (C_3H_2) (cm^{-2})
4.51(.15)	-9.36(.28)	5.7[5]	$1.2(1.6)\times 10^{13}$

Transition	TEX(K)	τ
$1_{10}-1_{01}$	8.09	0.71
$2_{12}-1_{01}$	4.88	3.94
$2_{21}-1_{10}$	3.98	4.88
$1_{10}-0_{00}$	4.73	1.21
$2_{02}-1_{11}$	3.95	1.54
$2_{11}-2_{02}$	4.54	0.29
$2_{20}2_{11}$	1.41	0.52

Notation is the same as Table 6.7.

Figure 6.22 Comparison between the uniform density results and observations for L134N. Descriptions are the same as Figure 6.12.

Uniform Density Model

n=3.2e4 X/(dv/dr)=4.3e−10 L134N

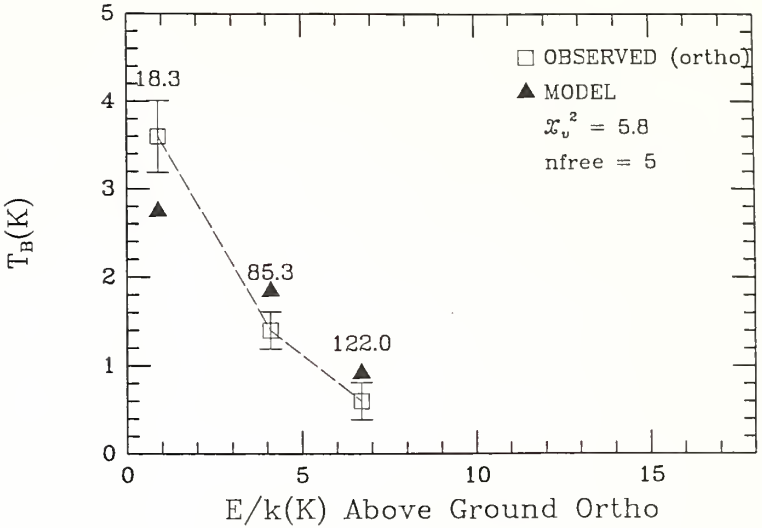

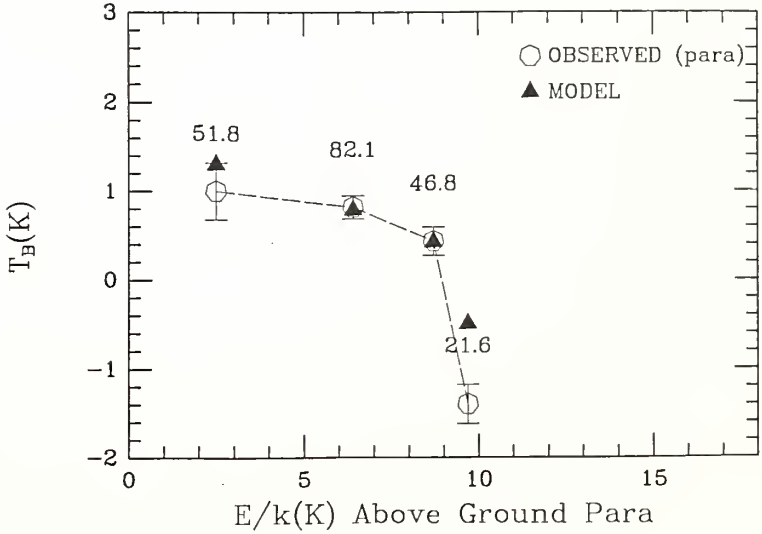

optical depths for these transitions (Table 6.9). C_3H_2 seems to originate in L134N from a dense core of $3x10^4$ cm^{-3} where the NH_3 is thought to originate, as suggested by Swade (1989a). In addition, Snell, Langer and Frerking (1982) determine $n(H_2) = 1x10^4$ cm^{-3} for the regions that CS, a density-sensitive molecule, probes.

6.5 B335

6.5.1 Observations and Model Results

B335 is a low-mass star formation site with high velocity CO emission (Frerking and Langer 1982; Goldsmith *et al.* 1984, Langer, Frerking and Wilson 1986) and a dense molecular core as seen in NH_3 and CS (Menten *et al.* 1984, Myers and Benson 1983 and Snell, Langer and Frerking 1982). Seen in the C_3H_2 $1_{10}-1_{01}$ transition, B335 is a relatively small source, with a half intensity size of about 1.4 arc minutes (Figure 6.23), requiring a filling factor of ~ 0.5 at 18 GHz. The map in Figure 6.24 was made at the 100 m Effelsberg telescope using 30" spacing, 1/2 the FWHP of the telescope beam. The source appears extended in the north-south direction and peaks north of the center reference position, which is at the location of a far infrared object (Keene *et al.* 1983). Individual spectra of the inner 1'x1' region of the map are displayed in Figure 6.25.

Three ortho and 4 para lines were detected toward the center position in B335 (Figure 6.26; Table 6.10). Except for the $2_{12}-1_{01}$

Figure 6.23 Integrated intensity contour map for B335. Observations of the 18 GHz $1_{10}-1_{01}$ C_3H_2 transition were made at the 100 m Effelsberg telescope. Contours are 0.1 to 1.6 K km s^{-1} with steps of 0.1 K km s^{-1}.

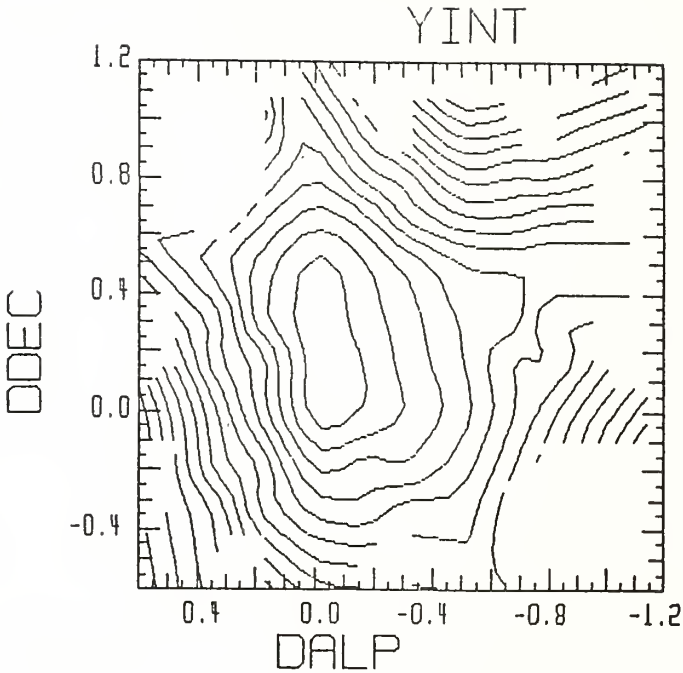
YINT
1.2
0.8
0.4
0.0
-0.4
DDEC
0.4
0.0
-0.4
-0.8
-1.2
DALP

Figure 6.24 C_3H_2 $1_{10}-1_{01}$ spectra toward B335. These spectra contribute to the central 1' x 1' region of the map in Figure 6.23. Position offsets indicated with each profile are (ΔRA, ΔDEC) in arc minutes with respect to the coordinates given in Table 6.10.

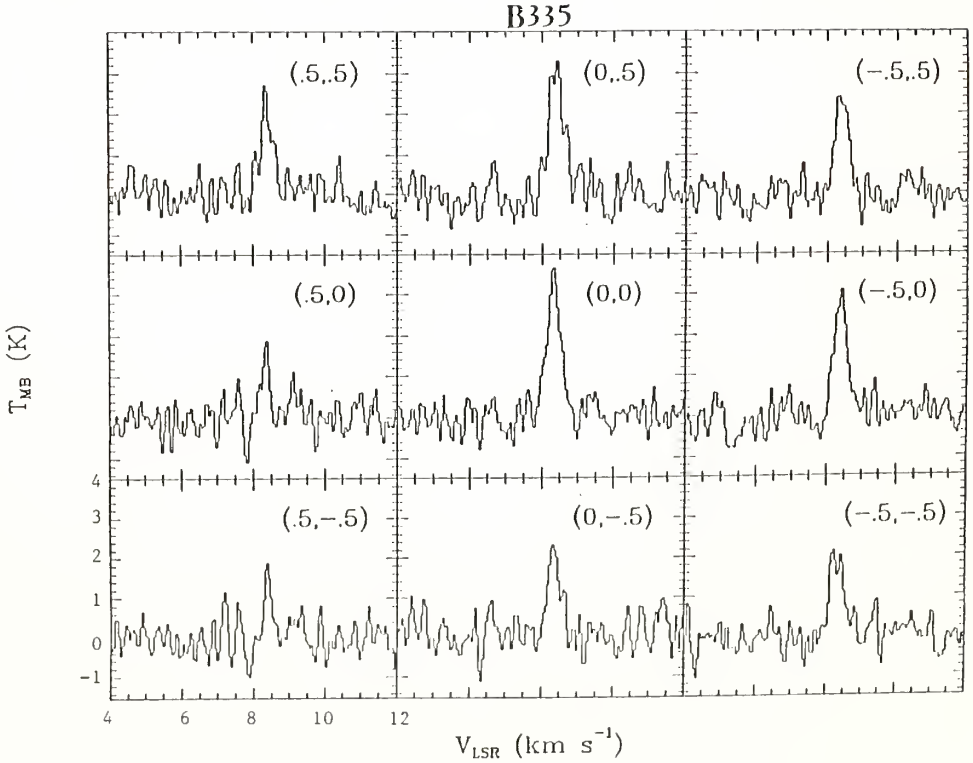
B335
(.5,.5)
(0,.5)
(−.5,.5)
(.5,0)
(0,0)
(−.5,0)
(.5,−.5)
(0,−.5)
(−.5,−.5)
T_{MB} (K)
4
3
2
1
0
−1
4
6
8
10
12
V_{LSR} (km s^{-1})

Figure 6.25 Observed C_3H_2 observations in B335. Descriptions are the same as in Figure 6.14. Source coordinates are given in Table 6.10.

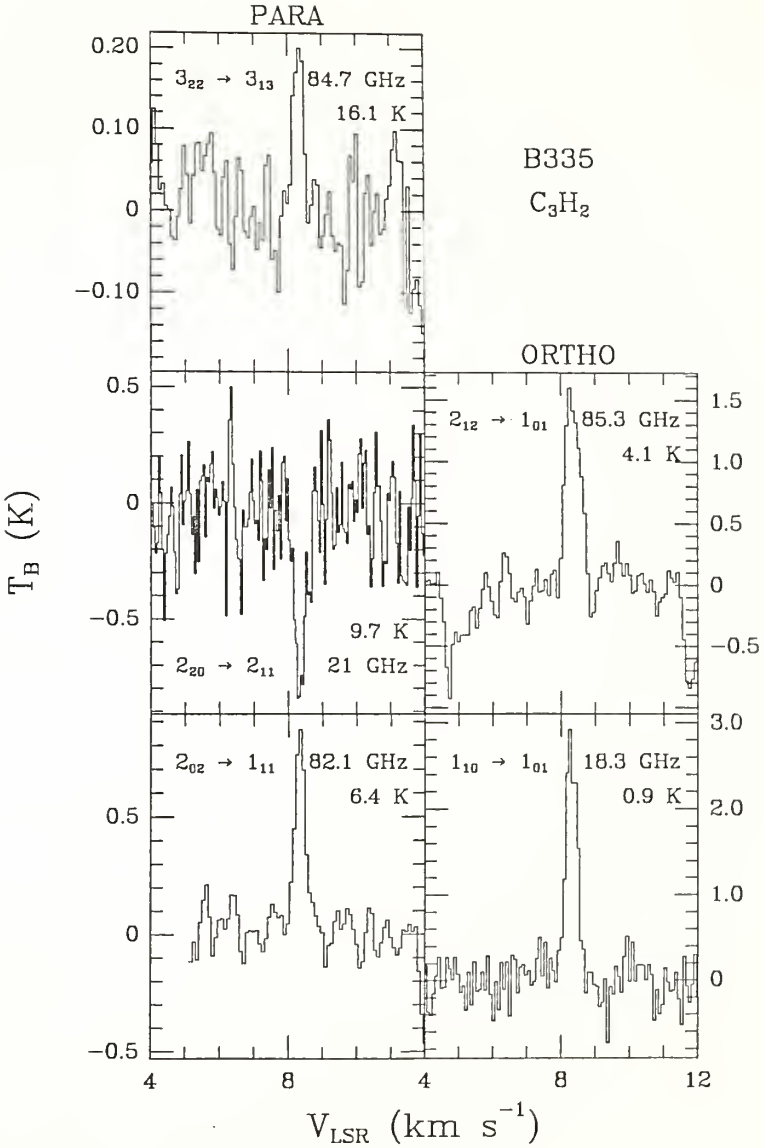
PARA
ORTHO
B335
C_3H_2
$3_{22} \rightarrow 3_{13}$
84.7 GHz
16.1 K
$2_{12} \rightarrow 1_{01}$
85.3 GHz
4.1 K
$2_{20} \rightarrow 2_{11}$
21 GHz
9.7 K
$2_{02} \rightarrow 1_{11}$
82.1 GHz
6.4 K
$1_{10} \rightarrow 1_{01}$
18.3 GHz
0.9 K
T_B (K)
V_{LSR} (km s^{-1})

Table 6.10

Summary of B335 C_3H_2 Observations

Position (RA/DEC)	Transition	Frequency (GHz)	T_B (K)	σ (K)	V_{LSR} (km s^{-1})	ΔV (km s^{-1})	resol (km s^{-1})
$19^h34^m35^s$	$1_{10}-1_{01}$	18.3	3.02	0.40	8.26	0.39	0.09
$07^\circ27'30''$	$2_{12}-1_{01}$	85.3	1.60	0.13	8.25	0.51	0.09
	$2_{02}-1_{11}$	82.1	0.88	0.12	8.36	0.40	0.09
	$2_{20}-2_{11}$	21.6	-0.85	0.40	8.33	0.40	0.08
	$3_{22}-3_{13}$	84.7	0.20	0.06	8.34	0.37	0.09

Notation is the same as for Table 6.2.

85 GHz transition, all of the remaining spectra have similar line widths of 0.40 km s^{-1}. The $2_{12}-1_{01}$ spectra, which has the largest optical depth of any of the observations, has a larger velocity width of 0.5 km s^{-1}. The mean velocity width for the lines is 0.41 km s^{-1} (standard deviation = 0.06 km s^{-1}).

CS (J=1-0), ^{13}CO (J=1-0) and HC_3N (J=5-4) have relatively larger line widths in B335: 0.6 km s^{-1} (Snell, Langer and Frerking 1982; Hasegawa *et al.* 1985), while the J=4-3 HC_3N and NH_3 lines have line widths of 0.4 km s^{-1}. The larger line widths are thought to be due to saturation effects (Hasegawa *et al.* 1985), as opposed to additional velocity components.

As seen in the previous cases, the contours of $\tilde{\chi}^2$ for B335 delineate a minimum valley and require an additional constraint. When we again include the $1_{10} - 1_{01}$ optical depth derived from the isotopic observations, we determine a best fit $\tilde{\chi}^2$ value for the uniform density case to be 6.1. Tau of 0.26 for the 18 GHz transition is shown superposed on the $\tilde{\chi}^2$ contours (Figure 6.26) confining the solution to $n(H_2) = 6.5\times10^4$ cm^{-3}, and $X/(dv/dr) = 1.3\times10^{-10}$ pc s km^{-1}. For a mean velocity width of 0.41 km s^{-1}, a column density of 1.06×10^{13} cm^{-2} is estimated. Thus, the fractional abundance of C_3H_2 relative to H_2 ~ 1×10^{-9}. Without the optical depth constraint, the model converges to lower density and higher abundance values with much larger optical depths. Table 6.11 contains the parameters for the solution, while Figure 6.27 shows the comparison between the predicted results and the observed values.

Figure 6.26. $\tilde{\chi}^2$ contours for the uniform density model in B335 intersected by an optical depth contour. $\tilde{\chi}^2$ contours are 5.5 to 50.0 in steps of 4.5 K. Levels 5.5, 23.3 and 45.6 K are represented by dashed contours with increasing thickness. The optical depth value for the $1_{10}-1_{01}$ (single dotted contour) C_3H_2 transition is obtained from isotopic observations (Bell *et al.* 1988).

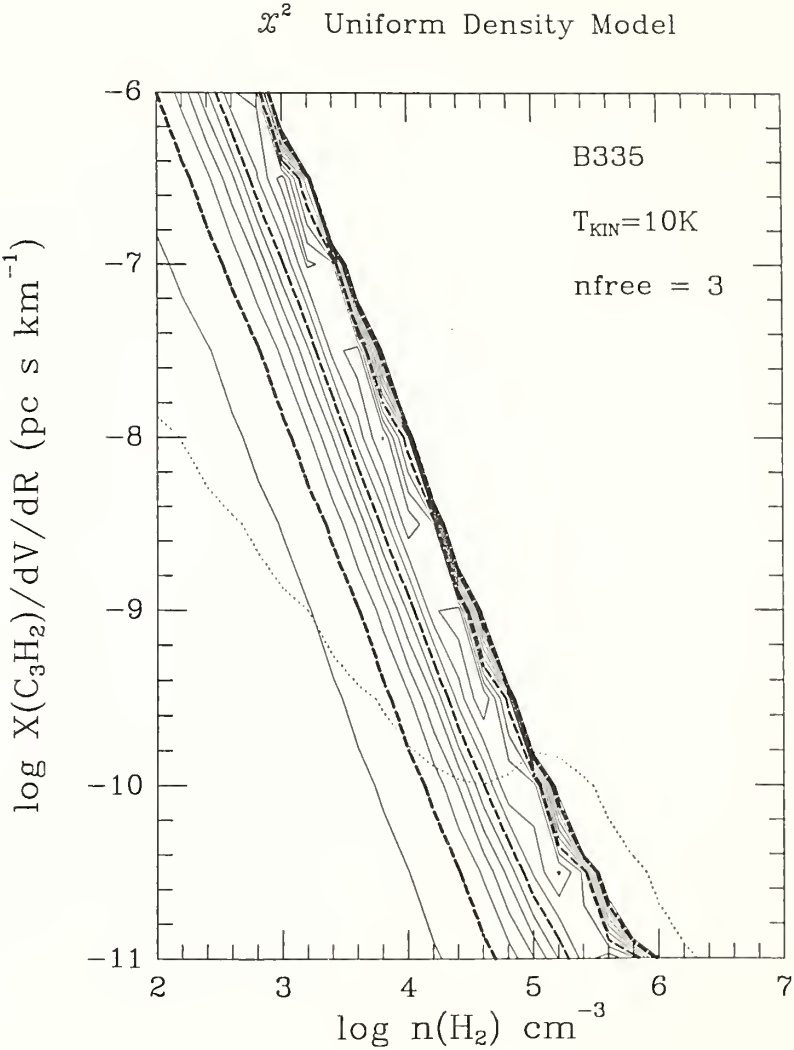
χ^2 Uniform Density Model
B335
T_{KIN}=10K
nfree = 3
log X(C_3H_2)/dV/dR (pc s km^{-1})
log n(H_2) cm^{-3}
-6
-7
-8
-9
-10
-11
2
3
4
5
6
7

Table 6.11

Summary of Model Results for B335 (Uniform Density)

log n (cm^{-3})	log X/dv/dr (pc s km^{-1})	$\tilde{\chi}^2[\nu]$	N (C_3H_2) (cm^{-2})
4.82(.23)	-9.87(.34)	6.1[3]	1.1×10^{13}

Transition	TEX(K)	τ
$1_{10}-1_{01}$	12.22	0.28
$2_{21}-1_{01}$	5.29	2.18
$2_{02}-1_{11}$	4.35	0.86
$2_{20}-2_{11}$	1.37	0.35
$3_{22}-3_{13}$	3.61	0.07

Notation is the same as for Table 6.7.

Figure 6.27 Comparison of the uniform density model results and observations for B335. The model includes the optical depth constraint. Descriptions are the same as Figure 6.12.

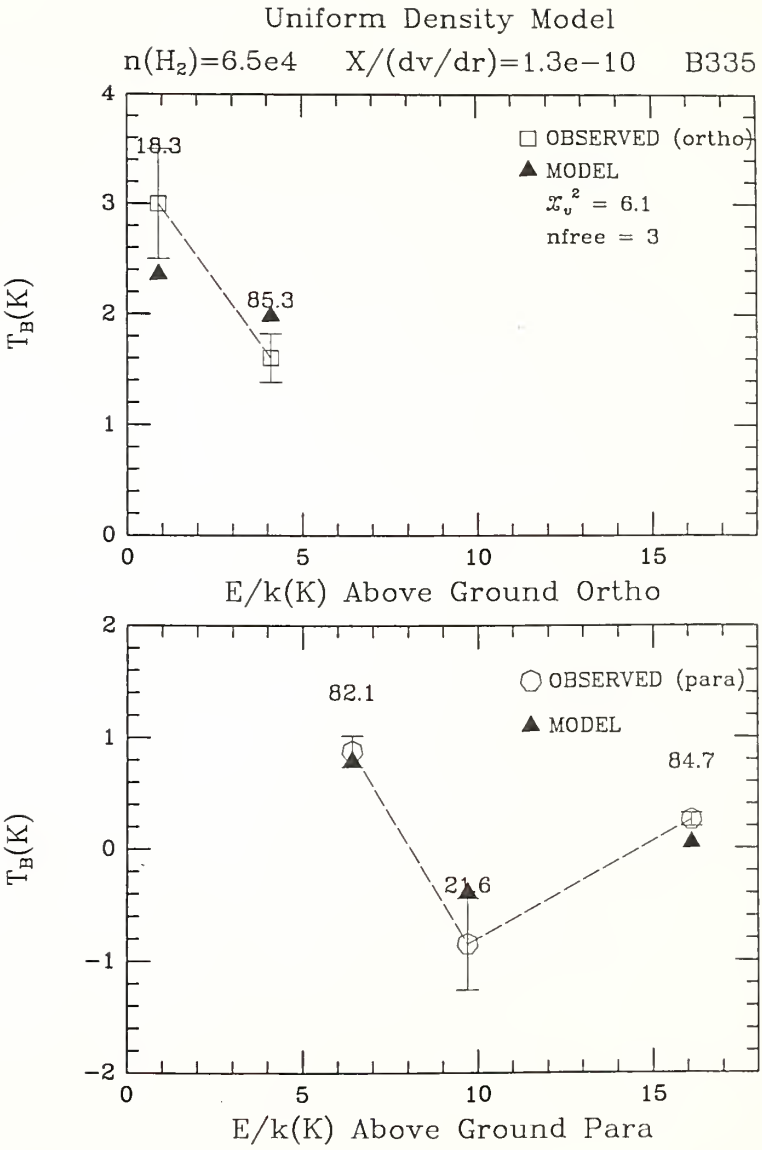
Uniform Density Model
n(H2)=6.5e4 X/(dv/dr)=1.3e−10 B335
OBSERVED (ortho)
MODEL
χu2 = 6.1
nfree = 3
18.3
85.3
TB(K)
E/k(K) Above Ground Ortho
OBSERVED (para)
MODEL
82.1
21.6
84.7
TB(K)
E/k(K) Above Ground Para

The 85.3 GHz transition is overpredicted while the 18 GHz transition is underpredicted, as was the case for the previous sources.

The chi-squared value for the two component model with 3 parameters gives a very much improved value of 0.8 for 2 degrees of freedom. This improvement in fit can be seen in Figure 6.28. All of the lines, including the 21 GHz absorption, which was deviant for the other sources, fit within the 1σ uncertainties. The parameters solved for are : $n_1 = 1.9\times10^4$ cm^{-3}, $n_2 = 6.6\times10^3$ cm^{-3} and X/(dv/dr) = 8.9×10^{-9} pc s km^{-1} (Table 6.12). The denser region is determined to have a higher column density of 2×10^{14} cm^{-3} and the less dense component has a column density of 7.2×10^{13} cm^{-2}, giving a total column density of 2.8×10^{14} cm^{-2}. However, the total optical depth of the $1_{10} - 1_{01}$ predicted by the model for this solution is much larger than observations indicate.

6.5.2 Summary

From CS observations Snell, Langer and Frerking (1982) derived the molecular hydrogen density in B335 to be 10^4 cm^{-3} and Hasegawa *et al.* (1985) determined 5×10^4 cm^{-3} from HC_3N observations. These density estimates are consistent with our C_3H_2 model predictions for the uniform density model constrained by the optical depth information for the $1_{10} - 1_{01}$ $C^{13}C_2H_2$ observations. The resulting columnn density is determined to be 1.1×10^{13} cm^{-2}.

The 2-component model reduces $\tilde{\chi}^2$ significantly to 0.8 and all the observed data are predicted well by the model (Figure 6.28). The

Figure 6.28 Comparison of the 2-component model results and observations for B335. Descriptions are the same as in Figure 6.12.

Two Component Model – 3 Parameters

B335 n(c)=1.9e4 n(h)=6.6e3 X/(dv/dr)=8.9e−9

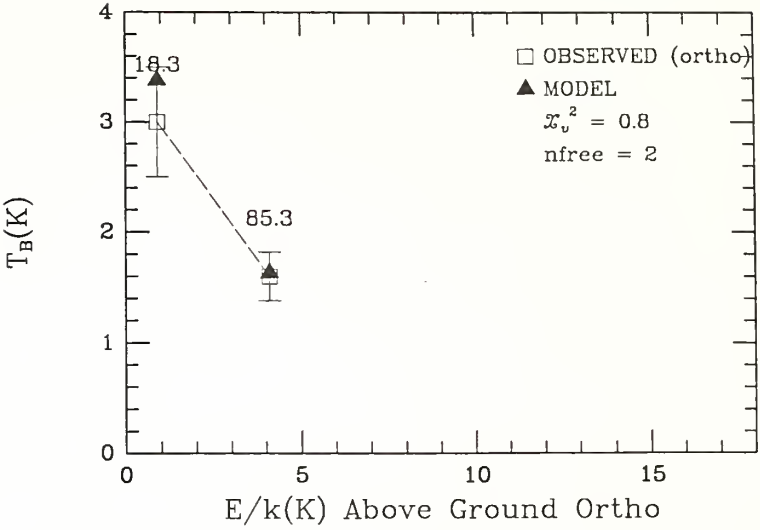

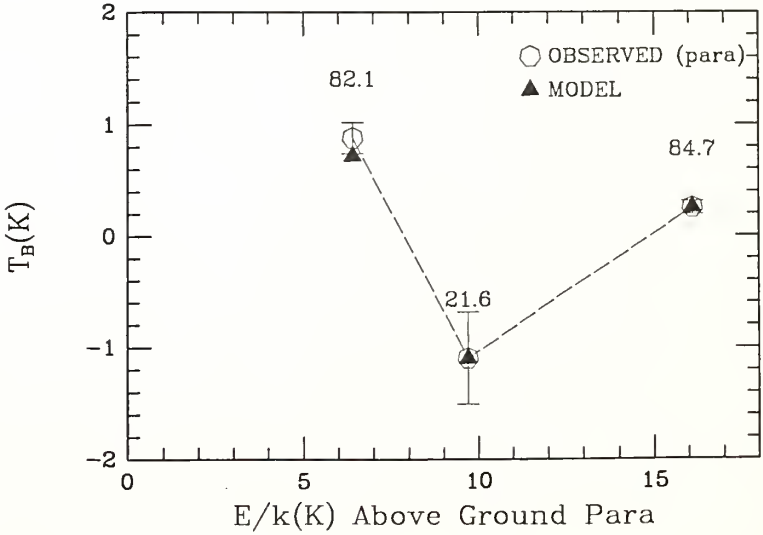

Table 6.12

Summary of Model Results for B335 (2 Component Model)

log n_1 (cm^{-3})	log n_2 (cm^{-3})	log X/dv/dr ($pc\ s\ km^{-1}$)	$\tilde{\chi}^2[\nu]$	N_1 ($10^{14}\ cm^{-2}$)	N_2
4.27(.23)	3.82(.27)	-8.05(.15)	0.8[2]	2.1	0.72

Transition	TEX_1(K)	τ_1	TEX_2(K)	τ_2
$1_{10}-1_{01}$	12.64	3.86	6.07	3.90
$2_{12}-1_{01}$	8.07	22.84	4.61	17.06
$2_{02}-1_{11}$	5.57	11.25	3.61	6.63
$2_{20}-2_{11}$	1.66	5.38	1.69	1.39
$3_{22}-3_{13}$	3.26	1.69	2.87	0.32

Notation is the same as Table 6.5.

derived "core" column density for C_3H_2 is $2(\pm.45)\times10^{14}$ cm^{-2} and the "halo" component has a column density of $7.2(\pm1.7)\times10^{13}$ pc s km^{-1}. km^{-1}. The total optical depth, however, is much larger (~ 8) for the 18 GHz transition than the isotopic observations suggest (~ 0.26).

6.6 Ortho-Para Ratio

For molecules containing symmetrically configured hydrogen atoms, there is a division of rotational energy levels into para (spins anti-parallel) and ortho (spins parallel). This occurs for such molecules as H_2, H_2CO, H_2CS and C_3H_2. Ortho and para species can be considered as virtually 2 distinct molecules which are not coupled by radiative or collisional transitions in interstellar clouds (see section 2.1). Since the formation temperature of a molecule is usually much greater than the difference in energy between the ortho and para states, the corresponding abundance ratio would be given by the ratio of the relative statistical weights.

Kahane *et al.* (1984) measured H_2CO ortho to para ratios in the warm cloud, Orion A, to be 3:1, while in the 2 dark clouds L134N and TMC-1 the ratio is found to be much lower (1:1 to 2:1). Similar results exist from H_2CS observations by Minh, Irvine and Brewer (1989), who determined the O:P ratio to be about 1.8 in TMC-1 and suggested that thermalization of molecules on grain surfaces could be responsible for the low O:P ratio. With the observed ortho and para C_3H_2 lines in TMC-1, L134N, and L1498 we are able to determine the O:P ratio in these dark clouds.

LVG results for ortho abundances and para abundances were generated disregarding any assumption about the *relative* abundance for this calculation. The $\tilde{\chi}^2$ search routine solved for various "best fit" X(ortho)/(dv/dr) and X(para)/(dv/dr) values at identical densities. Ortho to para ratios were then determined from the X/(dv/dr) ratios.

The temperature dependence of the ortho to para ratio for C_3H_2 in thermal equilibrium is shown in Figure 6.29 as the ratio of the respective partition functions, which includes transitions with energies above the ground state up to 100 K. Notice that the ratio approaches the value of 3.0 in the high temperature limit, as expected. With an energy difference between the ortho and para ground states of 2.4 K, the ortho to para ratio can be as low as 2.6 at temperatures of 10 K, which is near the ratios we derive from observations in dark clouds.

Our results show ortho to para ratios ranging from from 2.3 to 3.1 for the 4 dark cloud sources (Table 6.13). It is possible that TMC-1 and L134N have O:P ratios of about 2.5, while L1498 may have a higher ratio of 3.0. The mean value of the ortho to para ratio for all of measured dark cloud sources weighted by the square of the individual standard deviations is 2.41 (±0.11). The apparently higher value of ortho to para ratio in L1498 may not be statistically significant. Perhaps this higher ratio is indicating a kinetic temperature greater that 10 K. Increasing the para abundance relative to the ortho abundance may improve the predictions from the models used for the dark clouds discussed in detail above (which

Figure 6.29 Temperature dependence of the ortho and para ratio of C_3H_2 when populations are distributed according to the Boltzmann law.

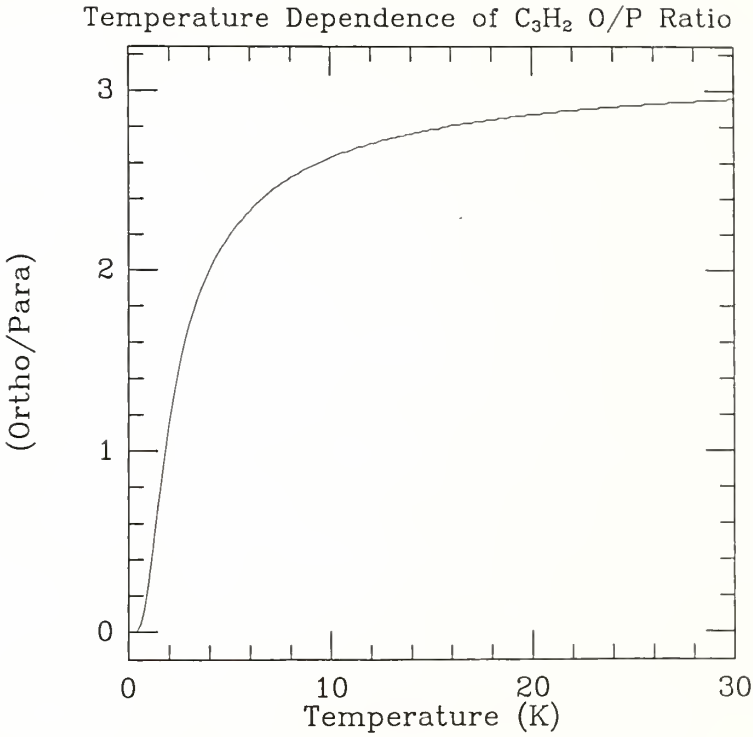
Temperature Dependence of C_3H_2 O/P Ratio
(Ortho/Para)
3
2
1
0
0
10
20
30
Temperature (K)

Table 6.13

Derived Ortho:Para Ratios in Dark Clouds

Source[1]	O:P	σ	# ortho lines	# para lines
TMC-1(0,0)	2.56	0.31	5	5
TMC-1(-4,6)	2.75	0.26	4	3
L134N	2.32	0.05	4	3
L1498	3.10	0.16	4	3

Notes to Table 6.13:

[1] Source positions are listed in Tables 6.2, 6.5, and 6.8.
σ is one standard deviation.

assume an ortho to para abundance ratio of 3.0), particularly for the intensities of the 21 and 46 GHz transities, which are underpredicted in the models for TMC-1 and L134N.

Possible mechanisms affecting ortho-para ratios are discussed in Kahane *et al.* (1984). The role of grains in the case of H_2CO and H_2CS is thought to be responsible for ortho to para ratios less than 3 (Kahane *et al.* 1984; Minh, Irvine and Brewer 1989). As the spin-exchange process by collisions with protons in the gas phase is thought to be inefficient in cold clouds, they propose that thermalization on grain surfaces can lead to ortho to para ratios less than 3. In the case of H_2CO and H_2CS, the energy difference between the ground ortho and para states is larger (~15 K) than the 2.4 K for C_3H_2, and, therefore, thermalization on 10 K grains leads to an ortho to para ratio as low as 1.5 K.

Since the formation temperature for C_3H_2 is expected to be much larger than the energy difference between the ortho and para ground states (2.4 K), the initial abundance ratio is expected to approach the relative statistical weights of the two states. If C_3H_2 is being subsequently thermalized on grain surfaces at 10 K, the ortho to para ratio can be as low as 2.6. The mechanisms of removing the molecule from the grain surface to the gas phase, however, are not properly understood for low temperatures. In addition, how the desorption process itself might affect the ortho to para ratio is not clear.

Measurements of the ortho to para ratios in hotter regions would be interesting to compare with the dark clouds. We might expect to see an ortho to para ratio of 3.0 in such regions, as seen in Figure

6.29 for temperatures > 20 K. Also measurements in additional dark clouds would be interesting to discern if differences in ortho to para ratios exist. Along with this information, it would be valuable to have reliable estimates of temperatures in the dark clouds to decipher the possible temperature dependency of the ratios.

6.7 Model Limitations

The Sobolev approximation was adopted mainly due to its relative computational simplicity resulting from such assumptions as uniform density and large velocity gradients. However, the lack of systematic collapse in these clouds, thus invalidating the large velocity gradient assumption, implies that the results should be treated with caution.

If the uniform density model is left to converge to a solution to match the observed intensities only, it seems to be driven to a solution strongly dependent on the 21 GHz line. Both the uniform density model and the 2-component model do not predict the 21 GHz absorption line well, although they show satisfactory qualitative behavior. Employing a global radiative transfer solution instead of our local solution may improve the misfitted 21 GHz absorption line, since it would be more sensitive to existing excitation gradients.

As the 2-component model allows interaction between the two components, it does improve the absorption line predictions, but not sufficiently. However, the model lacks self-consistency since it employs the Sobolev assumption to decouple effects from one point in

the source from another, while we then allow radiation from the core to be consequently absorbed by the halo component. In most cases discussed above, the 2-component model does not improve the predictions enough to chose it over the more simple uniform density solution.

To obtain accurate abundance values for comparison with chemical models, for example, requires knowing dv/dr. The velocity gradient is only crudely estimated based on the observed line width and source size, and the errors in sources which have no velocity gradients are magnified.

Errors in observed intensities may be incorrectly estimated because of telescope calibration uncertainties. These were estimated to be from 10 to 20% of the observed brightness temperature. Filling factor uncertainties can also affect the brightness temperatures being modeled. Our analysis uses data obtained with beam sizes ranging from 25" to 100". In most cases, we have estimated filling factors based on mapping information of a single transition, neglecting the varying distributions which may exist for the different transitions. If filling factors are obtained from the distribution of the low excitation 18 GHz transition, for example, brightness temperatures for higher frequency, higher energy transition may be underestimated, as we might expect such transitions to have less extensive distributions. Assuming that the clouds are homogeneous and that the different observed transitions are cospatial is not necessarily true. Inspection of the line widths, for example, in TMC-1 (Figure 6.8) indicates that all of these 10 transitions

probably do not arise from the same gas. Note that the $3_{30} - 2_{21}$ transition is only 0.23 km s^{-1} in width, in comparison with the other wider transitions (~ 0.5 km s^{-1}).

The 21 GHz absorption line is particularly sensitive to uncertainties in the cross sections, since the difference in T_{EX} and T_{BG} is a small value dependent on population differences between the 2_{20} and 2_{11} levels.

CHAPTER 7

CONCLUSIONS

From this study we have seen that C_3H_2 is a widespread molecule found in sources possessing a wide range of physical and chemical conditions. This cyclic molecule has been observed in cold, dense clouds, the envelope of a carbon star, giant molecular clouds, diffuse clouds, an external galaxy and a planetary nebula. Ten rotational transitions of wavelengths 1.3 cm to 1.3 mm and ranging in energy above the ground states from 1 to 17 K were observed for this study.

The observations show that the dark cloud sources seem to provide the most hospitable environments for C_3H_2 chemistry to progress. Fractional abundances of C_3H_2 (relative to H_2) in the dark clouds which were studied in detail range from 1 to 2×10^{-9} in B335, L1498 and L134N to 6×10^{-9} in the nearby quiescent cloud, TMC-1. These values are generally less than those derived from isotopic data assuming LTE conditions (Bell *et al.* 1988). The C_3H_2 abundance is comparable, for example, to HC_3N, CH_3C_2H and SO in TMC-1 (Irvine, Goldsmith and Hjalmarson 1987). The massive star-forming region, Orion, is estimated to have a C_3H_2 fractional abundance (relative to H_2) in the ridge component equal to about 8×10^{-10} cm^{-2}, comparable to that of HC_3N and methyl cyanide (CH_3CN) (Irvine, Goldsmith and Hjalmarson 1987). Toward Sagittarius B2, the fractional abundance of

C_3H_2 is estimated to be 2×10^{-9}, similar to that of SO, HC_3N, and CH_3CHO (acetaldehyde).

For the dark clouds TMC-1, L134N, B335 and L1498 we have attempted to create a physical model to match the large variety of transitions we have observed. A spherical uniform density model using the Sobolev approximation to account for optical depth effects was used. The range of excitation energies for the transitions easily detected in dark clouds does not quantitatively constrain the H_2 densities and C_3H_2 column densities well. Yet the model is successful in predicting the general behavior of the observed lines. A prominent deviance of the model from the observations seems to be the inability to predict a deep enough absorption in the $2_{20} - 2_{11}$ 21 GHz transition. This is the only C_3H_2 line observed in absorption against the 2.7 K background radiation and may be particularly sensitive to the accuracy of the calculated cross sections. The intensity of the line depends on determining T_{EX} precisely, since the term $(T_{EX} - T_B)$ being calculated is small. A two component model comprising a dense core and a less dense envelope provides for greater absorption in the 21 GHz line but does not improve the results sufficiently in most cases to warrant this complex configuration. For B335, however, the goodness of fit increased significantly to suggest a dense component with $n(H_2) \sim 2 \times 10^4$ cm^{-3} and a less dense component of 7×10^3 cm^{-3}. In all of the 2-component model solutions, the total calculated optical depths are much larger than those obtained from isotopic data.

Given the data set of C_3H_2 transitions that have been explored, we have seen that the uniform density model can be successful, providing isotopic data is available to constrain solutions of X/(dv/dr) and $n(H_2)$. Observations of two transitions of ^{13}C-substituted C_3H_2 obtained toward TMC-1 (0,0) succeed in confining the solution very well. At the other positions in TMC-1, we have only one (1_{10}-1_{01}) isotopic observation. It would be useful to obtain 3 mm 2_{12}-1_{01} $C^{13}C_2H_2$ observations for these positions in TMC-1 along with the other sources where multiple C_3H_2 transition have been observed, such as B335, L1498 and L134N.

The relatively high abundances of C_3H_2 provide a challenge for chemical models. The advent of C_3H_2 to the list of observed molecules places additional constraints on the ion-molecule chemical processes leading to the formation of complex molecules. Gas phase models are successful in matching observed abundances of simple molecules but have difficulty in predicting sufficient abundances of complex molecules such as C_3H_2 and the cyanopolyynes under steady state conditions. Including large molecules such as PAHs into chemical models augments the chemistry in a way that can provide substantial ammounts of C_3H_2 by the time steady state is reached. Otherwise, abundances of C_3H_2 calculated at steady state times are several orders of magnitude lower than observations, unless the available [C]/[O] ratio is greater than unity, which is larger than the cosmic value. However, at earlier times (~ 3×10^5 yr), before steady state is reached, models can reproduce the larger abundances of C_3H_2. Models which couple cloud dynamics with

chemistry are being developed, and the inclusion of grain chemistry in the models may significantly alter the present models results.

Observations of the deuterated species of C_3H_2 give the surprising result that the deuteration ratio in dark clouds is 0.05 to 0.15, one of the largest values which has been observed to date for any molecular species. These ratios are orders of magnitude higher than the cosmic value of D/H. Chemical models have difficulty explaining such a high fractionation, particularly when the fractionation in CHD is so much lower.

Cyanopolyynes and C_3H_2 are proposed to be related through similar chemistry and have an important common chemical precursor, $C_3H_3^+$ (Herbst 1985; Vrtilek, Gottlieb and Thaddeus 1987). C_3H_2 is generally found to have larger abundances in sources which are most abundant in the cyanopolyynes. This is the case for the dark clouds, where C_3H_2 is most prevalent. A correlation was observed to exist betweeen HC_5N and C_3H_2 in dark clouds, giving additional observational evidence for the relation between cyanopolyynes and C_3H_2 (Cox, Walmsley and Güsten 1989). The precursor ion, $C_3H_3^+$, is known to exist in both linear and cyclic forms (Adams and Smith 1987).

From observations of 4 dark clouds, ortho to para ratios for C_3H_2 are determined to range from 2.3 to 3.1 with a mean value of 2.4. If C_3H_2 is thermalized on 10 K grain surfaces, the ortho to para ratio can be as low as 2.6 to 1. Observations of several ortho and para lines in other dark clouds would be useful to determine if variations of the ratio exist in dark clouds.

Since all the observable low-lying transitions of C_3H_2 ($\leq$ 17 K) have been utilized in the present model calculations, it is beneficial to decide if other transitions can be useful to constrain the solutions. It is interesting to note that the 3_{21}-3_{12} 44 GHz transition is predicted to be in absorption in TMC-1, with a brightness temperature of -0.2 K (weaker than the 21 GHz transition) using the uniform density model constrained by the isotopic optical depth values. This line shows similar potentially diagnostic behavior as the 21 GHz line in that a transition from emission to absorption occurs when high molecular hydrogen densities are present. The 3_{30}-3_{21} 27 GHz transition may also be weakly absorbed (T_B = -0.25) under high density low abundance conditions. However, under the conditions estimated for TMC-1: $X/(dv/dr) = 1\times10^{-9}$ pc s km^{-1} and $n(H_2) = 3.7\times10^4$ cm^{-3}, the 27 GHz transition is expected to be a weak (~ 0.2 K) emission line.

The 2_{21}-2_{12} (55 GHz) and 3_{03}-2_{12} (117 GHz) transitions are the only other transitions predicted to be > 1.0 K in TMC-1. However, at these frequencies, the line intensities will be severely affected by atmospheric O_2 absorption. The brightness temperatures of the para lines near 150 GHz are predicted to be between 0.1 to 0.2 K. Other lines, higher in excitation energy, should in principle, help to constrain the solutions. However, any higher energy lines will have exceptionally low brightness temperatures.

The speculation that large complex molecules such as PAHs exist in the interstellar medium increases the liklihood that other simple ring molecules exists. Mechanisms for forming ring configurations

in the interstellar medium, however, are uncertain. Other molecular ring configurations related to C_3H_2 are proposed by Cooper and Murphy (1988). Hopefully laboratory studies will proceed for these species to eventually provide information for astronomical observations.

BIBLIOGRAPHY

Adams, N. G., and Smith, D. 1987, *Ap. J. (Letters)*, 317, L25.

Allamandola, L. J., Tielens, A. G. G. M., and Barker, J. R. 1987, in *Physical Processes in Interstellar Clouds*, ed. G. E. Morfill and M. Scholer (Dordrecht: Reidel) p. 305.

Askne, J., Höglund, B., Hjalmarson, Å., and Irvine, W.M. 1984, *Ap. J.*, 130, 311.

Avery, L. W. 1987, in *Astrochemistry* (IAU Symp. 120) ed. M. S. Vardya and S. P.Tarafdar, (Dordrecht: Reidel), p. 187.

Avery, L. W. and Green, S. 1989, *Ap. J.* 337, 306.

Avery, L. W., MacLeod, J. M., and Broten, N. W. 1982, *Ap. J.*, 254, 116.

Avery, L. W., Oka, T., Broten, N. W., and MacLeod, J. M. 1979, *Ap. J.* 231, 48.

Bastien, P., Bieging, J., Henkel, C., Martin, R. N., Pauls, T., Walmsley, C. M., Wilson, T. L., and Ziurys, L. M. 1981, *Astr. Ap.*, 98, L4.

Batrla, W., Walmsley, C. M., and Wilson, T. L. 1984, *Astr. Ap.*, 136, 127.

Beckwith, S., and Zuckerman, B. 1982, *Ap. J.*, 155, 536.

Bell, M. B., Avery, L. W., Matthews, H. E., Feldman, P. A. Watson, J. K. G., Madden, S. C., and Irvine, W. M. 1987, *Chem. Phys. Lett.* 136, 588.

Bell, M. B., Avery, L. W., Matthews, H. E., Feldman, P. A. Watson, J. K. G., Madden, S. C., and Irvine, W. M. 1988, *Ap. J.*, 326, 924.

Bell, M. B., Feldman, P. A., and Matthews, H. E. 1981, *Astr. Ap.*, 101, L13.

Bell, M. B. and Seaquist, E. R. 1988, *Ap. J.*, 329, L17.

Bell, M. B, Watson, J.K. G., Feldman, P. A., Matthews, H. E., Madden, S. C., and Irvine, W. M. 1988, *Ap. J.*, 326, 924.

Bergman, P. 1988, Private communication.

Bernheim, R. A., Kempt, R. J., Gramas, J. V., and Skell, P. S. 1965, *J. Chem. Phys.*, 43, 196.

Bevington, P. R. 1969, *Data Reduction and Error Analysis for the Physical Sciences* (New York: McGraw-Hill).

Bieging, J. H., Wilson, T. L., Downes, D., 1982, *Astr. Ap. Suppl.*, 49, 607.

Blake, G. A., Sutton, E. C., Masson, C. R., and Phillips, T. G. 1987, *Ap. J.*, 315, 621.

Bogey, M., Demuynck, C., Destombes, J. L., and Dubus, H. 1987, *Journal of Mol. Spectr.*, 122, 313.

Bogey, M. and Destombes, J. L. 1986, *Astr. Ap.*, 159, L8.

Bohme, P. D. and Millar, T. J. 1989, *M. N. R. A. S.*, 319, 473.

Brown, P. D. and Millar, T. J. 1989, *M. N. R. A. S.*, 237, 661.

Brown, R. D., Godfrey, P. D., and Betens, R. P. A. 1987, *M. N. R. A. S.*, 227, 19.

Brown, R. D., Godfrey, P. D., Cragg, D. M., Rice, E. H. N., Irvine, W. M., Friberg, P., Suzuki, H., Ohishi, M., Kaifu, N., and Morimoto, A. 1985, *Ap. J.*, 297, 302.

Brown, R. L., and Liszt, H. S. 1984, *Ann. Rev. Astr. Ap.*, 22, 223.

Bujarrabal, V., Guélin, M., Morris, M., and Thaddeus, P. 1981, *Astr. Ap.*, 99, 239.

Castor, J. I. 1970, *M. N. R. A. S.*, 149, 111.

Cernichero, J., and Guélin, M. 1987, *Ap. J.*, 297, 302.

Cernichero, J. Kahane, C., Gomez-Gonzalas, J., and Guélin, M. 1986, *Astr. Ap.*, 164, L1.

Colley, D. 1980, *M. N. R. A. S.*, 193, 495.

Combes, F., Boulanger, F., Encrenaz, P. J., Gerin, M., Bogey, M., Demuynck, C., and Destombes, J. L. 1985, *Astr. Ap.*, 147, L25.

Cox, P., Güsten, R., and Henkel, C. 1987, *Astr. Ap.*, 181, L19.

Cox, P., Güsten, R., and Henkel, C. 1988, *Astr. Ap.*, 206, 108.

Cox, P., Walmsley, M., and Güsten, R. 1988, *Astr. Ap.*, 209, 382.

Cummins, S. E., Green, S., Thaddeus, P., and Linke, R. A. 1983, *Ap. J.*, 266, 331.

Dalgarno, A. and Lepp, S. 1984, *Ap. J. (Letters)*, 287, L47.

DeFrees, D.J. and McLean, A.D. 1986, *Ap. J. (Letters)*, 308, L31.

de Jong, T., Chu, S.-I., and Dalgarno, A. 1975, *Ap. J.*, 199, 69.

de Zafra, R. L., Thaddeus, P., Kutner, M., Scoville, N., Solomon, P. M., Weaver, H., and Williams, D. R. W. 1971, *Astrophys. Lett.*, 10, 1.

Dickel, J. R., Dickel, H. R., and Wilson, W. J. 1978, *Ap. J.*, 223, 840.

Dickel, H. R., Dickel, J. R., Wilson, W. J., and Werner, M. 1980, *Ap. J.*, 237, 711.

Downes, D., Wilson, T. L., Bieging, J., and Wink, J. 1980, *Astr. Ap. Suppl.*, 40, 379.

Dreher, J. W., and Welch, W. J. 1981, *Ap. J.* 245, 857.

Felli, M. and Churchwell, E., and Massi, M. 1984, *Astr. Ap.*, 136, 53.

Fertel, J. H., and Turner, B. E. 1975, *Astrophys. Lett.*, 16, 61.

Fischer, J., Sanders, D. B., Simon, M,. and Solomon, P. M. 1985, *Ap. J.*, 293, 508.

Frerking, M. A. and Langer, W. D., 1982, *Ap. J.* 256, 523.

Friberg, P. 1983, *Astr. Ap.*, 132, 265.

Friberg, P., Madden, S. C., Hjalmarson, Å., and Irvine, W. M. 1988, *Astr. Ap.*, 1988, 195.

Gail, H. P., and Sedlmayer, E. 1987, in *Physical Processes in Interstellar Clouds,* ed. G. E. Morfill and M. Scholer, (Dordrecht: Reidel), p. 275.

Gaume, R.A. 1985, Ph. D. dissertation, University of Iowa.

Gellene, G. I. and Porter, R. F. 1984, *Journal Phys. Chem.*, 88, 6680.

Genzel, R., Downes, D., Moran, J. M., Johnston, K. J., Spencer, J. H., Matveyenko, L. I., Kogan, L. R., Kostenko, V. I., Rönnang, B. O., Haschick, A. D., Reid, M. J., Walker, R. D., Giuffrida, T. S., Burke, B. F. and Moiseev, I. G. 1979, *Astr. Ap.* 78, 239.

Genzel, R., Becklin, E. E., Wynn-Williams, C. G., Moran, J. M., Reid, M. J., Jaffe, D. T., and Downes, D. 1982, *Ap. J.*, 255, 527.

Gerin, M., Wooten, H. A., Combes, F., Boulanger, F., Peters III, W. L., Kuiper, T. B. H., Encrenaz, P. J., and Bogey, M. 1987, *Astr. Ap.*, 173, L1.

Gerola, H. and Glassgold, A. E. 1987, *Ap. J. Suppl.*, 37, 1.

Giguere, P. T., Clark, F. O., Snyder, L. E., Buhl, D., Johnson, D.R., and Lovas, F. J. 1973, *Ap. J.*, 182, 477.

Glassgold, A. E., Huggins, P. J., and Schucking, E. L. 1982, in *Symp. Orion Nebula*, Ann. NY Acad. Sci. 395.

Goldreich, P. and Kwan, J. 1974, *Ap. J.*, 189, 441.

Goldsmith, P. F. 1987, in *Summer School on Interstellar Processes*, ed. D. J. Hollenbach and H. A. Thronson, Jr. (Dordrecht: Reidel).

Goldsmith, P. F., and Linke, R. A. 1981, *Ap. J.*, 245, 482.

Goldsmith, P. F., Snell, R. L., Hemeon-Heyer, M. and Langer, W. D. 1984, *Ap. J.*, 286, 599.

Graedel, T. E., Langer, W. D. and Frerking, M. A. 1982, *Ap. J. Suppl.*, 48, 321.

Guélin, M., Friberg, P. and Mezaoui, A. 1982, *Astr. Ap.*, 109, 23.

Guélin, M., Langer, W. D., and Wilson, R. W. 1982, *Astr. Ap.*, 107, 107.

Guélin, M. 1985, in *Molecular Astrophysics - State of the Art and Future Directions*, ed. G. H. F. Diercksen *et al.* (Dordrecht: Reidel), pp. 23-44.

Guélin, M. 1987, in *Astrochemistry* (IAU) Symp. 120, ed. M. S. Vardya and S. P. Tarafdar (Dordrecht: Reidel), p. 171.

Güsten, R., and Downes, D. 1980, *Astr. Ap.*, 87, 6.

Güsten, R., and Fiebig, D. 1988, *Astr. Ap.*, 204, 253.

Güsten, R., and Henkel, C. 1983, *Astr. Ap.*, 125 136.

Güsten, R., Walmsley, C.M., Ungerechts, H., and Churchwell, E. 1985, *Astr. Ap.*, 142, 381.

Harper, D. A., Low, F., Rieke, G., and Thronson, H. A. 1976, *Ap. J.*, 205, 136.

Hasagawa, T., Hirano, N., Kameya, O., Taniguchi, Y., Tosa, M., Takakubo, K., and Seki, M. *Ap. J.*, 1985.

Hayatsu, R., and Anders, E. 1981, *Top. Current Chem.* 99, 1.

Heiles, C. 1968, *Ap. J.*, 151, 919.

Herbst, E. 1983, *Ap. J.*, 53, 41.

Herbst, E. 1985, in *Proto Stars and Proto Planets II*, ed. D. C. Black and M. S. Matthews (Dordrecht: Reidel), p. 668.

Herbst, E., Adams, N.G., and Smith, D. 1984, *Ap. J.*, 285, 618.

Herbst, E., and Leung, C. M. 1986, M. N. R. A. S., 222, 689.

Hjalmarson, Å., and Friberg, P. 1988, in *Formation and Evolution of Low Mass Stars*, ed. A. K. Dupree, and M. T. V. T. Lago (Dordrecht: Reidel).

Ho, P. T. P., Genzel, R., and Das A. 1983, *Ap. J.* 266, 596.

Irvine, W. M., Elldér, J., Hjalmarson, Å., Kollberg, E., Rydbeck, O. E. H., Sorensen, G. O., Bak, B., and Svanholt, H. 1981, *Astr. Ap.*, 97, 192.

Irvine, W. M., Goldsmith, P. F., and Hjalmarson, Å. 1987, in *Summer School on Interstellar Processes*, ed. D. J. Hollenbach and H. A. Thronson, Jr. (Dordrecht: Reidel).

Irvine, W. M., Good, J. C., and Schloerb, F. P. 1983, *Astr. Ap.*, 127, L10.

Irvine, W. M. and Knacke, R. F. 1988, in *Origin and Evolution of Planetary and Satellite Atmospheres*, ed. S K.Atreya, J. B. Pollack, and M. S. Matthews, (Tucson: University of Arizona Press).

Irvine, W. M., Schloerb, F. P., Hjalmarson, Å., and Herbst, E. 1985, in *Protostars and Planets II*, ed. D. Black and M. Matthews (Tucson: University of Arizona Press), p. 579.

Jaffe, D. T., Güsten, R., and Downes, D. 1981, *Ap. J.*, 250, 621.

Johansson, L.E.B., Andersson, C., Elldér, J., Friberg, P., Hjalmarson, Å., Höglund, B., Irvine, W. M., Olofsson, H., and Rydbeck., G. 1984, *Astr. Ap.*, 130, 227.

Johansson, L.E.B., Andersson, C., Elldér, J., Friberg, P., Hjalmarson, Å., Höglund, B., Irvine, W. M., Olofsson, H., and Rydbeck., G. 1984, *Astr. Ap. Suppl.*, 60, 135..

Jones, W. M., Stowe, M. E., Wells, E. E. Jr., and Lester, E. W. 1968, *J. Am. Chem. Soc.*, 90, 1849.

Kahane, C., Frerking, M. A., Langer, W. D., Encrenaz, P., and Lucas, R. 1984, *Astr. Ap.*, 137, 211.

Kanata, H., Yamamoto, S., and Saito, S. 1987, *Chem. Phys. Letters.* 140, 221.

Keene, J., Blake, G. A., Phillips, T. G., Huggins, P. J. and Beichmann, C. A. 1985, *Ap. J.*, 299, 967.

Keene, J., Davidson, J., Harper, D. A., Hildebrand, R. H., Jaffee, D. T., Lowenstein, R. F., Low, F. J.and Peric, R. 1983, *Ap. J. (Letters)*, 274, L43.

Kenny, J. D. and Taylor, D. 1988, internal FCRAO report #323.

Kleinman, D. E., and Wright, E. L. 1973, *Ap. J. (Letters)*, 185, L131.

Kutner, M. L., Machnik, D. E., Tucker, K. D., and Dickman, R. L. 1980, *Ap. J.*, 242, 541.

Kutner, M. L. and Ulich, B. L. 1981, *Ap. J.*, 250, 341.

Lada, C. A. 1976, *Ap. J. Suppl.*, 32, 602.

Lada, C. A., and Chaisson, E. J. 1975, *Ap. J.*, 195, 367.

Langer, W. D., Frerking, M. A., and Wilson, R. W. 1986, *Ap. J. (Letters)*, 306, 108.

Langer, W. D. and Graedel, T. E. 1988, *Ap. J. Suppl.*, 69, 241.

Lee, T. J., Bunge, A., and Schaefer, H. F. 1985, *J. Am. Chem. Soc.*, 107, 137.

Léger, A. and Puget, J. L. 1984, *Astr. Ap.*, 137, L5.

Lepp, S. and Dalgarno, A. 1988, *Ap. J.*, 324, 553.

Linke, R. A., Stark, A. A., and Frerking, M. A. 1981, *Ap. J.*, 243, 147.

Liszt, H. S., Burton, W. B., and van der Hulst, J. M. 1985, *Astr. Ap.*, 142, 245.

Lucas, R., Omont, A., Guilloteau, S., and Nguyen-Q-Rieu 1986, *Astr. Ap.*, 154, L12.

Lucy, L. B. 1971, *Ap. J.*, 163, 95.

Madden, S. C., Irvine, W. M., Matthews, H. E., and Avery, L. W. 1987, in *Summer School on Interstellar Processes*, ed. D. Hollenback and H. Thronson. NASA Technical Memo 88342, pp 155-156.

Madden, S. C., Irvine, W. M., and Matthews, H. E. 1986, *Ap. J.*, 311, L27.

Madden, S. C., Irvine, W. M., Matthews, H. E., Friberg, P. and Swade, D. A. 1984, *Astr. Ap.*, 97, 1403.

Martin, A. H. M. 1972, *M. N. R. A. S.*, 157, 31.

Massi, M., Churchwell, E., and Felli, M. 1988, *Astr. Ap.* 194.

Matthews, H., and Irvine, W. M. 1985, *Ap. J. (Letters)*, 298, L61.

Matthews, H. E., Madden, S. C., Avery, L. W., and Irvine, W. M. 1986, *Ap. J. (Letters)*, 307, L69.

Matthews, H. E., and Sears, T. J. 1983, *Ap. J. (Letters)*, 267, L53.

Mauersberger, R., Henkel, C., Wilson, T. L., and Walmsley, C. M. 1986, *Astr. Ap.*, 162, 199.

Mauersberger, R., Wilson, T. L., and Henkel, C. 1988, *Astr. Ap.*, 201, 123.

Menten, K. M., Johnston, K. J., Wilson, T. L., Walmsley, C. M., Mauersberger, R., and Henkel, C. 1985, *Ap. J.*, 293, 183.

Menten, K. M., Walmsley, C. M., Krugel, E., and Ungerechts, H. 1984, *Astr. Ap.*, 137, 108.

Millar, T. J., Bennett, A., and Herbst, E. 1989, *Ap. J.*, 340, 906.

Millar, T. J. and Freeman, A. 1984, *M. N. R. A. S.*, 207, 405.

Millar, T. J., Leung, C. M., and Herbst, E. 1987, *Astr. Ap.*, 183, 109.

Millar, T. J. and Nejad, L. A. M. 1985, *M. N. R. A. S.*, 217, 507.

Minh, Y. C., Irvine, W. M., and Brewer, M.K. 1989, *Ap. J*, submitted.

Mufson, S. L. and Liszt, H. S. 1979, *Ap. J.*, 232, 451.

Mundy, L. G., Snell, R. L., Evans II, N. J., Goldsmith, P. F., and Bally, J. 1986, *Ap. J.*, 306, 670.

Mundy. L. G., Evans II, N. J., Snell, R. L., and Goldsmith, P. F. 1987, *Ap. J.*, 318, 392.

Myers, P. C. 1985, in *Light on Dark Matter,* ed. F. P. Israel (Dordrecht: Reidel).

Myers, P. C. and Benson, P. J. 1983, *Ap. J.*, 266, 309.

Nyman, L. Å. 1983, *Astr. Ap.*, 120, 307.

Nyman, L. Å. 1984, *Astr. Ap.*, 141, 323.

Olano, C. A., Walmsley, C. M., and Wilson, T. L. 1988, *Astr. Ap.*, 196, 194.

Olofsson, H. 1984, *Astr. Ap.*, 134, 36.

Olofsson, H., Johansson, L. E. B., Hjalmarson, Å., and Nguyen-Quange-Rieu 1982, *Astr. Ap.*, 107, 128.

Omont, A. 1986, *Astr. Ap.*, 164, 159.

Oort, J. H. 1977, *Ann. Rev. Astr. Ap.*, 15, 295.

Penzias, A. A., and Burrus, C. A. 1973, *Ann. Rev. Astr. Ap.*, 11, 51.

Phillips, T. G., Knapp, G. R., Huggins, P. J., Werner, M. N., Wannier, P. G., Neugebauer, G., and Ennis, D. 1981, *Ap. J.*, 245, 512.

Plambeck, R. L., Wright, M. C. H., Welch, W. J., Bieging, J. H., Baud, B., Ho, P. T. P., and Vogel, S. N. 1982, *Ap. J.*, 259, 617.

Prasad, S. S. and Huntress, W. T., Jr. 1980, *Ap. J.*, 239, 151.

Reisenauer, H. P., Maier, G., Riemann, A., and Hoffman, R. W. 1984, *Angew. Chem.*, Int. Ed. Engl. 23, 641.

Righini, G., Simon, M., and Joyce, R. R. 1976, *Ap. J.*, 207, 119.

Rydbeck, O. E. H., Kollberg, E., Hjalmarson, Å., Sume, A., Elldér, J., and Irvine, W. M. 1976, *Ap. J. Suppl.*, 31, 333.

Schloerb, F. P., and Snell, R. L. 1984, *Ap. J.*, 283, 129.

Schloerb, F. P., Snell, R. L., and Young, J. S. 1983, *Ap. J.*, 267, 163.

Scoville, N. J., Solomon, P. M., and Penzias, A. A. 1975, *Ap. J.*, 201, 352.

Scoville, N. Z. 1972, *Ap. J. (Letters)*, 175, L127.

Seaquist, E. R., and Bell, M. B. 1986, *Ap. J. (Letters)*, 303, L67.

Snell, R. L. 1981, *Ap. J. Suppl.*, 45, 121.

Snell, R. L., Langer, W. D., and Frerking, M. A. 1982, *Astr. Ap.*, 255, 149.

Snell, R. L., Mundy, L. G., Goldsmith, P. F., Evans II, N. J., and Sobolev, V. V. 1960, *Moving Envelopes of Stars* (Cambridge: Harvard University Press).

Sternberg, A., Dalgarno, A. and Lepp, S. 1987, *Ap. J.*, 320, 676.

Swade, D. 1989a, *Ap. J.*

Swade, D. 1989b, *Ap. J. Suppl.*

Swade, D., Schloerb, F. P., Irvine, W. M., and Snell, R. L. 1985, in *Masers, Molecules, and Mass Outflows in Star-Forming Regions*, ed. A. Haschick, NEROC. publication.

Tarafdar, S. P., Prasad, S. S., Huntress, W. T., Villere, K. R., and Black, D. C. 1985, *Ap. J.*, 289, 220.

Thaddeus, P., Cummins, S. E., and Linke, R. A. 1984, *Ap. J. (Letters)*, 283, L45.

Thaddeus, P., Gottlieb, C. A., Hjalmarson, Å., Johansson, L. E. B., Irvine, W. M., Friberg, P., and Linke, R. A. 1985, *Ap. J. (Letters)*, 294, L49.

Thaddeus, P., Guélin, M. and Linke, R. A. 1981, *Ap. J. (Letters)*, 246, L41.

Thaddeus, P., Vrtilek, J. M., and Gottlieb, C. A. 1985, *Ap. J. (Letters)*, 299, L63.

Thronson, H. A., and Lada, C. A. 1983, *Ap. J.*, 269, 175.

Tölle, F., Ungerechts, H., Walmsley, C. M., Winnewisser, G., and Churchwell, E. 1981, *Astr. Ap.*, 95, 143.

Townes, C. H. and Schawlow, A. L. 1975, *Microwave Spectroscopy*, (New York: Dover).

Troland, T. H., Crutcher, R. M., and Heiles, C. 1985, *Ap. J.*, 298, 808.

Tucker, K. D., Kutner, M. L., and Thaddeus, P. 1974, *Ap. J. (Letters)*, 193, L115.

Turner, B. E. 1973, *Ap. J.*, 186, 357.

Turner, B. E. 1989, sumbitted *Ap. J.*

Turner, B. E., Rickard, L. J., and Xu, L.-P. 1989, *Ap. J.*, 344, 292.

Turner, B. E., and Thaddeus, P. 1977, *Ap. J.*, 211, 755.

Ungerechts, H., Walmsley, C. M., and Winnewisser, G. 1980, *Astr. Ap.*, 88, 259.

van Dishoeck, E. F. 1988, in *Millimetre and Submillimetre Astronomy*, ed. R. D. Wolstencroft and W. B. Burton (Dordrecht: Reidel).

Vrtilek, J. M., Gottlieb, C A., and Thaddeus, P. 1987, *Ap. J.*, 314, 716.

Walmsley, C. M., Güsten R., Angerhofer, P., Churchwell, E., and Mundy, L. G. 1986, *Astr. Ap.*, 155, 129.

Wannier, P. G. 1980, *Ann. Rev. Astr. Ap.*, 18, 399.

White, G. J., Phillips, J. P., Richardson, K. J., and Harten, R. H. 1986, *Astr. Ap.*, 159, 309.

Whiteoak, J. B., and Gardner, F. F. 1974, *Astr. Ap.*, 37, 389.

Wilson, R. N., Langer, W. D. and Goldsmith, P. F. 1981, *Ap. J. (Letters)*, 243, L47.

Wilson, T. L. 1974, *Astr. Ap.*, 31, 83.

Wilson, T. L., Schwartz, P. R., Epstein, E. E., Johnson, W. A., Etcheverry, R. D., Mori, T. T., Berry, G. G., and Dyson, H. B. 1974, *Ap. J.*, 191, 357.

Wilson, T. L., Mauersberger, R., Walmsley, C. M., and Batrla, W. 1983, *Astr. Ap.*, 127, L19.

Wilson, T. L., Walmsley, C. M., Snyder, L. E., and Jewell, P. R. 1984, *Astr. Ap.*, 127, L19.

Wootten, A. 1987, in *Astrochemistry* (IAU Symp. 120) ed. M. S. Vardya and S. P. Tarafdar (Dordrecht: Reidel), p. 311.

Wynn-Williams, C. G. 1971, *M. N. R. A. S.*, 171, 397.

Wynn-Williams, C., Becklin, E., and Neugebauer, G. 1972, *M. N. R. A. S.*, 160, 1.

Yamamoto, S., Saito, S., Ohishi, M., Suzuki, H., Ishikawa, S., Kaifu, N., and Murakami, A. 1987, *Ap. J. (Letters)*, 322, L58.

Zeng, Q., Hermsen, W., Wilson, T. L., and Batrla, W. 1984, *Astr. Ap.*, 140, 169.